SUPAKAR, TINKU. Ph.D. Engineering High-Throughput Approaches for CRISPR Gene Therapy and Synthetic Biology. (2024)
Directed by Dr. Eric Josephs. 132 pp.

The field of synthetic biology has witnessed rapid advancements in recent years, driven by the integration of high-throughput engineering approaches. This dissertation delves into the design, development, and implementation of high-throughput tools tailored for synthetic biology for various applications while addressing various challenges and complexities associated with each application.

Firstly, we have focused on applying high throughput engineering approach in gene editing tools such as CRISPR. CRISPR based technologies primarily are used for precision gene editing, mutating a DNA sequence based on the CRISPR effector's guide RNA or gRNA. Beyond gene editing, a burgeoning yet less-explored application of CRISPR effectors is in CRISPR-based antiviral biotechnologies. However, the rapid proliferation and mutation rates of viruses introduce unique complexities such as need of expanding recognition across clinical strain variants, enhancing viral detection sensitivity, and limiting mutagenic escape which are not addressed by current gene editing oriented CRISPR guide RNA (gRNA) design tools. To address this challenge, here, we have developed a computational algorithm for the design of efficient gRNAs, termed polyvalent guide RNAs (pgRNAs), which are optimized for simultaneous activity at multiple viral targets by utilizing the inherent tolerance of certain CRISPR effectors to mismatches between their guide RNA (gRNA) spacer sequences and its target sites.

Next, we present a highly parallelized method, compartmentalized CRISPR reactions (CCR), for screening large numbers of gRNA/target/off-target combinations simultaneously *in vitro* for both CRISPR effector activity and specificity, by confining the complete CRISPR reaction of gRNA transcription and CRISPR target cleavage within individual water-in-oil

microemulsions. This approach overcomes the limitations of traditional CRISPR gRNAs screening, which has low throughput. Additionally, we demonstrate that CCR can be used to screen hundreds of thousands of extended gRNA (x-gRNAs) for highly active and highly specific variants of the standard gRNA sequences that can completely block cleavage at off-target sequences while maintaining high levels of on-target activity.

Lastly, we have focused on scaling microfluidic systems which are used in many advanced applications in medical diagnostics, lab-on-chips, and laboratory automation. Microfluidic valves play a key role within microfluidic systems by regulating fluid flow through distinct microchannels. While microfluidic systems are often limited to planar structures, 3D printing enables new capabilities to generate complex designs for fluidic circuits with higher densities and integrated components. However, the control of fluids within 3D structures presents several difficulties, making it challenging to scale effectively and many fluidic devices are still often restricted to quasi-planar structures. Here, we have performed systematic computational and experimental characterization of a modified re-entrant honeycomb structure to generate a modular metamaterial for an active device that allows us to directly regulate flow through integrated, multiplexed fluidic channels “one-at-a-time,” in a manner that is highly scalable.

In conclusion, these high throughput techniques developed in this research, including multiplexed CRISPR-based antivirals, parallelized and compartmentalized *in vitro* CRISPR screening, and scaling microfluidic systems with novel metamaterial designs will enhance the efficiency and scalability of molecular biology methodologies across biotechnology, medicine, and diagnostics.

ENGINEERING HIGH THROUGHPUT APPROACHES FOR CRISPR GENE THERAPY AND SYNTHETIC BIOLOGY

by

Tinku Supakar

A Dissertation
Submitted to
the Faculty of The Graduate School at
The University of North Carolina at Greensboro
in Partial Fulfillment
of the Requirements for the Degree
Doctor of Philosophy

Greensboro

2024

Approved by

Dr. Eric Josephs
Committee Chair

DEDICATION

I dedicate this research to my beloved grandparents, whom I lost during my second year of Ph.D. Though you're not physically here, I felt your blessings are always with me and helped me to succeed in this Ph.D. journey. I also dedicate this dissertation to my parents, family, especially my supportive husband and son. Their unwavering support has been instrumental in shaping who I am today.

APPROVAL PAGE

This dissertation written by Tinku Supakar has been approved by the following committee of the Faculty of The Graduate School at The University of North Carolina at Greensboro.

Committee Chair

Dr. Eric Josephs

Committee Members

Dr. Dennis LaJeunesse

Dr. Jianjun Wei

Dr. Reza Zadegan

May 14, 2024

Date of Acceptance by Committee

May 14, 2024

Date of Final Oral Examination

ACKNOWLEDGEMENTS

First and foremost, I extend my deepest gratitude to my advisor, Dr. Eric Josephs. Without his invaluable guidance, this dissertation would not have been possible. His unwavering support and keen interest at every stage of this study has been crucial for its successful completion. I am also indebted to my committee members, Dr. Dennis LaJeunesse, Dr. Jianjun Wei, and Dr. Reza Zadegan, for generously offering their time and invaluable suggestions, which have significantly enhanced the quality of this dissertation. Furthermore, I am grateful to the Joint School of Nanoscience and Nanoengineering and the University of North Carolina at Greensboro for providing me the necessary resources and financial assistance that facilitated the completion of this dissertation. Special appreciation goes to Dr. Jeffery Alston for his guidance for the last part of my dissertation and for granting me access to the instruments in his laboratory.

I would also like to express my heartfelt thanks to my supportive husband, Dr. Amlan Ghosh, my wonderful son, Neelarka Ghosh, my parents, and my entire family for their unwavering love and support throughout my Ph.D. journey. Additionally, I extend my sincere appreciation to my lab colleagues and friends at JSNN for their invaluable assistance and encouragement throughout this endeavor.

Chapters 1 and 3 have been included with permission, either reproduced or adapted from my published works in iScience and Advanced Functional Materials. In Chapter I, where I am listed as a co-author, I contributed to the design of the computational algorithm. The primary experimentation to validate the algorithm's output was conducted by the leading authors, Dr. Bagchi, Dr. Kulberg, and Dr. Salehin. In Chapters II and III, I led the respective projects with the assistance of my co-authors.

TABLE OF CONTENTS

LIST OF TABLES viii

LIST OF FIGURES ix

CHAPTER I: DESIGN OF POLYVALENT GUIDE RNAS FOR CRISPR ANTIVIRALS BIOTECHNOLOGIES 1

Abstract 1

Introduction 1

Results 5

Design of "Polyvalent" Guide RNAs (pgRNAs) for CRISPR-Based Antivirals 5

Detailed Description of Polyvalent Guide RNAs (pgRNAs) Design Algorithm 9

Abundance of Homoeologous Targetable Sequences Pairs in RNA Virus Genomes 9

Calculation of Mismatch Penalties and Relative CRISPR Activities Using CFD Matrix 10

Workflow for Polyvalent Guide RNAs (pgRNAs) Design Algorithm 13

Frequency of Polyvalent Guide RNAs (pgRNAs) within RNA Viral Genomes 16

Experimental Validation of Our Engineered gRNAs (pgRNAs) 20

Enhanced Viral Suppression in Nicotiana benthamiana using Engineered pgRNAs 20

Engineered pgRNAs for in vitro Viral Detection in Sequences Diverging Up to 25% 25

Engineered pgRNAs Induce Cas9 dsDNA Cleavage with Up to 40% Divergence in Ex Vivo Target Pairs 30

Discussion 35

Experimental Methods 38

Construction of RfxCas13d for in planta Expression 38

Construction of crRNA Expression Vector 39

Agroinfiltration of *Nicotiana benthamiana* (Tobacco) Leaves 39

Quantitative RT-PCR 40

Cas13 Collateral Activity Assays 40

SHERLOCK-Type Viral Detection Reactions 41

Generation of Cas9 Target Sequences 42

in vitro Transcription of Cas9 gRNAs 42

Duplex gRNA Generation 43

Cas9 Cleavage Reactions 43

Resource Availability 44
Code Availability 44
CHAPTER II: COMPARTMENTALIZED CRISPR REACTIONS (CCR) FOR HIGH-THROUGHPUT SCREENING OF GUIDE RNA POTENCY AND SPECIFICITY 45
Abstract 45
Introduction 45
Results 49
Single-Pot CRISPR Reaction Conducted in a Non-Emulsion Setting 49
Compartmentalized CRISPR reactions (CCR) 51
Water-Oil Emulsion: Droplet Size Evaluation 56
Simultaneous Evaluation of Cleavage Efficiency of gRNAs Targeting the Human EMX1 Gene Using Compartmentalized CRISPR Reactions (CCR) 57
Compartmentalized CRISPR Reactions (CCR) to Determine Multiple gRNAs Off-target Cleavage Efficiency 61
Compartmentalized CRISPR reactions (CCR) for Screening of x-gRNAs 64
In vitro Validation of the Top x-gRNA Candidates for EMX1 Off-targets 68
Discussion 69
Materials and Methods 70
DNA Oligonucleotides 70
Protocol for Single-Pot *in vitro* CRISPR Cleavage Assays 70
Protocol for Single-Pot CRISPR Cleavage Assays in Emulsions 71
In vitro Digestion Reactions 72
Dynamic Light Scattering (DLS) Measurement 73
Analysis of the Next-generation Sequencing (NGS) Data 73
CHAPTER III: PROGRAMMED INTERNAL RECONFIGURATIONS IN A 3D-PRINTED MECHANICAL METAMATERIAL ENABLE FLUIDIC CONTROL FOR A VERTICALLY STACKED VALVE ARRAY 75
Abstract 75
Introduction 76
Results 81
Design and Optimization of 3D-Printed Mechanical Metamaterials with Programmable Internal Deformations 81
“Closeable” and “Always Open” Segments for Mechanical Control of Fluid Flow 85

Algorithmic Design and 3D printing of Vertically Stacked Valve Arrays 89
Conclusion..... 94
Experimental Section 96
Materials.....96
Valve Design, Fabrication, and Post-Processing.....96
Uniaxial Compression Test of Re-Entrant Valves at Different Values of θ and φ 97
Fatigue Measurement 97
Flow Rate Measurement in the Flow Channels.....97
Finite Element Analysis (FEA) 98
Data availability 98
CHAPTER IV: CONCLUSION 99
REFERENCES 102
APPENDIX A: SUPPORTING INFORMATION CHAPTER II 121
APPENDIX B: SUPPORTING INFORMATION CHAPTER III 127

LIST OF TABLES

Table 1. Eighteen Possible Targets/gRNAs Capable of Targeting Sequences Within the Human EMX1 Gene as Predicted by Various CRISPR gRNA Design Algorithms [59-68] 57

Table 2. Eighteen Predicated Off-target sites for Four of the gRNAs from CRISPOR [75] as Well as gRNA-16 61

LIST OF FIGURES

Figure 1. Polyvalent Guide RNAs (pgRNAs) Addressing the Differential Need of CRISPR gRNAs for Gene Editing vs. in CRISPR-Based Antivirals 7

Figure 2. Design of Polyvalent Guide RNAs (pgRNAs) for CRISPR-Based Antiviral Applications 8

Figure 3. Prevalence of Homoeologous Cas13 Target Pairs (greater than 16 out of 23 nt or equal to 70% sequence similarity) in Viral Genomes RNA 10

Figure 4. Position-Dependent Effects of Sequence Variants in the Targeted Region on the Activity of Different CRISPR Effectors 11

Figure 5. Process Flow for Polyvalent Guide RNAs (pgRNAs) Design Algorithm 15

Figure 6. Distribution of Cas 13d pgRNAs in Human-Hosted (+) ssRNA Viruses and RNA Viral Transcripts 17

Figure 7. Homoeologous Target pairs and pgRNAs in the SARS-CoV-2 Genome 18

Figure 8. pgRNAs Targeting the HIV-1 provirus genome: Demonstrating High Predicted Cleavage Activity at Both Target Pairs 19

Figure 9. Engineered pgRNAs to Suppress Viral Spread in Higher Organisms (Nicotiana benthamiana) 21

Figure 10. pgRNAs Can Robustly Suppress Viral Spread in Higher Organisms (Nicotiana benthamiana) 23

Figure 11. Cas13a Demonstrates Non-Specific RNAse Activity: A Characteristic Harnessed in Viral Diagnostic Assays 26

Figure 12. pgRNAs Designed to Stimulate “Collateral Activity” by Cas13a for Viral Detection *in vitro* 27

Figure 13. pgRNAs Engineered to Induce Collateral Activity in ssRNA SARS-CoV-2 Virus 28

Figure 14. Cas13 Viral Diagnostic Assay Sensitivity with Engineered pgRNAs 29

Figure 15. pgRNAs Engineered to Stimulate Cas9 dsDNA Cleavage Activity at Divergent Target Pairs 31

Figure 16. pgRNAs Designed to Target Homoeologous Pairs of DNA Sequences Displaying Up to 50% Sequence Divergence *ex vivo* at Synthetic Targets and Original Target Sequences found in DNA Viruses or Retroviruses 33

Figure 17. Agarose Gel Electrophoresis of Cas9-pgRNA Cleavage Products of Synthetic Targets with Increasing Divergence; Related to Figure 16 34

Figure 18. Agarose Gel Electrophoresis of Cas9-gRNA Cleavage Products under Different *in vitro* Conditions Typically Optimized for Gene Editing 34

Figure 19. Single-Pot CRISPR Conducted in a Non-Emulsion Setting 50

Figure 20. Protocol for Compartmentalized CRISPR Reactions (CCR) 52

Figure 21. Validation of Compartmentalized CRISPR reactions (CCR) Technique..... 54

Figure 22. Validation of Compartmentalized CRISPR Reactions (CCR) Technique: Experimental Results 55

Figure 23. Determining the Droplets Size in Emulsions 56

Figure 24. Simultaneous Evaluation of Cleavage Efficiency of gRNAs Targeting EMX1 Gene Using Compartmentalized CRISPR reactions (CCR)..... 59

Figure 25. *In* vitro Validation of the Top Three Screened gRNAs Using CCR 60

Figure 26. Simultaneous Evaluation of Off-target Cleavage Efficiency of Five Different gRNAs Targeting EMX1 Gene Using Compartmentalized CRISPR Reactions (CCR) 63

Figure 27. Compartmentalized CRISPR Reactions (CCR) Designed for Screening of x-gRNAs 65

Figure 28. CCR Results with the DNA library Designed for Screening of x-gRNAs..... 66

Figure 29. Determination of Top “Good” x-gRNAs from Next-Generation Sequencing (NGS)..... 67

Figure 30. Top “Good” x-gRNAs for EMX1 Off-target 1(OT1) Screened Using CCR 68

Figure 31. *In vitro* Validation of the Top “Good” x-gRNAs for EMX1 Off-target 1 69

Figure 32. A 3D-printed, Vertically Stacked Valve Array for Fluidic Control 77

Figure 33. The “Tilt” Angle in a Re-entrant Mechanical Metamaterial Provides a Handle to Tune Relative Mechanical Stiffness Within a 3D printed Device 80

Figure 34. Tilting Re-entrant Mechanical Metamaterials Focuses Mechanical Stresses Within the Structures 82

Figure 35. Banded (Tilted) and Hollowed Re-entrant Mechanical Metamaterials Allow for Controllable Collapse of the Specific Regions in the 3D Printed Structures 84

Figure 36. Tilted Re-entrant Mechanical Metamaterials Allow for the Generation of "Always Open" and "Closeable" Segments / Valves When Subjected to Applied Pressures in Parallel 87

Figure 37. A "Quasi-Planar" Valve Array Integrates into Microfluidic Multiplexors / De-Multiplexors 88

Figure 38. A Stacked Valve Array with Complex Positioning of "Always Open" and "Closeable" Segments of Flow Channels 89

Figure 39. Design of a 3x6x6 3D-Printed, Vertically Stacked Valve Array with 18 Independently Addressable Flow Channels 91

Figure 40. Design and 3D-printing of a 8x12x9 Vertically Stacked Valve Array with 96 Independently Addressable Flow Channels 93

CHAPTER I: DESIGN OF POLYVALENT GUIDE RNAS FOR CRISPR ANTIVIRALS

BIOTECHNOLOGIES

Abstract

CRISPR effectors possess antiviral capability as it recognizes and degrades viral mRNA and RNA genomes that are complementary to its guide RNA (gRNA).[1-8] In this context, adopting a multiplexed targeting[3] strategy, which involves simultaneously targeting multiple sites, has proven effective in enhancing viral suppression compared to individual targeting. Notably, certain CRISPR systems, such as Cas13a and Cas9, exhibit tolerances to target sites that are not perfectly complementary to their guide RNAs (gRNAs). This mismatch tolerance of CRISPR systems is exploited in this study to engineer gRNAs which possess optimal activity at multiple viral target sites. Termed "polyvalent" gRNAs or "pgRNAs," these engineered gRNAs have demonstrated superior antiviral activity within a higher organism (*Nicotiana benthamiana*). In contrast to conventionally designed gRNAs, pgRNAs exhibit remarkable efficacy, reducing detectable viral RNA by over 30-fold. Even in the absence of perfect complementarity with either target, when multiplexed, pgRNAs demonstrates an exceptional ability to decrease viral RNA by more than 99.5%. It is worth noting that pairs of sequences targetable by pgRNAs are prevalent in the genomes of RNA viruses. Consequently, our engineered gRNAs (pgRNAs) provide a solution by emphasizing the necessity for customized approaches to surmount the challenges associated with targeting viruses in eukaryotes using CRISPR systems.

Introduction

Class II CRISPR effectors, such as Cas9, Cas12, and Cas13, are nucleases that employ the spacer segment in its RNA cofactors, referred to as CRISPR RNAs (crRNAs) or guide RNAs

(gRNAs), to recognize and initiate the degradation of nucleic acids bearing a sequence complementary to that segment.[1-8] These guide RNAs (gRNAs) can be designed to target any complementary nucleic acid sequences which has led to advancement of CRISPR-based technologies for various applications, particularly precision gene editing.[1]

However, beyond gene editing, a burgeoning yet less-explored application of CRISPR effectors involves their potential use in novel antiviral diagnostics, prophylactics, and therapeutics, capitalizing on their ability to identify and degrade viral nucleic acids and genetic material.[9] Given that most of pathogenic viruses are RNA viruses, RNA-guided RNA endonucleases such as type VI CRISPR effectors Cas13a (formerly C2c2), Cas13b, and Cas13d exhibit significant promise for CRISPR antiviral biotechnologies.[10-13] Cas13 variants, through their targeted degradation of viral single-stranded RNA (ssRNA) genomes or mRNA, have recently demonstrated the ability to reduce viral loads in plants and plant cells [2,4,14], mammalian cells,[15,16] human cells,[1,17] and in animal models.[5] Type II CRISPR effector Cas9 and type V CRISPR effector Cas12, recognizing and introducing breaks into double-stranded DNA (dsDNA) targets, have also been applied *in vitro* [7, 18,19] and, more recently, in animal models [20] to degrade dsDNA viruses and excise proviruses from cells with latent retroviral infection.[21] Moreover, both type V and type VI CRISPR effectors exhibit nonspecific ssDNAse and ssRNAse activity after target recognition, respectively, and this nonspecific activity has been harnessed for viral detection in diagnostic devices.[6, 11, 17, 22]

Despite the significant promise these applications hold for the future of CRISPR antivirals, the development of robust CRISPR-based antiviral biotechnologies faces numerous challenges distinct from those encountered in developing effective gene editing tools. Specifically, for Cas13-based mRNA knockdown in eukaryotic cells,[23] the rapid proliferation

and mutation rates of viruses introduce unique complexities. Unlike mRNA knock-down experiments in human cells, RNA viruses are dynamic entities, replicating rapidly within a cell and utilizing multiple copies of the viral genome to generate high levels of viral mRNA (vmRNA), resulting in substantial viral protein production.[24] Consequently, CRISPR-based antiviral biotechnologies must grapple with the challenge of maintaining high levels of targeted nuclease activity while avoiding interference with host nucleic acids, all while addressing the issue of mutational escape. Mutational escape occurs when novel mutations emerge, limiting or nullifying the CRISPR effector's ability to recognize the viral genome. To address these challenges, two primary approaches have been employed: targeting the CRISPR effector to regions of high sequence conservation in the viral genome [1, 5, 8, 13, 17] and introducing multiple gRNAs to simultaneously target different segments of the viral genome (multiplexing), thereby reducing the likelihood of viral escape.[1, 13, 17, 18] However, the design of effective gRNAs for antiviral applications remains an ongoing area of research. Notably, the criteria for designing gRNAs for antiviral applications differ from those of other CRISPR biotechnologies, emphasizing the need for specialized considerations.

To address this challenge, in this study, we introduce a computational algorithm tailored for the design of efficient guide RNAs, termed polyvalent guide RNAs (pgRNAs). These pgRNAs are optimized for simultaneous activity at multiple viral targets, leveraging the well-established natural tolerances of specific CRISPR effectors to mismatches between their guide RNA (gRNA) spacer sequences and target sites.[9, 25, 26, 27] Importantly, pgRNAs are meticulously engineered to target multiple viral sites without increasing the risk of "off-target activity" by maintaining significant divergence with the host genome.

Recognizing the significance of multiplexed targeting [20] in inhibiting viral infection, expanding recognition across clinical strain variants,[8, 13] enhancing viral detection sensitivity,[28] and limiting mutagenic escape [18] from CRISPR antivirals, we hypothesized that a single gRNA spacer sequence could be optimized for CRISPR ribonucleoprotein (RNP) activity at multiple specific targets within a viral genome. This hypothesis aimed at altering the gRNA spacer sequence in such a way that, despite lacking perfect complementarity to any individual target, the CRISPR RNPs would effectively recognize and degrade all members of a specific target set (Figure 1B).

We further postulated that this "polyvalent" activity, or the ability to act on multiple sites with a single gRNA, would not only compensate for potential reductions in activity due to mispairings of nucleotides but could enhance antiviral potential. This enhancement could be achieved by increasing the effective number of recognized targets on a virus, improving the rate of viral recognition by each CRISPR RNP, and potentially limiting viral mutagenic escape. Additionally, this approach could reduce the components required for effective multiplexed targeting. This process of engineering gRNAs with "polyvalent" activity contrasts with conventional gRNA design approaches for precision gene editing, where efforts are focused on limiting CRISPR RNP activity at sequences with imperfect complementarity and preventing mutagenic activity at multiple or unintended "off-target" sites (Figure 1A). Given that gRNAs predicted to elicit significant activity at multiple sites would typically be rejected by gene editing-oriented gRNA design tools,[26] our approach emphasizes the need for new strategies optimized specifically for antiviral applications.

Further, to implement our algorithm, experimentally, we demonstrate the superior antiviral efficacy of using pgRNAs with Cas13d in *Nicotiana benthamiana*, a model tobacco

organism, compared to conventionally designed gRNAs. Our findings include: (i) Single pgRNAs targeting two viral sites effectively suppress viral propagation in whole *N. benthamiana* plants at the organ/tissue scale, despite lacking perfect complementarity to their targets. (ii) Treatments with pgRNAs outperform single perfectly complementary "monovalent" gRNAs, often reducing detectable viral RNA by an additional order of magnitude compared to "monovalent" gRNAs, and single pgRNAs are as effective as or better than treatments using two multiplexed "monovalent" gRNA counterparts. (iii) Multiplexed pgRNAs targeting four viral sequences perform even better, reducing detectable viral RNA in planta by over 99.5%.

Further we found that, *in vitro*, despite imperfect complementarity, pgRNAs can be engineered to trigger Cas13's "collateral activity" for viral detection at viral target pairs diverging by up to 25%. Additionally, pgRNAs can direct DNA-targeting CRISPR-Cas9 to degrade multiple DNA targets *ex vivo* with sequence divergence up to 40% (mismatches at 8 out of 20 bp).

In conclusion, research presented here shows that homoeologous sequences are plentiful in viral genomes and can be targeted simultaneously by engineered CRISPR guide RNAs termed as "polyvalent" gRNAs (pgRNAs). The broad applicability and effectiveness of this approach emphasis the distinctive need of alternate strategy for designing CRISPR gRNAs for antiviral applications, distinct from the requirement for precision gene editing.

Results

Design of “Polyvalent” Guide RNAs (pgRNAs) for CRISPR-Based Antivirals

In our algorithm for engineering "polyvalent" guide RNAs (pgRNAs) for CRISPR-based antiviral applications, the initial step involves identifying pairs of protospacers (nucleotide targets of a CRISPR RNP) within the genome of a target virus. These pairs exhibit at least 70%

sequence homology, and the computationally predicted CRISPR-mediated cleavage activity at both pairs falls within the top quartile, following established methods.[27, 29]

Analyzing 2,372 RNA virus genomes from the NCBI Reference Sequence database [30] unveiled the prevalence of these homoeologous pairs, characterized by over 70% identity (more than 16 out of 23 bp) in RNA viruses across mammals, birds, arthropods, and plants (Figures 2B and Figure 3). These pairs are targetable by Cas13 effector molecule. For instance, RNA viruses with 5,000 bp genomes, on average, have about 30 such pairs, while those with 10,000 bp genomes have around 120, adhering to a power law scaling with genome length (Figure 3). In the context of human-hosted RNA viruses, a total of 19,926 homoeologous target pairs were identified across 89 viruses (Figure 2B).

Next, potential pgRNA candidate sequences are generated for each pair by strategically determining nucleotides at positions of divergent sequences between the two targets pairs. This process aims to maximize predicted activity at both target sites by minimizing the potential reductions in activity of the CRISPR effectors due to position-specific mispairings at those sites (as depicted in Figure 2A). To achieve this, "mismatch penalties" are calculated, representing the reduction of CRISPR RNP activity for candidates at sites with imperfect complementarity to the spacer sequence. Mismatch penalties have been quantitatively established for various CRISPR effectors, exhibiting a strong dependence on both the type of mismatch (incorrectly paired nucleotides) and the position of the mismatch(es) along the target. This dependence varies not only by the type of CRISPR effector but also across homologues of the effector derived from different species (Figure 4).[9, 26, 27, 31]

Subsequently, sequences are screened based on biophysical properties that could negatively impact expression or activity, such as sequences with strong predicted secondary

structures or the presence of mononucleotide stretches. These are excluded from consideration. Additionally, to prevent "off-target" interactions with the host genome or transcriptome, any sequences with more than 65% complementarity with potential "off-targets" in the host genome or transcriptome (containing at least 15 complementary nucleotides in the 23 nucleotide Cas13 spacer) are rejected. This stringent selection process results in a final set of pgRNA candidates demonstrating high predicted activity at multiple viral sites and effectively no predicted "off-target" activity compared to the host (as illustrated in Figure 2A). Previous biochemical studies have indicated that Cas13d necessitates at least 18 nucleotides of complementarity to its target for stable binding and target cleavage to occur.[32] For pgRNA designs for Cas13, a conservative requirement of at least 8 mismatches with any host transcripts is imposed.

Figure 1. Polyvalent Guide RNAs (pgRNAs) Addressing the Differential Need of CRISPR gRNAs for Gene Editing vs. in CRISPR-Based Antivirals

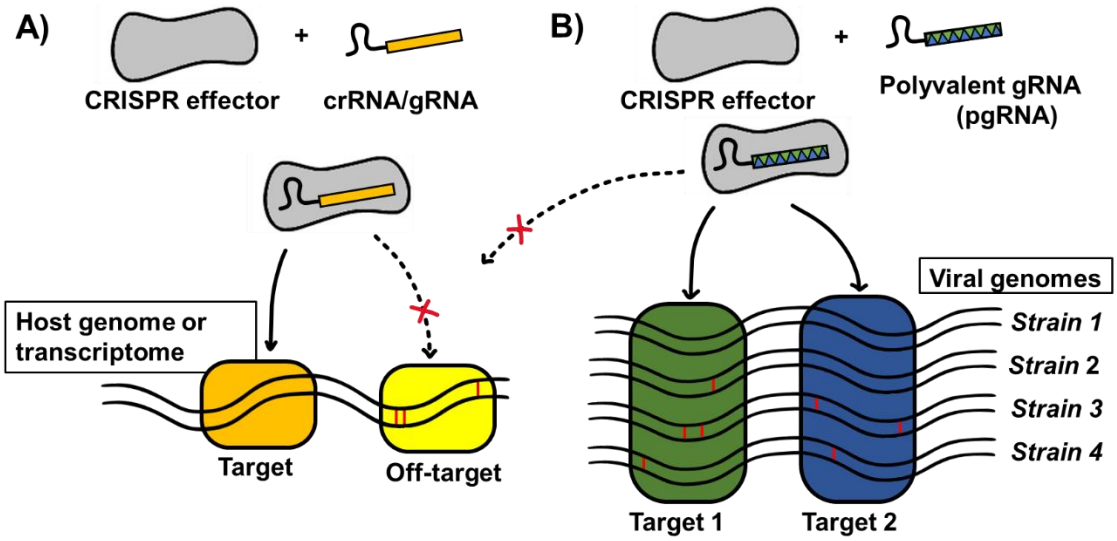

Note. (A) Precision gene editing applications of CRISPR demands extreme specificity, targeting only at a single target; however, (B) Our engineered "polyvalent" guide RNA (pgRNA) lacks perfect complementarity with its target, yet it is strategically optimized to facilitate activity

at multiple viral sites simultaneously, all while avoiding interference with the host genome or transcriptome. This approach aids in suppressing viral propagation, broadening the scope of strain variant detection, enhancing viral detection sensitivity, and preventing mutagenic escape.

Figure 2. Design of Polyvalent Guide RNAs (pgRNAs) for CRISPR-Based Antiviral Applications

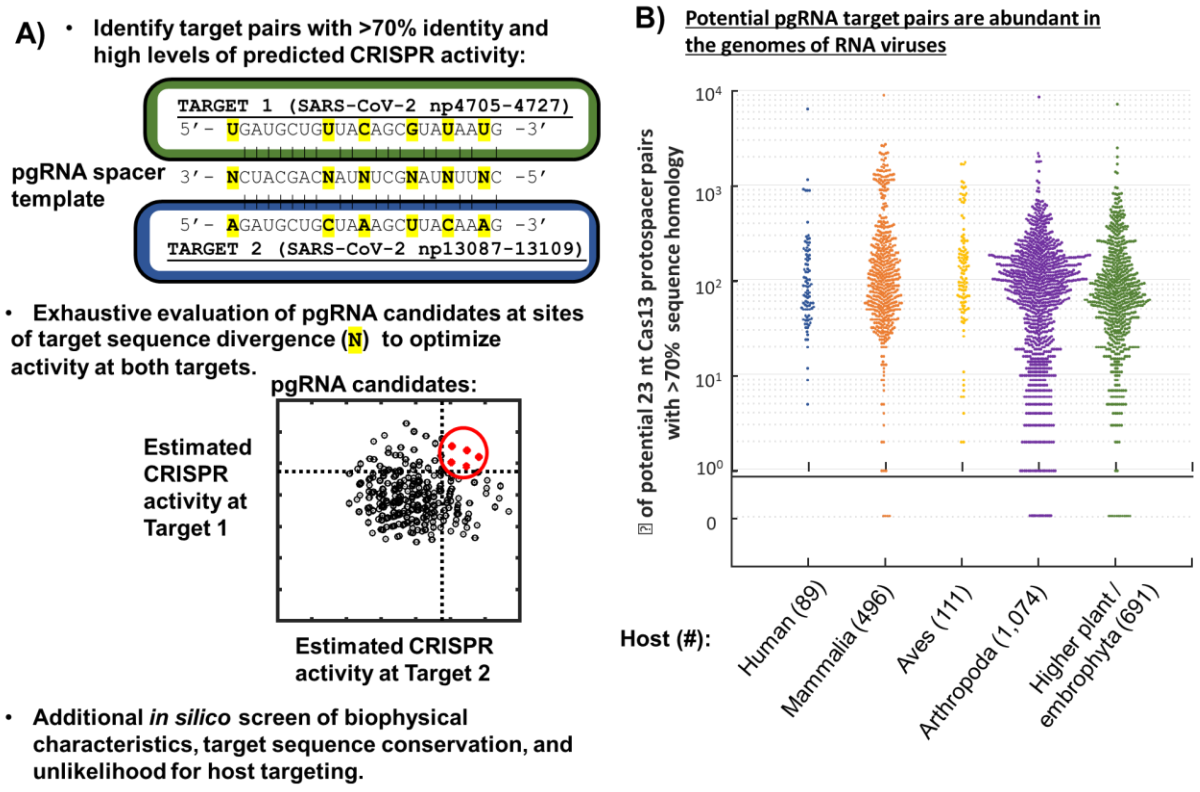

Note. (A) Protocol for pgRNAs design which involve identifying target pairs with over 70% homology in the same viral genome and subsequently minimizes potential decreases in CRISPR activity at homoeologous target pairs by determining the most well-tolerated mismatch- and position-specific mispairings for the particular CRISPR effector. (B) Abundance of homoeologous sites, which share at least 70% similarity out of 23 nt, targetable by pgRNAs for Cas13 across the genomes of RNA viruses.

Detailed Description of Polyvalent Guide RNAs (pgRNAs) Design Algorithm

Abundance of Homoeologous Targetable Sequences Pairs in RNA Virus Genomes

Examining 2,372 RNA virus genomes from the NCBI Reference Sequence database [30] revealed the abundance of homoeologous pairs, marked by over 70% identity (more than 16 out of 23 bp), within RNA viruses across mammals, birds, arthropods, and plants (Figures 2B and 3). To conduct the analysis, we subjected the complete sequences of all RNA viruses associated with human, mammal, arthropoda, aves, and higher plant hosts in the NCBI Reference Sequence database to a "brute force direct alignment" (nucleotide-by-nucleotide, no gaps) for each of 23 nucleotides in each target sequences. This analysis considered only sequence polymorphisms at the same site. The total number of considered viruses for different hosts includes arthropoda (1074 viral species), aves (111), mammal (496), higher plant / embrophyta (691), and human (89)-hosted viruses.

In this analysis, we focused on the (+) strand, as even for (-) and dsRNA viruses, these sequences would match most of mRNA sequences. Viable targets were defined as those lacking polynucleotide repeats (4 consecutive rU's, rC's, rG's, or rA's). Targets derived from different segments or cDNAs of the same viral strain were considered together.

The findings revealed that pairs of targetable sites for Cas13 (23 nt), sharing at least 70% homology, are abundant across the genomes of all RNA viruses. The relationship between the number of target pairs (P) and genome length (L) is well-fitted by the equation: $\log_{10}(P) = 2.202 \times \log_{10}(L) - 6.76$, or equivalently $P = 1.74e^{-7} \times L^{2.202}$, where ($R^2 = 0.7288$) as illustrated in Figure 3.

Figure 3. Prevalence of Homoeologous Cas13 Target Pairs (greater than 16 out of 23 nt or equal to 70% sequence similarity) in Viral Genomes RNA

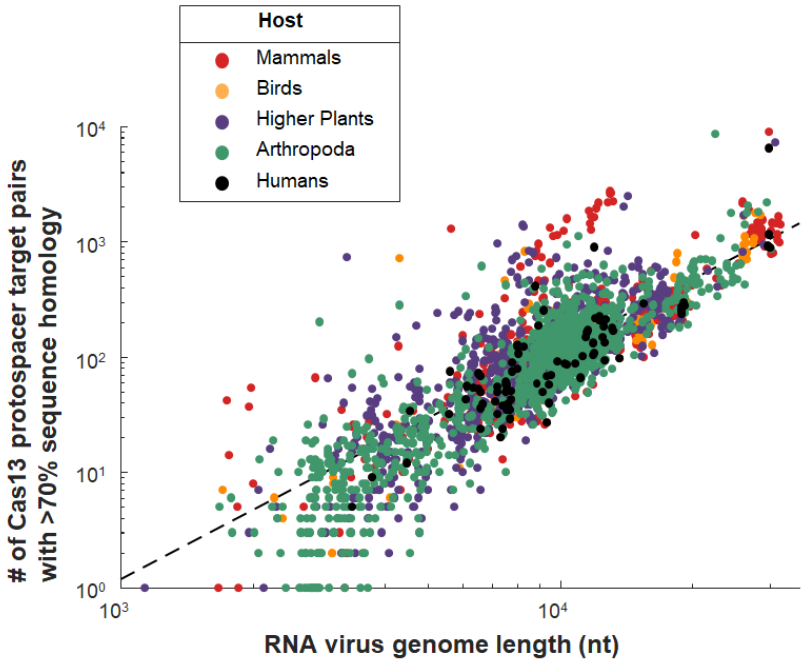

Note. A) Pairs of targetable sites for Cas13 (23 nt), which share at least 70% homology, are abundant across the genomes of RNA viruses. The number of target pairs (P) vs. genome length (L) is fit well (R^2 = 0.7288) by: $\log_{10}(P) = 2.202 * \log_{10}(L) - 6.76$, or equivalently $P = 1.74e\text{-}7 * L^{2.202}$. All complete, RefSeq-quality genomes of RNA viruses, excluding proviruses, available by December 27, 2020, were downloaded from the NCBI Virus database with hosts: arthropoda (1074 viral species), aves (111), mammal (496), higher plant / embrophyta (691), and human (89). Genomes composed of multiple segments or CDS from the same viral isolate were considered together.

Calculation of Mismatch Penalties and Relative CRISPR Activities Using CFD Matrix

The design of polyvalent guide RNAs (pgRNAs) aims to enhance the efficiency of a single guide RNA at multiple viral sites by leveraging the inherent tolerance of CRISPR

effectors, such as Cas9 from S. pyogenes,[9, 29] enAsCas12a, [33, 34] and Cas13d [27, 19] to minimize potential decreases in activity at those sites. These tolerances are highly influenced by the type of mismatch (i.e., which nucleotides are incorrectly paired) and the position of the mismatch(es) along the target. Moreover, these tolerances vary not only among different CRISPR effectors but also across homologs of the effector derived from distinct species, as depicted in the Figure 4.

Figure 4. Position-Dependent Effects of Sequence Variants in the Targeted Region on the Activity of Different CRISPR Effectors

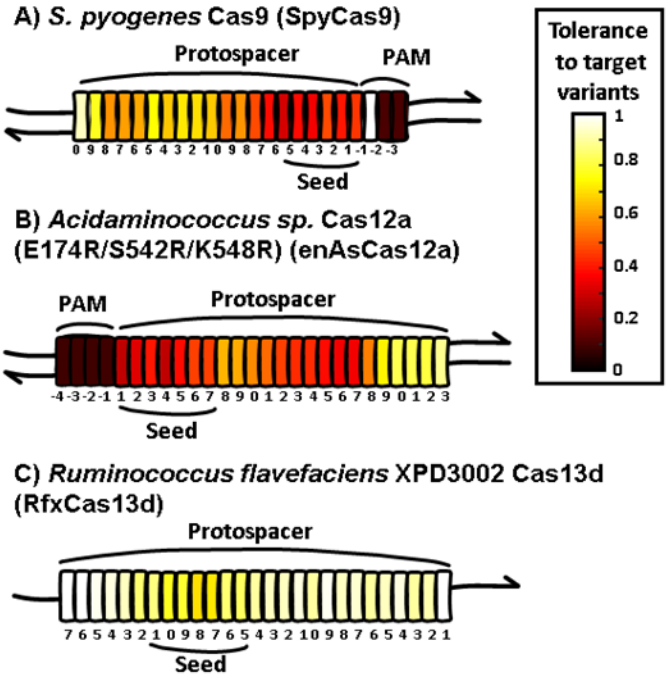

Note. (A) Type II CRISPR effector Cas9 from S. pyogenes,[9, 29] which targets dsDNA; (B) an engineered variant of type V CRISPR effector Cas12a from Acidaminococcus sp. BV3L6, enAsCas12a,[33, 34] which targets dsDNA; and (C) type VI CRISPR effector Cas13d from Ruminococcus flavefaciens XPD3002 [27, 19] which targets ssRNA. Targeted nucleotides are colored by the tolerance, or the average change in activity if there is a sequence variation at that site, of the CRISPR effectors for each position within or near the targeted (protospacer) sites. For

the design of polyvalent gRNAs, we seek to maximize activity of a single gRNA at multiple viral sites by exploiting well-tolerated mismatch- and position- specific mispairings of the CRISPR effectors to minimize potential reductions of activity at these different sites.

To quantify this mismatch tolerance, we evaluated the relative CRISPR activity at targets that deviate from perfect matching with the guide RNA or pgRNA spacer sequences using the Cutting Frequency Determination (CFD) score.[9, 27, 29] The CFD score involves calculating mismatch penalties, which signify the relative reduction in CRISPR activities for each incorrectly paired site, by drawing them from a CFD matrix.[9, 27, 29] This CFD matrix is a table of position-specific reductions in activity due to mispairing between specific nucleotides in the spacer and the target sites. The CFD matrices for CRISPR effectors (RfxCas13d [27] and SpyCas9 [9, 29]) were generated by the Sanjana lab and Doench lab, respectively, using data from "dropout" experiments based on massively parallel screens of gRNA libraries. The CFD score for a given target and gRNA spacer is the product of the penalties for each mismatch, with position-specific penalties averaged over all possible mismatched nucleotides as illustrated in Figure 4. For RfxCas13d,[27] mismatch penalties or CFD score were calculated by comparing the value of the reported log2(Fold-Change in expression) to the second power of gRNA with mismatches to a perfectly complementary targeted mRNA reporter [27]. In instances of missing values, interpolation was employed. For sequential mismatches, including two-in-a-row and three-in-a-row scenarios, position-specific penalties for double- and triple-mismatches were utilized. If off-target sites exhibited less than 15 nucleotide identity compared to the intended target (less than 55% identity), the CRISPR effectors were deemed effectively inactive at those sites. From the mismatch penalty calculation, a tolerance value of ,1, implies that the CRISPR effector exhibits no change in activity regardless of the nucleotide identity at that site, and a tolerance value of ,0,

implies that CRISPR activity is completely abolished if the nucleotide sequence is changed from the expected nucleotide at that site. The "seed" region is defined as a region of high sensitivity (low tolerance) to sequence variations. Cas9 [9, 29] and Cas12a [33, 34] are highly sensitive to sequence variations at its protospacer adjacent motif (PAM) site. In addition, for Cas9 effector, changes in relative activity at sites with non-canonical PAM sequences (besides the canonical PAM sequence d(NGG)) were included in the CFD score as illustrated in Figure 4.

Workflow for Polyvalent Guide RNAs (pgRNAs) Design Algorithm

The protocol for the design of polyvalent guide RNAs (Figure 5) is implemented using MATLAB R2018a (Natick, MA) with the Bioinformatics Toolbox or Jupyter notebook with the biopython package and the NCBI-BLAST+ suite.[7] Each step of the protocol is elaborated below:

Step 1: Estimate activity at different targets ('protospacers'). "On-target" activity for every potential target in a viral genome is found using sgRNA Designer for Cas9 [26, 29] or cas13 design for Cas13d.[27] Only those targets with predicted activity in the top quartile are generally considered as potential pgRNA targets.

Step 2: Identification of Targetable Pairs with high homology. Every potential target is aligned to every other potential target, and pairs with >70% sequence identity (≥ 14 nt identity for 20 nt Cas9 targets and ≥ 16 nt identity for 23 nt Cas13d targets) are identified.

Step 3: Optimization of pgRNA activity at pair sequences. For a given target pair, a pgRNA spacer template was generated complementary to the targets, using the location and sequences of the matching targets. Different 'candidate pgRNA' spacers were generated with all four potential nucleotides (rA, rU, rC, rG) at each of the sites of sequence divergence between the target pairs, *i.e.* 4^n candidates for target pairs with n differences between sequence. A mismatch penalty (CFD score) [9, 27, 29] between the candidates and each of the target pairs was

calculated using the multiplicative approach (*i.e.*, Figure 4). Those with activity at both sites predicted to remain in the top quartile (or other threshold) for both were kept for further evaluation. Candidate pgRNAs with homopolymer repeats (≥4 consecutive 'rU' or ≥5 consecutive 'rG', 'rC', or 'rA') were removed. Additionally, those with GC content less than 30% or greater than 70% were also excluded from further consideration. For RfxCas13d, the respective 'direct repeat' sequence for each crRNA (5'-ACCCCUACCAACUGGUCGGGGUUUGAAAC-3') sequence was appended 5'- to their pgRNA candidate spacers and the pgRNA secondary structures evaluated using the RNAfold function from MATLAB's Bioinformatic Toolbox or Vienna RNA.[35] If the secondary structure of the direct repeat was perturbed by presence of the candidate spacer from its canonical structure, it was removed from consideration, as were those with secondary structure free energy in the spacer region lower than -5 kcal/mol.

Step 4: Estimate activity at potential host off-targets. Candidate pgRNA spacers were aligned to the host genome (*i.e.,* Genome Reference Consortium Human Build 38, GRCh38 human reference genome) and *N. benthamiana* transcriptome (transcriptome assembly v5) using a local nucleotide BLAST optimized for short sequences less than 30 nt (blastn-short). The region surrounding each hit to the human genome or transcriptome, to a total of 23 nt (the 23 nt protospacer for Cas13d and 20 nt protospacer + 3 nt PAM for Cas9), were evaluated for a mismatch penalty score with its respective pgRNA candidates and, in addition to this for Cas9, it looked for the presence of PAM. Those with no predicted interaction with the host genome or transcriptome are considered the leading candidates.

Step 5: Selection of pgRNAs based on additional functional criteria. At this stage, the pgRNA candidates have been screened for high activity at multiple viral targets, no predicted

activity at host “off-target” sites, and biophysical characteristics that suggest they would retain high overall CRISPR activity.[27, 29] The candidates were then further refined by considering pgRNA targets located within specific genes or regions of interest (ROIs) that may be of clinical or functional significance, or conservation of the targets / viral intolerance to mutations by calculating mismatch penalty score (CFD Score) for the pgRNA candidates at each site across different clinical viral strains. This was done prior to the experimental validation. The entire workflow for the design of our engineered gRNAs termed "polyvalent" gRNAs or "pgRNAs," is shown in Figure 5.

Figure 5. Process Flow for Polyvalent Guide RNAs (pgRNAs) Design Algorithm

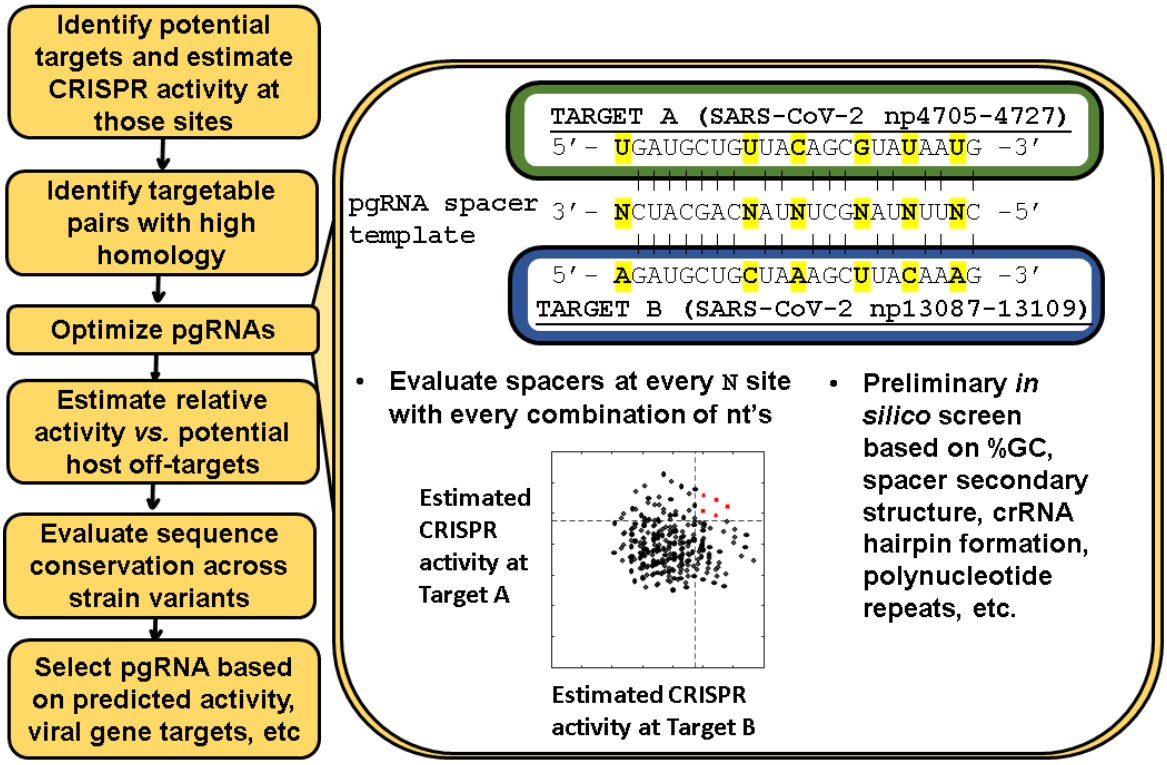

Note. Briefly, in this algorithm, all possible targets in the viral genome were first evaluated for CRISPR predicted activities, using tools such as sgRNA Designer for Cas [9, 29] or cas13design for Cas13d.[27] Subsequently, targetable pairs in the top quartile of predicted on-target

activity with large fractions of identical sequence (*e.g.*, ≥70%) were identified. A pgRNA spacer template was next generated (right). For pairs with 'n' sites, where the sequence differs, 4^n candidate pgRNA spacers were generated with every possible combination of nucleotides at those n sites, which were then evaluated for sufficient predicated relative activities at both target pairs using the Cutting Frequency Determination (CFD) score. Selected candidates were then screened in silico for acceptable biophysical properties known to affect CRISPR activity (secondary structure, GC content, etc.). pgRNA candidates with acceptably high relative activity across all clinical strain variants and acceptably low predicted activity at potential off-target sites with the human genome/transcriptome were then further screened for additional criteria (targeting specific genes or regions of interest (ROIs), for examples) and evaluated using additional gRNA design tools or validated experimentally. Implementation of the algorithm in Python is available at: https://github.com/ejosephslab/pgrna.

Frequency of Polyvalent Guide RNAs (pgRNAs) within RNA Viral Genomes

Our gRNA design algorithm is specifically tailored to address key considerations in CRISPR antiviral applications, such as multiplexing and preventing escape, as well as accommodating clinical variation and viral sequence heterogeneity. To showcase the broad applicability of our algorithm, pgRNA sequences were generated for RfxCas13d targeting all human-hosted (+) ssRNA viruses or viral transcripts (59 in the RefSeq database) (Figure 6). For each target pair with predicted monovalent activity at both sites ranking in the top quartile,[27] we conducted a screening process for biophysical compatibility, ensuring the absence of polynucleotide repeats or significant predicted secondary structure in the spacer. The sequences were aligned to the Genome Reference Consortium Human Build 38 (GRCh38) human reference transcriptome using a local nucleotide BLAST search optimized for short sequences (less than 30

bp). Viable pgRNA candidates were those with no hits (less than 15 bp complementarity out of 23 bp of target sequences) to the human transcriptome and with predicted activity at both sites ranking in the top quartile of all Cas13 activity for targets of that virus.

Figure 6. Distribution of Cas 13d pgRNAs in Human-Hosted (+) ssRNA Viruses and RNA Viral Transcripts

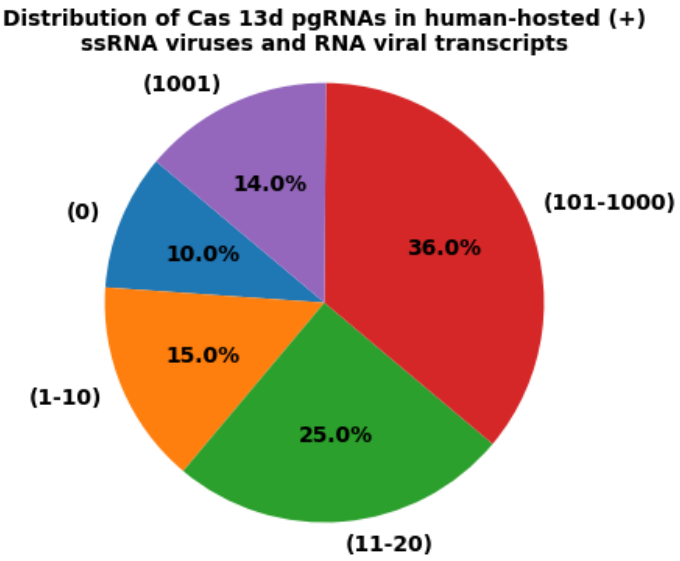

Note. 53 of 59 human-associated (+) ssRNA viruses or RNA viral transcripts have at least one pgRNA sequence (with more than 50% have >100 pgRNA candidates). pgRNA candidates are defined as those gRNA sequences which has predicted activity in the top quartile at multiple viral sites compared to all anti-viral gRNAs; having no BLAST hits to human transcriptome (no complementary targets with greater than 15 out of 23 nt complementarity); and having no biophysical characteristics like strong secondary structure or mononucleotide repeats that would inhibit activity or expression.

The analysis (Figure 6) reveals that 53 out of 59 human-associated (+) ssRNA viruses or RNA viral transcripts have at least one candidate pgRNA sequence, with many (> 50%) having

over 100 potential pgRNA candidates. Additionally, we applied our algorithm to the SARS-CoV-2 genome and HIV-1 provirus sequence. For the SARS-CoV-2 genome, the algorithm identified 144 engineered pgRNA candidates with activity ranked in the top quartile of all anti-SARS-CoV-2 gRNAs at both targetable homoeologous sites. These candidates exhibited no predicted activity with the human transcriptome, and 15 of the target sites showed 100% sequence conservation across approximately 29,000 sequenced clinical variants (Figure 7). Similarly, for the HIV-1 provirus, polyvalent guide RNAs (pgRNAs) were generated, demonstrating high predicted cleavage activity for three homoeologous target pairs, as illustrated in the Figure 8.

Figure 7. Homoeologous Target pairs and pgRNAs in the SARS-CoV-2 Genome

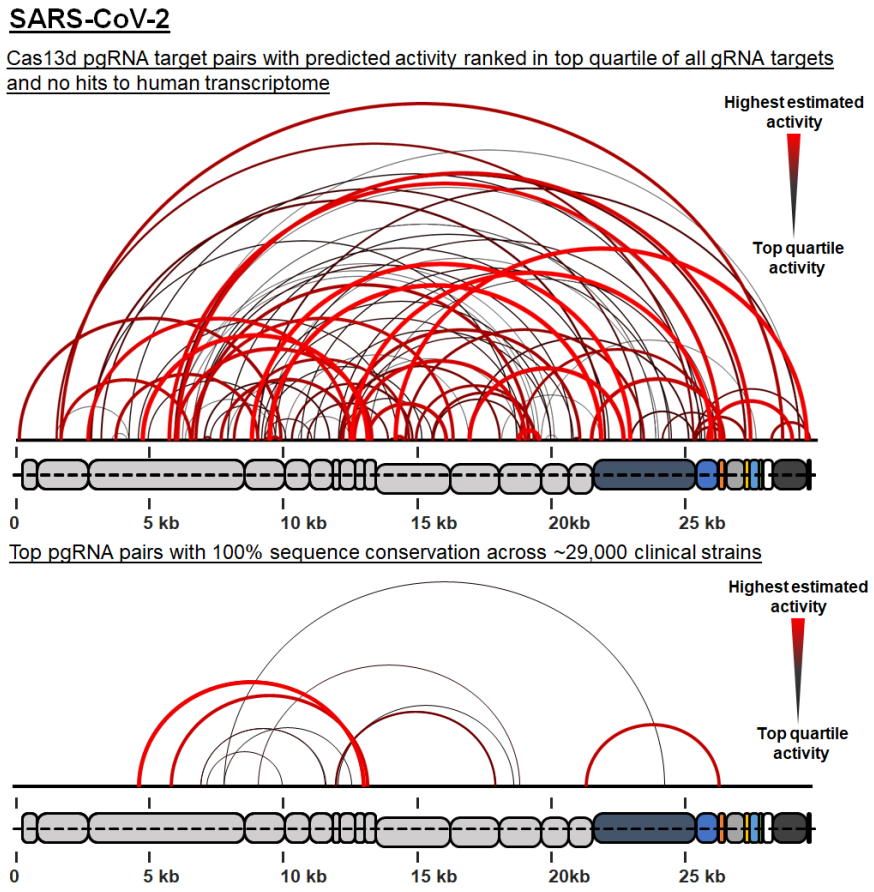

Note. Target pairs in the SARS-CoV-2 genome for pgRNAs, 144 pairs of which predicted to have activity ranked in the top quartile of all anti-SARS-CoV-2 gRNAs at both sites and no predicted reactivity with the human transcriptome (top), 15 of which (bottom) target sites both with 100% sequence conservation across ~29,000 sequenced clinical variants.

Figure 8. pgRNAs Targeting the HIV-1 provirus genome: Demonstrating High Predicted Cleavage Activity at Both Target Pairs

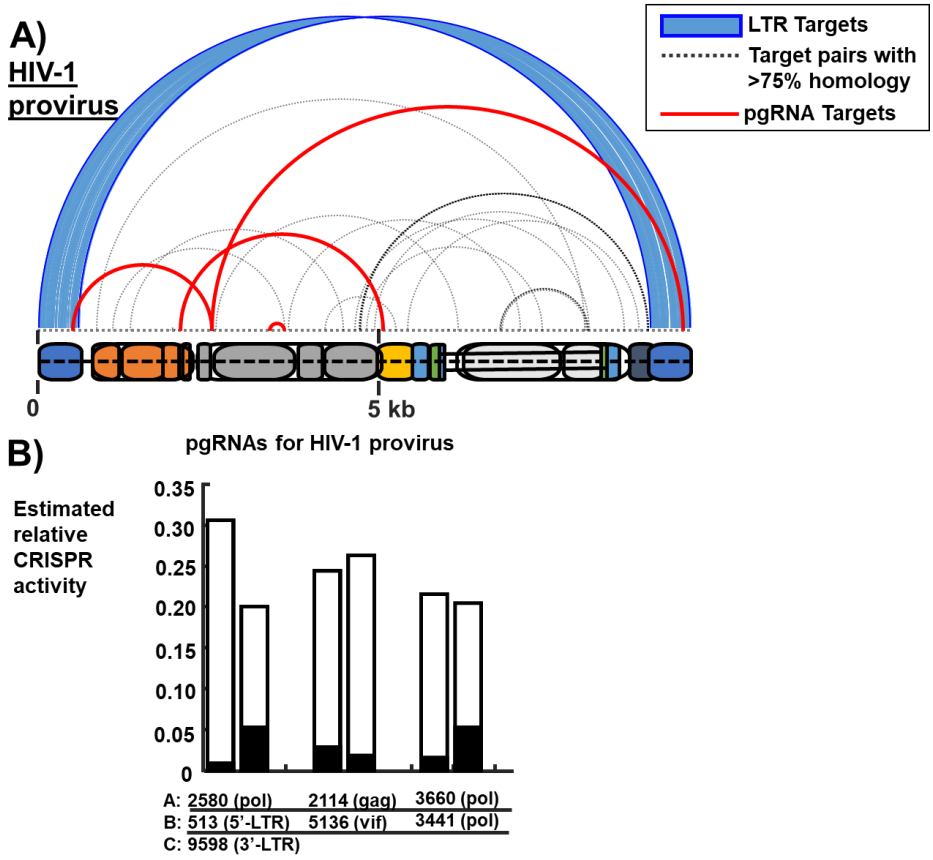

Note. A) Homoeologous Cas13 Target Pairs (>16/23 or 70% sequence identity) for HIV-1 provirus, B) Potential pgRNA candidates for HIV-1 provirus genome exhibiting high predicted cleavage activity at both the target sites.

Experimental Validation of Our Engineered gRNAs (pgRNAs)

Enhanced Viral Suppression in Nicotiana benthamiana using Engineered pgRNAs

Next, we aimed to empirically confirm our design algorithm by assessing whether our engineered pgRNAs, designed for the simultaneous targeting of multiple viral sites, would demonstrate more effective inhibition of *in vivo* viral propagation compared to their perfectly complementary but monovalent counterparts. To conduct this experiment, we designed pgRNAs for RfxCas13d to target pairs of protospacers identified in the tobacco mosaic virus (TMV) (Figure 9).

Following that, *Nicotiana benthamiana* were infected with a TMV replicon (TRBO-GFP) through Agrobacterium tumefaciens-mediated transformation in its leaves.[14, 24] The TRBO-GFP replicon, previously employed as a model for validating CRISPR-based antiviral approaches in plant viral infection,[14] contains an expression cassette for the modified TMV under a strong constitutive 35S promoter. Upon transcription, the replication-competent (+) ssRNA virus can propagate cell-to-cell within the leaf as an uncontrolled infectious agent. In this context, the TMV coat protein gene in the TRBO-GFP replicon was replaced with a green fluorescent protein (GFP) gene, enabling the visual tracking of viral spread (Figures 9A, and 10A) and serving as a reporter for quantifying overall viral RNA levels in the leaves (Figures 10B). We then concurrently deliver transfer DNAs (T-DNAs) to facilitate the temporary expression of RfxCas13d and T-DNAs to express single/multiplexed gRNAs or pgRNAs through agrobacterium tumefaciens-mediated transformation (Figure 9A).

Figure 9. Engineered pgRNAs to Suppress Viral Spread in Higher Organisms (Nicotiana benthamiana)

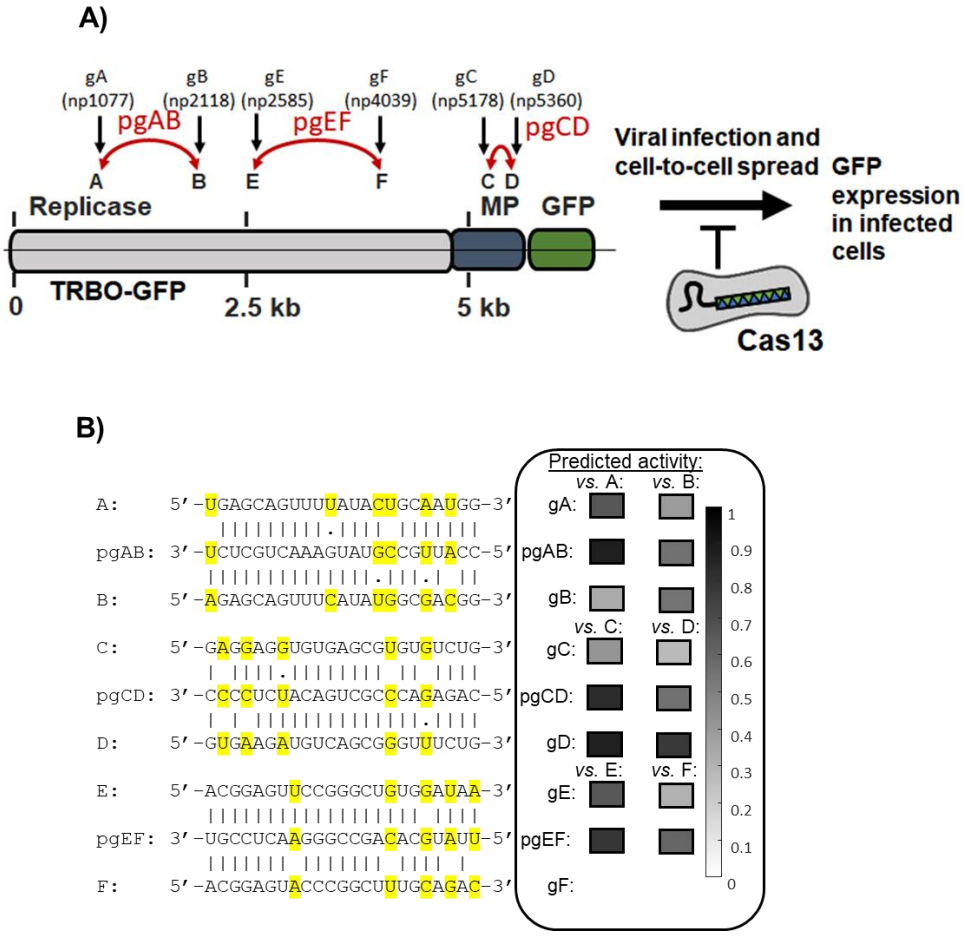

Note. (A) pgRNAs for RfxCas13d were designed to target pairs of sequences in the tobacco mosaic virus (TMV) variant replicon (TRBO-GFP) genome. Monovalent gRNAs (g; black) and polyvalent gRNAs (pg; red). Following infiltration of the replicon (TRBO-GFP) and transcription, the (+) ssRNA virus will infectiously spread cell to cell in the leaf, which can be tracked by expression of a reporter protein (GFP). Viral spread is inhibited by TRBO-GFP-targeting RfxCas13d RNPs, providing a quantitative assay for antiviral activity for different gRNA designs. MP: movement protein. GFP: green fluorescent protein. (B) Pairs of targets in

the TRBO-GFP for the different pgRNAs with up to 30% (6 nt out of 23) divergence between sequences. The sequences of the pgRNAs are optimized for activity at both targets, even with predicted mispairings and non-canonical base-pairings with each target. (right) Predicted activity for gRNAs and pgRNAs at each of the paired target sites.

The designed gRNAs/pgRNAs were specifically directed towards the viral replicase gene or the movement protein (MP) gene, distinct from the GFP (Figure 9A). In addition, the pgRNAs were designed aimed to reduce the probability of interaction with host RNA (*N. benthamiana transcriptome*). To achieved this, it was ensured that each pgRNA incorporates at least 8 or 10 mismatches (less than 57 – 65% complementarity) with all recorded *N. benthamiana* RNA transcripts (utilizing transcriptome assembly v5 [36]). Additionally, an extra search for off-targets were performed using an alternative transcriptome assembly (GIUP: TSA: *Nicotiana benthamiana*, transcriptome shotgun assembly) which identified only potential off-targets with greater than 8 or even 10 mismatches for all the three tested pgRNAs.

Three days post-treatment, plants expressing any of the six distinct monovalent gRNAs exhibited a significant reduction in viral RNA levels in their leaves, typically to around 5% - 25% compared to plants expressing Cas13 along with a non-targeting gRNA (gRNA-NT) or no gRNA (Figure 10A-C). Specifically, plants expressing a single monovalent gRNA displayed less suppression of viral replication compared to those expressing a single pgRNA, which effectively inhibited viral spread (Figure 10A-C) and viral gene expression by over 97% relative to GFP mRNA levels in plants expressing a gRNA-NT (Figures 10B, C). Additionally, one particular gRNA (gRNA TRBO.np5360 or gD in Figure 10C) exhibited notably significant predicted "polyvalent" behavior at its paired site even though it contains mis-paired nucleotides with that site (Figure 9B). Furthermore, it is worth noting that plants subjected to Cas13d treatment

exhibited a healthy phenotype throughout the experiments, despite literature reports suggesting potential long-term toxicity associated with Cas13d expression due to collateral activity,[37] (Figure 10A).

Figure 10. pgRNAs Can Robustly Suppress Viral Spread in Higher Organisms (Nicotiana benthamiana)

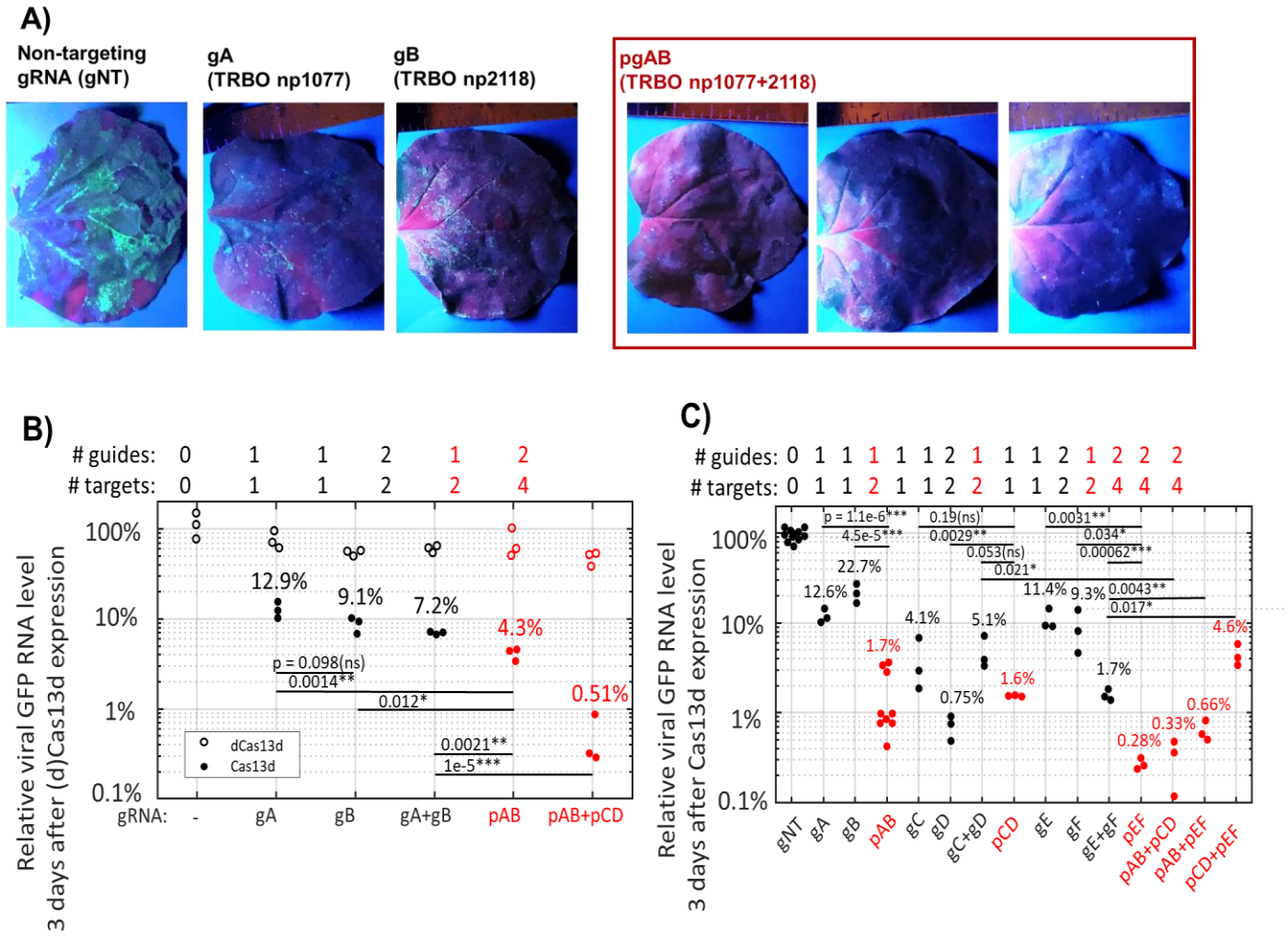

Note. (A) Representative images of leaves illuminated under UV light three days after infiltration show the extent of viral spread by GFP expression. To better visualize differences in viral spread between leaves with different gRNAs, image brightness was increased +20% and image contrast increased by +40%. Leaves of N. benthamiana were infiltrated with a suspension

of *A. tumefaciens* harboring plasmids for the transient expression of RfxCas13d with its gRNAs (pgRNAs, its two "monovalent" counterpart gRNAs, or a non-targeting (NT) gRNA), and an expression cassette for replication-competent TRBO-GFP. As a control, the RfxCas13d mutant is also used in some cases. dCas13d: Catalytically inactive RfxCas13d mutant. Viral spread is suppressed by Cas13 RNPs with gRNAs and strongly by Cas13 RNPs with pgRNAs, but not Cas13 RNPs with a non-targeting (NT) gRNA. In plants treated with pgRNAs, there is some discoloration at the site of agroinfiltration that is distinct from viral GFP. (B-C) Results of quantitative reverse-transcription PCR (qRT-PCR) of leaf RNA after treatment with different gRNAs. Polyvalent guide RNAs (pgRNAs) effectively impede viral transmission in a host organism more efficiently than their perfectly complementary monovalent gRNAs. They perform at least as effectively as multiplexed monovalent gRNAs and even surpass them, exhibiting superior performance as multiplexed pgRNAs, leading to a reduction in viral RNA levels by over 99.5%. Note logarithmic scale on y-axis. Numbers above data points (N = 4 leaves each) are values of mean reduction of viral RNA. Horizontal bars indicate results of two-sided T-test of most relevant comparisons, with p-value above it. * p-value < 0.05; ** p-value < 0.005; *** p-value < 0.0005; ns p-value > 0.05 (not significant).

Subsequently, we examined the impact of multiplexing our engineered pgRNAs in comparison to individual gRNAs and multiplexed monovalent gRNAs. We found that the simultaneous expression of two pgRNAs ((pAB+ pCD), (pAB+ pEF), (pCD+ pEF)), targeting four viral sites with two guides each, resulted in a further tenfold reduction in viral RNA levels (Figure 10C). In two instances, this reduction reached as low as 0.33% to 0.6% of viral RNA in the leaves compared to plants expressing the non-targeting gRNA. Conversely, multiplexed

monovalent gRNAs (gC + gD) achieved a reduction in viral RNA levels to 5% compared to plants expressing the non-targeting gRNAs (Figure 10C).

Further, we checked whether the antiviral efficacy of pgRNAs is attributed to the targeted ssRNAse activity of Cas13d. We found that the plants expressing the pgRNAs exhibited reduced viral levels (often less than 2%) compared to treatments with a catalytically inactive Cas13d variant (dCas13d) which led to a moderate (10% – 40%) reduction in viral RNA levels (Figure 10B). The reduction in viral load due to dCas13d remains unclear, possibly it is associated with a modest silencing effect previously reported in *N. benthamiana* when gRNAs were expressed without any Cas enzymes.[38] These results highlight the essential role of catalytically active Cas13 in achieving the potent antiviral effect of pgRNAs.

Engineered pgRNAs for in vitro Viral Detection in Sequences Diverging Up to 25%

CRISPR-associated Cas13 effectors display non-specific ssRNAse activity, also termed "trans cleavage" or "collateral activity," once they recognize their target RNA, which is complementary to the CRISPR RNA (crRNA).[32, 39] This collateral activity has been utilized in viral diagnostics (Figure 11), as seen in the SHERLOCK system, a tool for detecting human viruses, including SARS-CoV-2.[3, 17, 28] In systems for viral detection using CRISPR effectors like SHERLOCK, the use of multiple guides (gRNAs) has been shown to improve sensitivity in detecting viruses.[28, 39] Additionally, recognizing multiple viral sites not only enhances adaptability to genetic variations but also allows for the detection of multiple viruses within a family. However, the incorporation of numerous gRNAs may lead to increased complexity and costs. Hence, we aimed to investigate whether our engineered pgRNAs could achieve a similar level of collateral activity at multiple viral targets simultaneously, potentially with a reduced number of components.

Figure 11. Cas13a Demonstrates Non-Specific RNAse Activity: A Characteristic Harnessed in Viral Diagnostic Assays

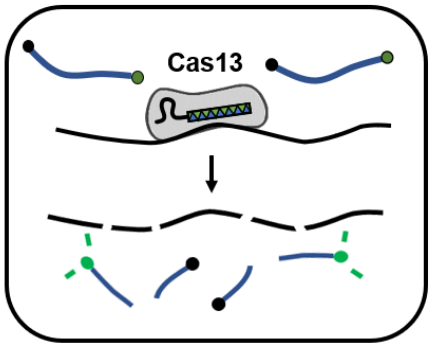

Note. After recognizing a target, Cas13 exhibits nonspecific RNAse activity; nonspecific degradation of a fluorescent reporter RNA results in a fluorescent signal that can be detected in viral diagnostic assays.

LwaCas13a, the Cas13 variant utilized in the SARS-CoV-2 SHERLOCK assay is available commercially as a purified enzyme. However, unlike RfxCas13d,[27] LwaCas13a has not undergone comprehensive characterization regarding its tolerance to mismatches. We proposed that if the stability of base-pairing between the gRNA spacer and target predominantly activates Cas13 RNAse activity, we could leverage the mismatch sensitivities established for RfxCas13d as a starting point for designing pgRNAs tailored for LwaCas13a in viral detection applications. Our hypothesis was validated; even though SHERLOCK and collateral activity activation have been reported to be sensitive to single-nucleotide polymorphisms in their targets, [3, 11] we successfully engineered single pgRNAs for LwaCas13a that could elicit collateral activity at multiple synthetic targets (Figure 12). These pgRNAs demonstrated detectable collateral activity even at targets with up to 4 nt mismatches with the gRNA spacers (Figure 12).

Figure 12. pgRNAs Designed to Stimulate "Collateral Activity" by Cas13a for Viral Detection *in vitro*

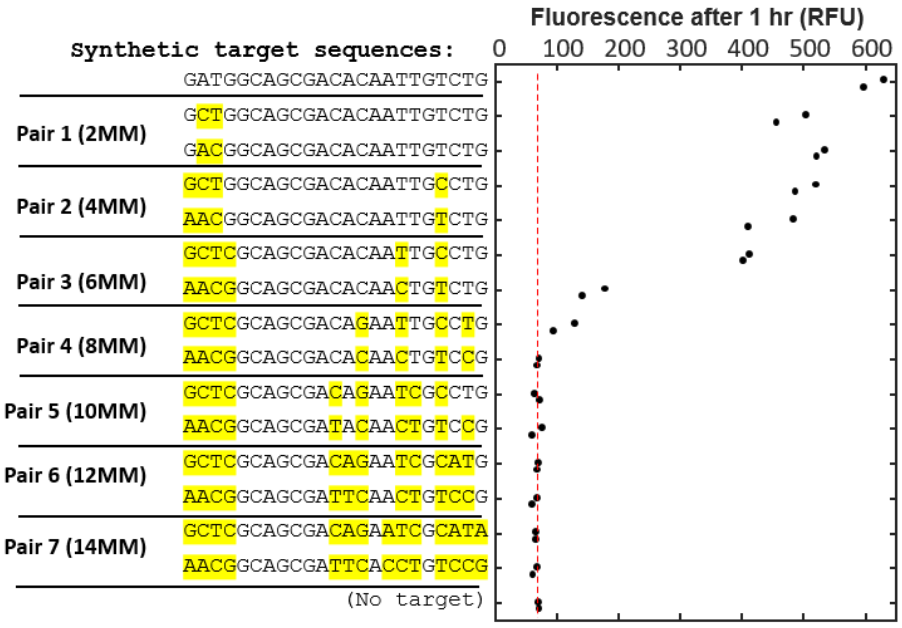

Note. Detectable collateral activity is stimulated by Cas13a in vitro at targets with sequence divergence up to 25%.

Moreover, utilizing the mismatch penalties established for RfxCas13d,[27] we successfully optimized pgRNAs for activity at homoeologous targets specific to the SARS-CoV-2 virus, which exhibited divergence of up to 25% (6 out of 23 nt) (Figure 13). These designed pgRNAs exhibited collateral activity at both targets, despite containing mis-paired bases with each target site. In contrast, perfectly matched "monovalent" gRNAs displayed virtually no cross-reactivity in vitro at paired sites characterized by such high sequence divergence (Figure 13). These findings suggest that as an initial approach, at least *in vitro*, pgRNAs for LwaCas13a can be developed using design principles established for RfxCas13d.

Figure 13. pgRNAs Engineered to Induce Collateral Activity in ssRNA SARS-CoV-2 Virus

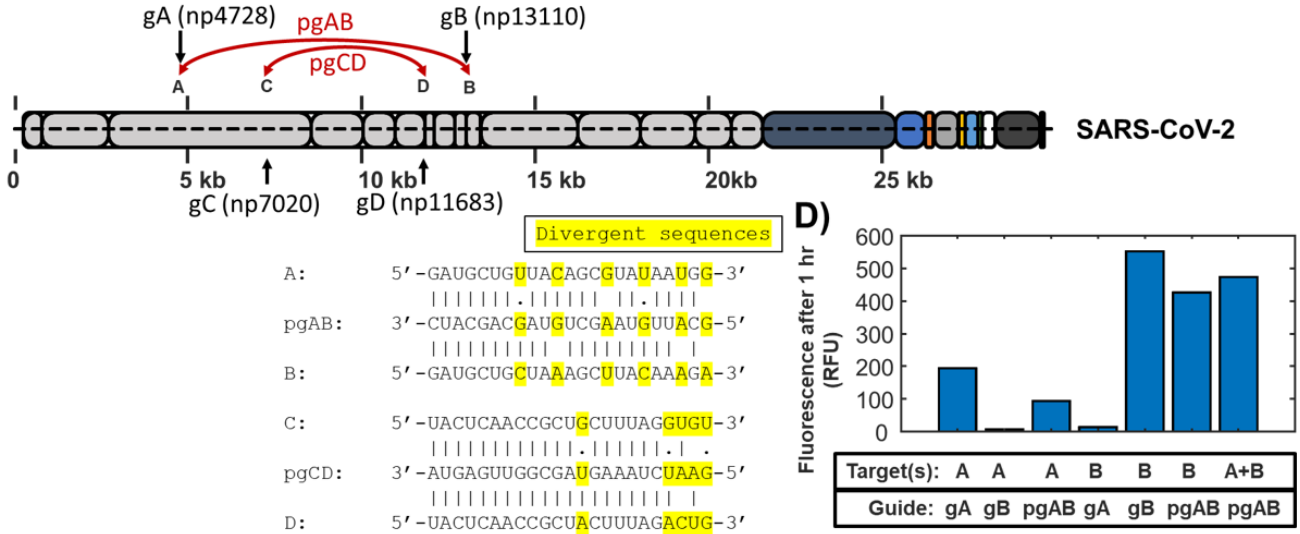

Note. pgRNAs were designed to target (+) ssRNA virus SARS-CoV-2. The sequences of the pgRNAs are optimized for activity at both targets (right), even with predicted non-canonical base-pairings with each target.

Next, we sought to evaluate the applicability of pgRNAs in *in vitro* viral diagnostics. For which, we designed 23 pgRNAs with high predicted activity (based on RfxCas13d design rules) targeting 15 homoeologous pairs in SARS-CoV-2. Subsequently, we assessed their collateral activity and compared the results with the combined activity of their perfectly matched monovalent gRNA counterparts (30 individual gRNAs). Our findings (Figure 14) revealed that each tested pgRNA exhibited collateral activity at levels like or higher than their combined monovalent gRNA counterparts in the presence of both target sites in the sample. Importantly, no off-site collateral activity was detected in the presence of non-targeted RNA sequences, universal human reference RNA (from 10 human cell lines), or human lung total RNA. We further determined their limits of detection (LOD) in a SHERLOCK-type assay using LwaCas13a and

the best-performing pgRNAs. The results indicated that Cas13 with single pgRNAs (targeting two sites) or multiplexed (2) pgRNAs (targeting four sites) could robustly generate detectable signals in samples initially containing 40 copies/μL heat-inactivated SARS-CoV-2, performing comparably to their monovalent counterparts and even some multiplexed monovalent gRNAs (Figure 14).

Figure 14. Cas13 Viral Diagnostic Assay Sensitivity with Engineered pgRNAs

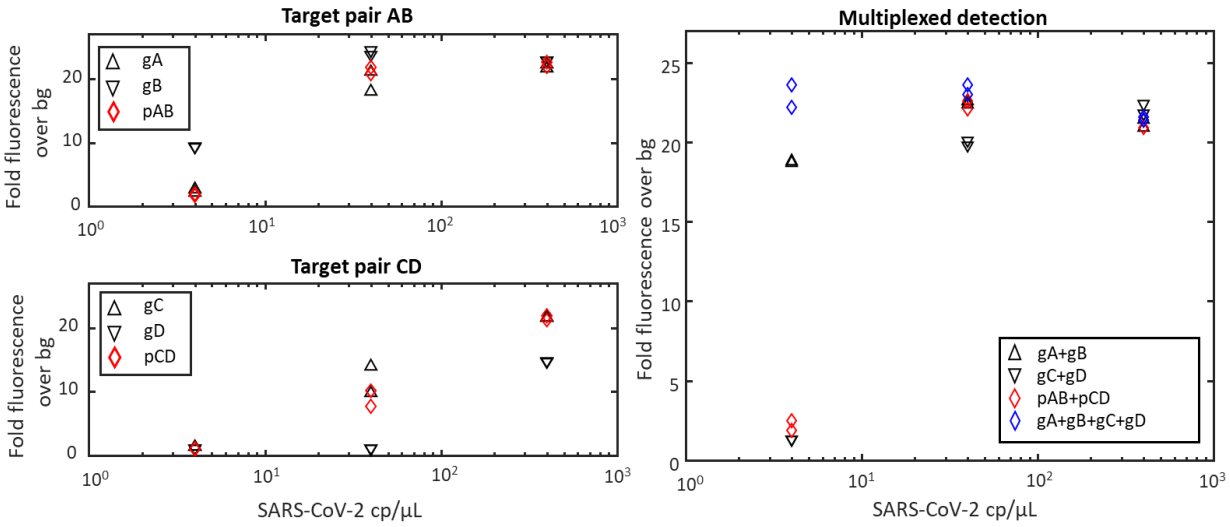

Note. In a SHERLOCK-type Cas13 viral diagnostic assay, Cas13 with single pgRNAs (recognizing two sites, left) or two pgRNAs (recognizing four, right) could robustly generate detectable signals in the presence of samples initially containing 40 cp/uL heat-inactivated SARS-CoV-2 (Whereas clinically relevant LOD for SARS-CoV-2 is often considered as 1000 cp/uL [28]).

These findings suggest that pgRNAs are suitable for *in vitro* viral detection applications involving multiple viral targets, offering simplicity in assembly or operation and potentially lower cost per reaction compared to multiplexed detection using monovalent gRNAs. In

addition, the use of pgRNAs can enhance assay robustness in the face of genetic variation across clinical variants. This is especially pertinent in scenarios where it may be unlikely for variants to exhibit numerous mutations at both targeted sites simultaneously. For instance, a variant with a significant insertion or deletion (indel) at one site might go undetected in a CRISPR-based viral detection assay using a monovalent gRNA specific to that site. However, the probability of a variant possessing large indels at all multiple sites recognized by a single pgRNA is lower. Moreover, the design principles of pgRNAs can be extended to develop broad-spectrum Cas13-based viral diagnostics [40] tolerant to polymorphisms within a viral family. This strategy holds significant value for monitoring emerging pathogens. In such scenarios, the advantages of CRISPR-based viral diagnostics, particularly isothermal detection, become of utmost importance, especially in remote or resource-constrained settings, as opposed to PCR-based diagnostics.

Engineered pgRNAs Induce Cas9 dsDNA Cleavage with Up to 40% Divergence in Ex Vivo Target Pairs

Finally, we aimed to investigate whether the design principles applied to pgRNAs in Cas13 could be extended to gRNAs for other CRISPR effectors, such as the Cas9 effector from Streptococcus pyogenes (SpyCas9), known for recognizing and inducing double-strand breaks in dsDNA targets (Figure 15A).[21] For Cas9 from S. pyogenes, we designed a pgRNA (pg) along with its two "monovalent" counterpart gRNAs (gA and gB) to target two sequences with a 30% difference (6 out of 20 nt) in their protospacer region and 1 out of 3 differences in their protospacer adjacent motif (PAM) region (Figure 15B). Cas9 with monovalent guides shows no cross-reactivity at homoeologous sites, while Cas9 with the engineered pgRNA demonstrates robust cleavage activity at both sites (Figure 15C).

Figure 15. pgRNAs Engineered to Stimulate Cas9 dsDNA Cleavage Activity at Divergent Target Pairs

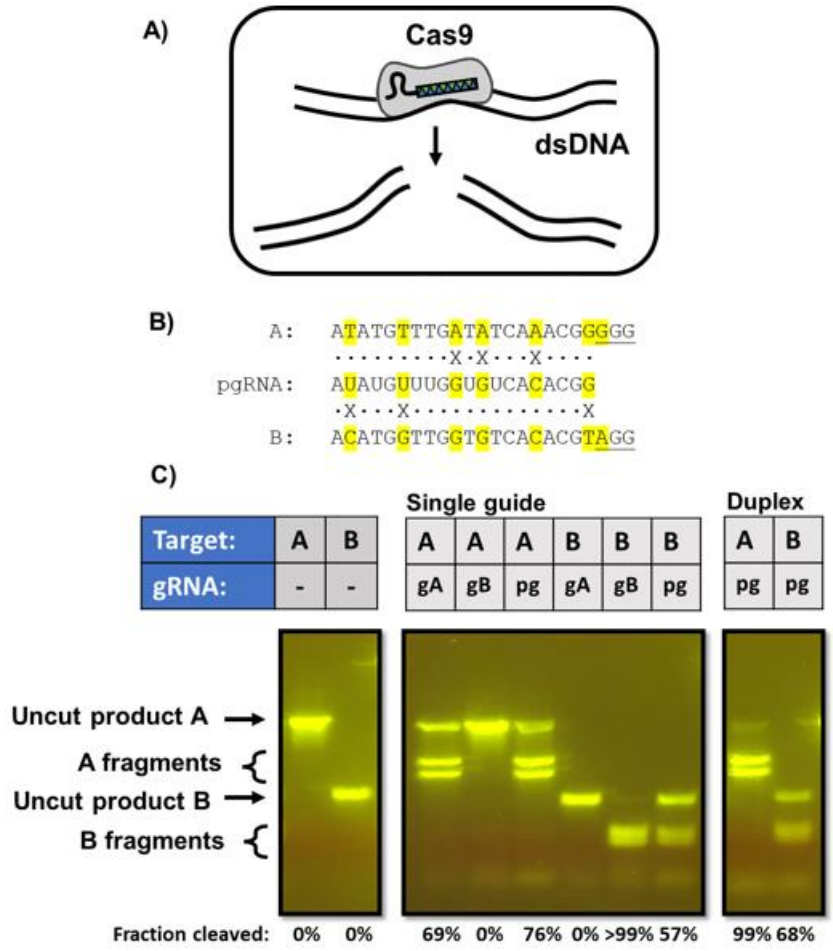

Note. (A) Cas9 from S. pyogenes recognizes and cleaves dsDNA. (B) A pgRNA (pg) and its two "monovalent" counterpart gRNAs (gA and gB) for Cas9 was designed to target two sequences that differ by 6 of the 20 nt (30%) in their protospacer region, and 1 out of 3 within their protospacer adjacent motif (PAM) region (underlined). (C) Cas9 with monovalent guides exhibit no cross-reactivity at homoeologous sites, while Cas9 with a pgRNA exhibits robust cleavage activity at both sites. pgRNA activity is enhanced with a crRNA: tracrRNA duplex compared to a chimeric "single guide" RNA.

Subsequently, we developed pgRNAs to address homoeologous pairs of DNA sequences displaying up to 50% sequence divergence, representing differences at a maximum of 10 out of the 20 bp sites in the SpyCas9 protospacers (Figure 16). We then assessed the cleavage activity of purified Cas9 RNPs at these sites *ex vivo*. Some of these sequences were identified from DNA viruses or retroviruses as potential targetable pairs, while others were intentionally designed for exhibiting maximum polyvalency (Figure 16). Like Cas13, SpyCas9 with "monovalent" (perfectly matched) gRNAs demonstrated no cross-reactivity at paired sites characterized by such high sequence divergence. In contrast, SpyCas9 RNPs with pgRNAs consistently exhibited the ability to cleave both targets, even when the paired sequences diverged by up to 40% (Figure 16 and Figure 17).

It is noteworthy that in instances where the pgRNA displayed activity at only one target, those targets exhibit up to 5 mis-paired nucleotides between the engineered pgRNA and the protospacer. Additionally, we observed that the inclusion of a leading 5'-rG on the spacer, a condition believed to enhance specificity in CRISPR activity for gene editing applications,[41] resulted in a reduction of pgRNA activity at both sites (Figure 18). Thus, through the optimization of tolerance for mismatches between the spacer sequence and targeted sites, we demonstrate that pgRNAs can be tailored to facilitate high levels of SpyCas9 cleavage activity at multiple targeted DNA sequences simultaneously *ex vivo.*

Figure 16. pgRNAs Designed to Target Homoeologous Pairs of DNA Sequences Displaying Up to 50% Sequence Divergence *ex vivo* at Synthetic Targets and Original Target Sequences found in DNA Viruses or Retroviruses

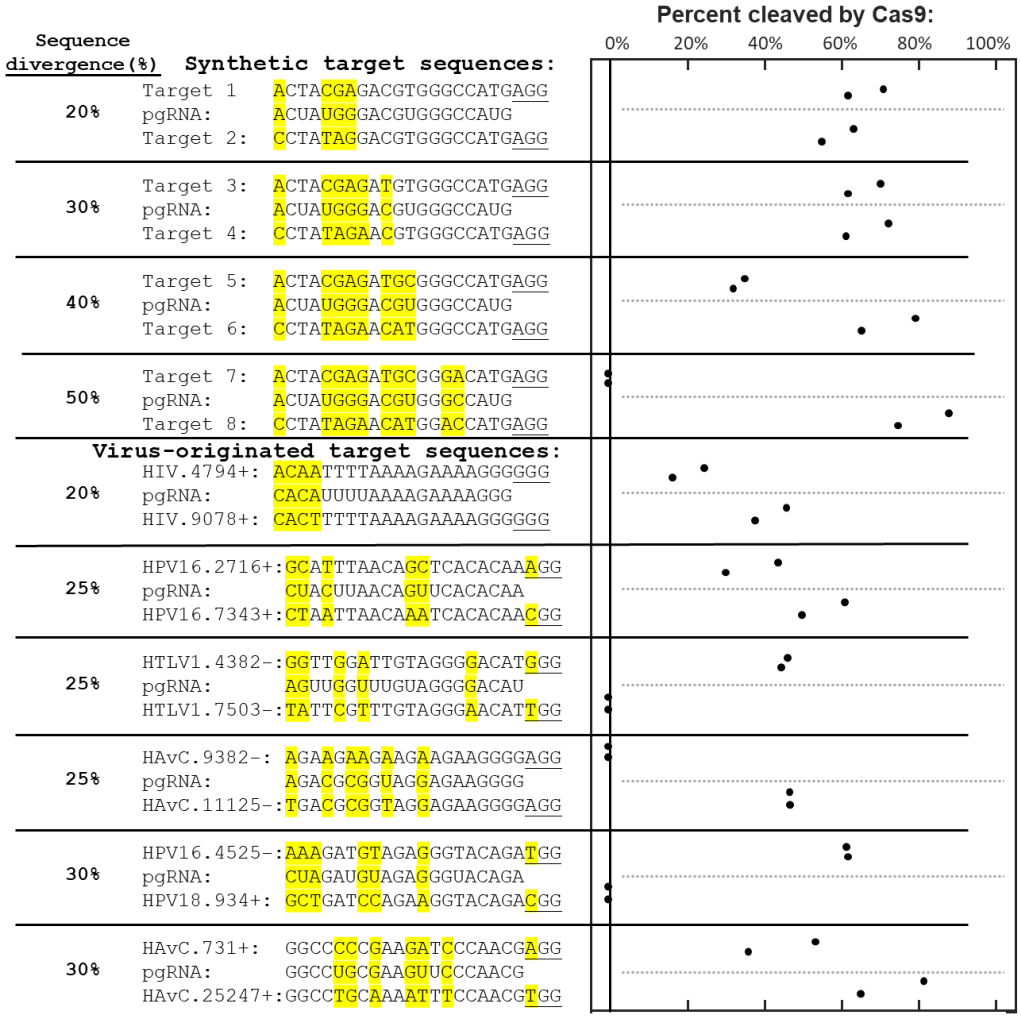

Note. pgRNAs could be generated for SpyCas9 to exhibit robust cleavage activity *ex vivo* at pairs of synthetic targets (upper) and target sequences originally found in DNA viruses or retroviruses (lower) with sequences diverging by up to 40%. HIV: Human Immunodeficiency Virus type 1; HPV16: Human papillomavirus type 16; HPV18: Human papillomavirus type 18; HTLV1: Human T-lymphotropic virus 1; HAvC: Human Adenovirus.

Figure 17. Agarose Gel Electrophoresis of Cas9-pgRNA Cleavage Products of Synthetic Targets with Increasing Divergence; Related to Figure 16

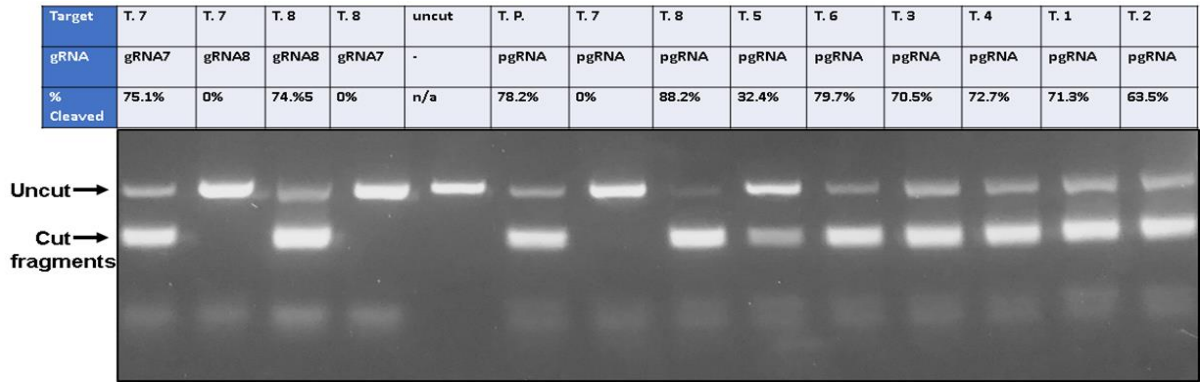

Figure 18. Agarose Gel Electrophoresis of Cas9-gRNA Cleavage Products under Different *in vitro* Conditions Typically Optimized for Gene Editing

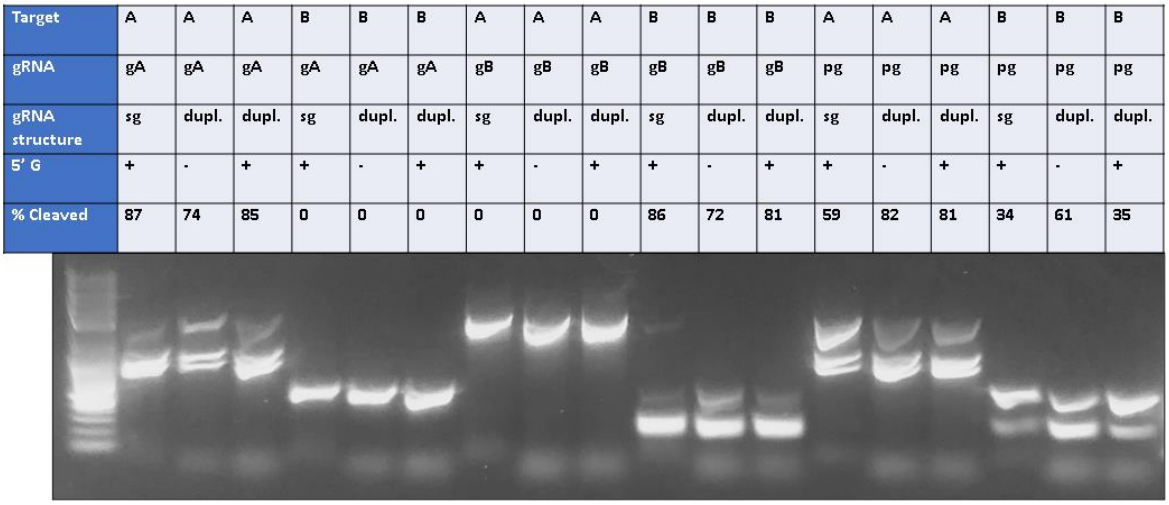

Note. gRNAs marked with 5'- have 21 bp long spacers with an unpaired 5'- G. Those with 'sg' gRNA structures were transcribed *in vitro* as 'single guides RNAs' (sgRNA) that fuse the crRNA and tracrRNA in continuous RNA molecule, while for 'dupl.' (duplex) the crRNA was synthetized (IDT; Coralville, IA) and hybridized with a tracrRNA (IDT) prior to incubation with the Cas9. Related to Figure 17.

Discussion

The CRISPR effector proteins, initially discovered in bacteria and archaea as an antiviral defense mechanism against foreign DNA and RNA,[42] inherently exhibit some tolerance to sequence variation in their targets. In the context of gene editing applications, extensive efforts are usually directed towards minimizing the natural tolerance of CRISPR effectors for nucleic acids with imperfect complementarity to their guide RNAs (gRNAs) to prevent unintended degradation and mutation at "off-target" sites. However, in this study, we leverage these tolerances to engineer gRNAs termed, polyvalent guide RNAs (pgRNAs), optimized for simultaneous activity at multiple viral target sites. It is noteworthy that, our engineered pgRNAs simultaneously target multiple viral sites without increasing the risk of "off-target activity" by maintaining significant divergence with the host genome.

Moreover, we validated our algorithm through experimental implementation. Experimentally, pgRNAs with Cas13 exhibited remarkable antiviral efficacy in *Nicotiana benthamiana*, a model tobacco organism, even with multiple mismatches or non-canonical base-pairings with their viral targets. The reduction in viral RNA across a tissue was 30- to 40-fold compared to monovalent gRNAs, showcasing the superior performance of pgRNAs. Furthermore, the effectiveness of single pgRNAs rivaled or surpassed treatments using two multiplexed "monovalent" gRNA counterparts. Notably, the application of multiplexed pgRNAs targeting four viral sequences demonstrated even greater efficiency, achieving a reduction of detectable viral RNA in planta by over 99.5% compared to monovalent gRNAs.

Additionally, we verified our algorithm *in vitro*. *In vitro* experiments demonstrated that pgRNAs, despite imperfect complementarity, could be tailored to induce Cas13's "collateral activity" for viral detection at viral target pairs with sequences diverging by up to 25%.

Moreover, these pgRNAs were capable of guiding DNA-targeting CRISPR-Cas9 to degrade multiple DNA targets ex vivo, even with sequence divergence reaching 40%, involving mismatches at 8 out of 20 base pairs.

The notable improvement in performance observed with pgRNAs, whether employed singly or in multiplex, compared to single gRNAs is particularly striking. This is noteworthy, given that the pgRNA spacer sequence includes up to three or four mis-paired nucleotides with each of its two targets. We propose that the heightened efficacy of pgRNAs in suppressing viral propagation may be intricately linked to the kinetics of CRISPR effector recognition in the context of a rapidly replicating RNA virus—a feature that holds greater significance in antiviral applications compared to other CRISPR biotechnologies.

In situations involving multiplexed targeting with N distinct "monovalent" gRNAs, where the amount of transfected CRISPR effector is likely constrained, this multiplexing effectively diminishes the number of effectors per target by 1/N. While multiplexed targeting aids in averting viral mutagenic escape, this effective reduction in effector concentration per target may significantly impact the rate at which each CRISPR effector can locate and degrade its viral target within a rapidly replicating RNA virus in a eukaryotic cell. Conversely, a CRISPR effector equipped with a single pgRNA that can recognize N viral sites while maintaining high activity at each site now has N-fold the number of viral targets it can potentially recognize. This augmentation in the rate of viral recognition per effector, even surpassing effectors with perfectly matched "monovalent" gRNAs that can only recognize a single viral site, may influence the kinetics of effector recognition and degradation. This impact on kinetics, potentially less critical in gene editing applications or even in applications of Cas13-mediated "knock-down" of mRNA transcripts from a discrete set of chromosomal genes than for a viral targest which are dynamic

entities and replicate rapidly within a host cell. Our findings in planta suggest that the "polyvalency" of pgRNAs can offset any potential reduction in activity at their target sites, thereby amplifying their antiviral activity with Cas13 compared to their perfectly complementary monovalent counterparts.

Despite the aforementioned capabilities of our designed pgRNAs for CRISPR antiviral applications, there are some limitations. For instance, while our pgRNA design algorithm minimizes interactions with the host genome or transcriptome through bioinformatics, experimental evaluation of potential off-target effects for each viral target and (p)gRNA sequence is crucial to ensure safety, especially for DNA-targeting CRISPR enzymes like Cas9. Additionally, our study utilized Cas13 in *N. benthamiana* plants as a proof-of-concept to demonstrate the superiority of pgRNAs in antiviral CRISPR applications. Further research is necessary to determine whether pgRNAs can effectively combat human viruses in human cell lines. Another potential issue concerns the potential toxicity stemming from Cas13's collateral activity.[37, 43] However, our plant-based study suggested phenotypic health. This toxicity was observed in animal cell lines and transgenic animals under conditions of high expression of both Cas13 and its target during extended periods of targeted RNA knockdown, a scenario that might not be necessary for antiviral applications. Nonetheless, it remains to be established whether Cas13's collateral activity is indispensable for its in vivo antiviral effects. If it turns out to be non-essential, engineered Cas13 variants with targeted activity but minimized collateral activity [37] or alternative RNA-targeting CRISPR effector Cas7-11 that lacks collateral activity [43] could present potentially safer alternatives. Additionally, while previous studies in human cell lines did not find evidence of elevated mutation rates in CRISPR-targeted viruses,[17] further work is

needed to evaluate the "long-term" effects of CRISPR antivirals on the mutation rate of viral targets.

Nevertheless, our gRNA design algorithm is specifically tailored to address key considerations in CRISPR antiviral applications, such as multiplexing and preventing escape, as well as accommodating clinical variation and viral sequence heterogeneity. Furthermore, while pgRNAs were designed specifically for CRISPR antiviral applications, our results demonstrate that our design principles also apply to both RNA- and DNA-targeting CRISPR effectors. Hence, pgRNAs could, in theory, be crafted for "polyvalent" genome editing through CRISPR, particularly for the knockout of members within extensive orthologous gene families, where achieving comprehensive coverage across the entire family might pose challenges with traditional multiplexed gene editing approaches utilizing numerous "monovalent" guides.

Experimental Methods

Construction of RfxCas13d for in planta Expression

The DNA sequences of the plant codon optimized Cas13d-EGFP with the Cas13d from *Ruminococcus flavefaciens* (RfxCas13d) flanked by two nuclear localization signal (NLS) was amplified from plasmid pXR001 (Addgene #109049) using Q5 high fidelity of DNA polymerase (NEB). Similarly, overlap extension PCR was performed to amplify plant expression vector pB_35S/mEGFP (Addgene #135320) with ends that matched the ends of the Cas13 product so RfxCas13d expression would be under the control of 35S Cauliflower mosaic virus promoter. The PCR products were treated with DpnI (NEB), assembled in a HiFi DNA assembly reaction (NEB), transformed into NEB10b cells (NEB), and grown overnight on antibiotic selection to create plasmid pB_35S/RfxCas13. Successful clones were identified and confirmed by

sequencing followed by transformation into electro-competent *Agrobacterium tumefaciens* strain GV3101 (pMP90).

Construction of crRNA Expression Vector

Single stranded oligonucleotides corresponding to "monovalent", non-targeting (NT), and "polyvalent" gRNAs were purchased from Integrated DNA Technologies (Coralville, IA), phosphorylated, annealed, and ligated into binary vector SPDK3876 (Addgene #149275) that had been digested with restriction enzymes XbaI and XhoI (NEB) to be expressed under the pea early browning virus promoter (pEBV). The binary vector containing the right constructs were identified, sequenced, and finally transformed into *Agrobacterium tumefaciens* strain GV3101.

Agroinfiltration of *Nicotiana benthamiana* (Tobacco) Leaves

In addition to pB_35S/RfxCas13 and the SPDK3876's harboring gRNA sequences (TRV RNA2), PLY192 (TRV RNA1) (Addgene #148968) and RNA viruses TRBO-GFP (Addgene # 800083) were individually electroporated into *A. tumefaciens* strain GV3101. Single colonies were grown overnight at 28 degrees in LB media (10 g/L tryptone, 5 g/L yeast extract, 10 g/L NaCl ; pH 7). The overnight cultures were then centrifuged and re-suspended in infiltration media (10mM MOPS buffer pH 5.7, 10mM MgCl2, and 200 μM acetosyringone) and incubated to 3-4 hours at 28 degrees. The above cultures were mixed to a final OD600 of 0.5 for CasRX-NLS-GFP-pB35, 0.1 for PLY192 (TRV RNA1), 0.1 for RNA2- crRNAs and 0.005 for TRBO-GFP and injected into healthy leaves of five to six-week-old *N. benthamiana* plants grown under long-day conditions (16 h light, 8 h dark at 24 °C). A total of four leaves for each gRNA were infiltrated. Three days post-transfection, leaves were cut out and photographed under a handheld UV light in the dark and stored at -80°C before subsequent analysis.

Quantitative RT-PCR

Total RNA was extracted from infiltrated leaves using RNeasy Plant Mini Kit (Qiagen) and the yield was quantified using nanaodrop. A total of 1ug RNA from control (NT gRNAs) and experimental samples were used for DNase I treatment (Ambion, AM2222) followed by reverse transcription using a poly-dT primer and the Superscript III First Strand cDNA Synthesis System for RT–PCR (Invitrogen). Quantitative PCR was performed on Quant studio 3 Real-Time PCR System from Applied Biosystem using iTaq PowerUP^{TM} SYBR Green pre-formulated 2x master mix (Applied Biosystems). Relative expression levels based on fold changes were calculated using the ddCT method. Cycle 3 GFP mRNA expression levels from the TRBO-GFP replicon were normalized against transcripts of the tobacco PP2A. The samples were performed in three biological replicates.

Cas13 Collateral Activity Assays

Initial screens were performed using synthetic dsDNA (~300 bp) containing a T7 promoter located upstream of a specific target sequence derived from either SARS-CoV-2 or human *CD46* transcript sequencesin two steps as follows: 1 µl *Leptotrichia wadeii* Cas13a (LwaCas13a) enzyme (106 ng; Molecular Cloning Laboratories, South San Francisco, CA, US) was preincubated with each pre-synthesized gRNA (CD46 targets) [0.25µM; Integrated DNA Technologies, Coralville, Iowa, US (IDT)] or *in vitro* transcribed gRNA (SARS-CoV-2 targets) [0.25µM; NEB] in a total volume of 5 µl for 10 min at room temperature, followed by the addition of 16 µl of synthetic dsDNA template (Twist Biosciences, South San Francisco, CA, US) at varying concentrations ($4.0x10^5$ cp/µl , $4.0 x10^7$ cp/µl, or $4.0x10^9$ cp/µl at final concentration for SARS-CoV-2 targets and $1.0x10^9$ cp/ul for CD46 targets). A master mix containing 0.5 µl of T7 RNA polymerase [New England Biolabs, Ipswich, MA, US (NEB)], 1 µl

of 25mM rNTPS (at equal ratios of rATP, rUTP, rGTP, rCTP; NEB), 0.23 µl 1M MgCl2 (Invitrogen ThermoFisher, CA US), 0.5 ul HEPES (Invitrogen ThermoFisher ,CA US), 0.63 µl of RNAseH inhibitor (NEB), 1.56 µl RNAse Alert Reporter (IDT), and 0.58 ul of nuclease-free water (Invitrogen) were assembled on ice and 4 µl added to the mixture containing the DNA template and preincubated Cas13 RNP. 25 µl of each preassembled reaction was added to a 384 well plate (Black/Clear Bottom) and loaded into a preheated fluorescence microplate reader (Promega GloMax Explorer) at 37˚C. Data readouts were collected every 5 min for 1 hr at an excitation peak at 480 nm and an emission peak at 520 nm.

Specificity of Cas13 collateral activity was evaluated using dsDNA fragments that were not complementary to the gRNAs being tested to confirm that activation of collateral activity as well as human universal RNA (10 tissues) (Invitrogen ThermoFisher, CA US), and total human lung RNA (Invitrogen ThermoFisher, CA US), was also used at 1 and 3 ug, respectively per reaction.

SHERLOCK-Type Viral Detection Reactions

Heat-inactivated SARS-CoV-2 RNA from respiratory specimens, deposited by the Centers for Disease Control and Prevention, was obtained through BEI Resources, NIAID, NIH: Genomic RNA from SARS-Related Coronavirus 2, Isolate USA-WA1/2020, NR-52285 (American Type Culture Collection (ATCC) VR-1986HK). In a SHERLOCK-type reaction, 1 µl of heat-denatured SARS-CoV-2 (350,000 copies total) was reverse transcribed using the High Capacity cDNA Reverse Transcription Kit (Thermo Fisher Scientific) with 3.4 µl of primer (0.5µM) in a final volume of 16 µl and PCR-amplified by the addition of 2 µl of reverse and forward target primers (2 µM) and 20 µl of 2 x OneTaq Master Mix (NEB) in a final volume of 40 µl under standard thermocycler conditions (2 min at 95 °C, followed by 35 cycles of 30 s at

95 °C, 30 s at 49°C, and 30 sec at 68 °C, followed by a final extension of 5 min at 72 °C). Reactions were diluted to 4, 40, or 400 cp / uL of the starting viral material [22] for each target and Cas13 collateral activity assays were performed as described above. Collateral activity assays using Cas13 proteins with no gRNA were also evaluated to provide equivalent background signals.

Generation of Cas9 Target Sequences

Cas9 DNA targets in Table 4 were generated by either (1) using plasmids containing targets or PCR amplification of targets in plasmids using primers.

Plasmids were purified using Monarch Plasmid Miniprep Kit following standard protocols (NEB, New England Biolabs, Ipswich, MA). PCR amplification was carried out using 4.5 ng of plasmid DNA, downstream and upstream PCR primers (IDT, Integrated DNA Technologies, Coralville, Iowa, United States) at a final concentration of 0.2uM, and Taq 2x Master Mix (NEB, New England Biolabs, Ipswich, MA, United States) following standard thermocycling protocols. Amplified PCR targets were purified using a Monarch PCR and DNA cleanup kit (NEB) following standard protocols. DNA oligonucleotides were hybridized to form duplex DNA targets by using equal molar concentration of oligos (IDT, Integrated DNA Technologies, Coralville, IA) to a final concentration of 10uM in nuclease-free IDT Duplex buffer. Reactions were heated to 95ºC for 2 min and allowed to cool to room temperature prior to the reaction assembly.

***in vitro* Transcription of Cas9 gRNAs**

Single guide RNA (sgRNA) was synthesized by using the EnGen sgRNA synthesis Kit (NEB, New England Biolabs, Ipswich, MA, United States) following standard protocols. DNA oligos (IDT) were designed to contain a T7 promoter sequence upstream of the target sequences

with an initiating 5'- d(G), as well as overlapping tracrRNA DNA sequence at the 3' end of the target. The sgRNA was purified using Monarch RNA Cleanup Kit (NEB) and quantitated using standard protocols.

Duplex gRNA Generation

Duplex CRISPR gRNAs (cRNA:tracrRNA) was generated by hybridizing synthetic RNA oligos to a universal synthetic tracer RNA oligo (IDT). To hybridize oligos, equal molar concentration of oligos were combined in IDT duplex buffer to a final concentration of 10uM. Reactions were heated to 95^{o}C for 2 min and allowed to cool to room temperature prior to the reaction assembly.

Cas9 Cleavage Reactions

Our computational tools for designing pgRNAs for Cas9 and Cas13 are publicly available at https://www.github.com/ejosephslab/pgrna (DOI:10.5281/zenodo.7126522). Cas9 Nuclease from *S. pyogenes* (NEB) was diluted in 1x NEB Buffer 3.1. prior to the reaction assembly. Cas9 cleavage activity was performed using either PCR-amplified targets, whole plasmid, or hybridized DNA oligos containing desired targets using standard methods. Briefly, Cas9 was preincubated with either a sgRNA or duplex gRNA (crNA:tracRNA) for 5 min at equal molar concentrations in 1x NEB Buffer 3.1 (NEB) in a volume total of 10 ul. Reactions were incubated for 5-10 min at room temperature. Target DNA was then added to the reactions, NEB Buffer 3.1 was added back to a final concentration of 1x, and nuclease-free water was added bringing the final volume to 20 ul. The final reaction contained 100nM Cas9-CRISPR complex and 10nM of target DNA. Similar reactions without the addition of gRNAs to Cas9 were used as a control for uncut DNA. Reactions were incubated at 37^{o}C for 1 hour, followed by the addition of 1 unit of

Proteinase K and further incubation at 56ºC for 15 min. Reactions were stopped by the addition of one volume of purple Gel Loading dye (NEB).

Fragments were separated and analyzed using a 1.5% Agarose gel in 1xTAE and 1X SYBR Green 1 Nucleic Acid Gel Stain (Thermo Fisher Scientific; Waltham, MA), and fluorescence was photographed and measured (AmershamTM Imager 600; GE Life Sciences, Piscataway, NJ, United States).

Resource Availability

Code Availability

Our computational tools for designing pgRNAs for Cas9 and Cas13 are publicly available at https://www.github.com/ejosephslab/pgrna (DOI:10.5281/zenodo.7126522).

CHAPTER II: COMPARTMENTALIZED CRISPR REACTIONS (CCR) FOR HIGH-THROUGHPUT SCREENING OF GUIDE RNA POTENCY AND SPECIFICITY

Abstract

The sequence of a variable segment called a spacer in the guide RNA (gRNA) of a CRISPR effector determines the sequence at which the effector will exhibit nuclease activity to generate target-specific mutations in living cells. However, nuclease activity with different gRNAs can vary considerably, in a spacer sequence-dependent manner that can be difficult to predict. While computational tools are helpful in predicting a CRISPR effector's activity and/or potential for off-target mutagenesis with different gRNAs, individual gRNAs must still be validated in vitro prior to their use. Here, we present compartmentalized CRISPR reactions (CCR) for screening large numbers of spacer/target/off-target combinations simultaneously in vitro for both CRISPR effector activity and specificity, by confining the complete CRISPR reaction, including gRNA transcription and target cleavage within individual water-in-oil microemulsions. With CCR, large numbers of the candidate gRNAs output by computational design tools can be immediately validated in parallel, and we show that CCR can be used to screen hundreds of thousands of extended gRNA (x-gRNAs) variants that can completely block cleavage at off-target sequences while maintaining high levels of on-target activity. We expect CCR can help to streamline the gRNA design and its validation process for applications in biological/biomedical research.

Introduction

The Clustered Regularly Interspaced Short Palindromic Repeats (CRISPR) and CRISPR-associated protein 9 (Cas9) system has emerged as a robust method for targeted gene editing,[44, 45]

allowing precise and efficient modifications of specific nucleic acid sequences within a genome. The process relies on guide RNAs (gRNAs) that are designed to complement target DNA sequences in a modular segment called their spacer.[46, 47] Stable base-pairing between the spacer sequence and the target sequence activates the Cas9 nuclease domains to cleave the DNA.[46-50] When Cas9 cleavage occurs within a cell, cellular double-strand break repair (DSB) mechanisms can introduce permanent genetic modifications within its genome at the cleavage site. Therefore, by simply alternating the sequence of the gRNA's spacer, Cas9 can be employed to introduce specific mutations into a gene of interest.[51 -54] These mutations typically involve insertions or deletions during mutagenic DSB repair,[53,54] potentially resulting in a frameshift knockout of the gene,[51, 52] making it a highly useful tool for biological studies and gene therapies.[44, 45]

However, the molecular mechanism of target recognition and cleavage by Cas9 is intricate. It involves, search for a Protospacer Adjacent Motif (PAM) site [50], followed by a strand invasion,[47] and a conformational change driven by the formation of a stable R-loop [55, 56] that positions the nucleases appropriately. Predicting Cas9 nuclease ability to recognize and degrade different sequences is challenging due to this complex process, unlike the design of PCR primers, which is mainly driven by the thermodynamics of base-pairing.[57, 58] The strand invasion of the guide RNA (gRNA) is believed to be a kinetic and non-equilibrium process.[46, 47, 48, 55, 56] Consequently, it leads to significant variability in Cas9 efficacy based on various properties of the gRNA's spacer sequence.[59 - 69] Significant efforts have been put in predicting the activity of Cas9,[59 - 69] and consequently various machine learning models[61, 66- 68] have emerged as valuable tools to determine gRNA candidates to target a gene of interest. Once a gene of interest has been identified, possible targets (with a 3'- PAM) are enumerated, and computational tools[59 - 68] are then employed to identify the most promising candidates.

Moreover, the nuclease domains of Cas9 can also be activated at off-target sequences that are similar but not identical. This occurs If during strand invasion the gRNA is able to stably bypass the incorrectly paired nucleotides. Therefore, off-target effects are also considered in addition to predicting activities at different target sites.[59, 61, 70-75] The computational tools enumerate all possible targets identified by the presence of the requisite PAM in proximity and then assessed activity at both on-targets and potential off-targets sites. In practice, there are trade-offs between the anticipated on-targets and potential off-target activities when deciding which candidate gRNAs to validate manually.[75]

Consequently, translating the outcome of computational tools poses challenges due to potential contradictions among different models for evaluating on-target, off-target efficacy, and double-strand break (DSB) repair outcomes.[75] Therefore, multiple gRNAs often need to be tested manually or validated [76, 77] *in vitro* to effectively induce desired mutations in cells. However, this process can be laborious, involving the transcription, purification, and individual reaction of gRNAs. Moreover, evaluating numerous spacer/target/off-target combinations present practical challenges.[76-78] Conducting these high-throughput screenings within mammalian cell lines[79 - 82] is also a challenging endeavour due to the low efficiency of the transfection process. Additionally, conducting CRISPR screening assays in bulk aqueous volumes becomes complex, as interactions occur among neighboring DNA templates,[83, 84] leading to a lack of physical isolation between individual guide RNAs (gRNAs) and their corresponding DNA templates.

To tackle these challenges, inspired by the concept of compartmentalized self-replication (CSR),[83-85] we introduce a streamlined protocol that we call a Compartmentalized CRISPR Reaction (CCR) screen. In CCR screen, libraries of short (<500 bp), specially designed DNA molecules are individually confined within micron-sized water droplets in water-in-oil emulsions

along with high concentrations of T7 RNA polymerase and Cas9 nuclease. The emulsification process involves slowly adding the aqueous phase in a dropwise manner to a stirring mixture of mineral oil and surfactants. The DNA molecules contain the coding sequence for a gRNA downstream of a promoter for T7 RNA polymerase, as well as a targeted DNA sequence (or off-target) on the opposite end of the DNA molecule. Under buffer conditions we have identified where both T7 RNA polymerase and Cas9 were found to be active, the gRNAs encoded on the isolated DNA molecules are transcribed and can associate with the Cas9 nucleases to form the active Cas9 RNP, which can then interact with the target sequence found on the same molecule within the emulsions.

Thus, the non-interacting water droplets in the microemulsion system serve as microreactors [83 – 93] for conducting high-throughput *in vitro* CRISPR reactions while effectively preventing interactions between the neighbouring DNA molecules, thereby circumventing mispairing of the CRISPR guide RNAs (gRNAs). It should be noted that the standard protocol for *in vitro* digestion with the Cas9 nuclease protein involves the prior synthesis and purification of gRNAs specific to the target sites. In present study, we have demonstrated the feasibility of performing CRISPR cleavage reactions in a single-pot manner, bypassing the need for external gRNA synthesis.

Next, we tested the utility of the CCR approach by testing the on-target activity of all 18 possible spacers capable of targeting sequences within the 126 bp exon 1 of the human gene *EMX1* (Chr2:72933825-72933951 in the hg38 assembly) as predicted by different computational CRISPR guide RNAs (gRNAs) design algorithm.[59-68] We also utilized the CCR method to screen for off-target activity at the potential off-targets sites determined by CRISPOR algorithm [75] for five different gRNAs. Finally, we have illustrated application of CCR approach to screen a large

library of extended guide RNAs (x-gRNAs).[94, 95] Extended guide RNAs (x-gRNAs) are 5' nucleotide extensions to the CRISPR gRNAs and are reported to increase Cas9 gene editing specificity by orders of magnitude. However, all x-gRNAs are not equally efficient and specific. [94, 95] This distinctive screening approach thus offer significant advantages in tackling the challenges associated with currently established high-throughput screening techniques.

Results

Single-Pot CRISPR Reaction Conducted in a Non-Emulsion Setting

The standard protocol for *in vitro* digestion with the Cas9 nuclease protein typically begins with the synthesis and purification of guide RNAs (gRNAs) specific to the target sites. Cas9 protein is then combined with the purified gRNA to form a Cas9-gRNA complex which is then introduced to the target DNA *in vitro*. The Cas9 nuclease, guided by the gRNA, recognizes the target DNA sequence, and induces a double-strand break (DSB). This process is illustrated in Figure 19A. In the current study, we illustrate the viability of conducting CRISPR cleavage reactions in a one-pot approach, eliminating the necessity for external gRNA synthesis. To accomplish this, we initially conducted *in vitro* reactions by introducing the reaction mixture into the aqueous phase at various concentrations of DNA library templates. The reaction mixture includes both T7 RNA polymerase for gRNA synthesis and Cas9 for the formation of the Cas9-gRNA complex. We employed a buffer (NEB 3.1) in the reaction mixture, which we determined to exhibit optimal activity for both T7 polymerase and Cas9 protein Figure 19B. The results of the *in vitro* CRISPR reaction performed in a single-pot manner are depicted in Figure 19C. In this case, we utilized a higher concentration of DNA templates, approximately 300 femtomoles, to ensure the visualization of bands in the electrophoresis gel stained with SYBR Safe dye. For samples containing Cas9, a band around 180 bp was observed, corresponding to the cleaved

large fragment after the reaction with Cas9. In the control sample representing the aqueous phase without Cas9 protein, there was no band around 180 bp. Instead, two other bands were evident—one around 280 bp, matching the length of our uncut DNA template, and another around 100 bp, representing the sgRNA generated by T7 polymerase. The latter band exhibited a reddish hue in blue light (Figure 19C), confirming the formation of sgRNA. In another control where the aqueous phase did not contain T7 RNA polymerase, only one band around 280 bp was observed, corresponding to the length of the uncut DNA template. As expected, there was no band around 100 bp, indicating the absence of sgRNA generation in the absence of T7 RNA polymerase (Figure 19C).

Figure 19. Single-Pot CRISPR Conducted in a Non-Emulsion Setting

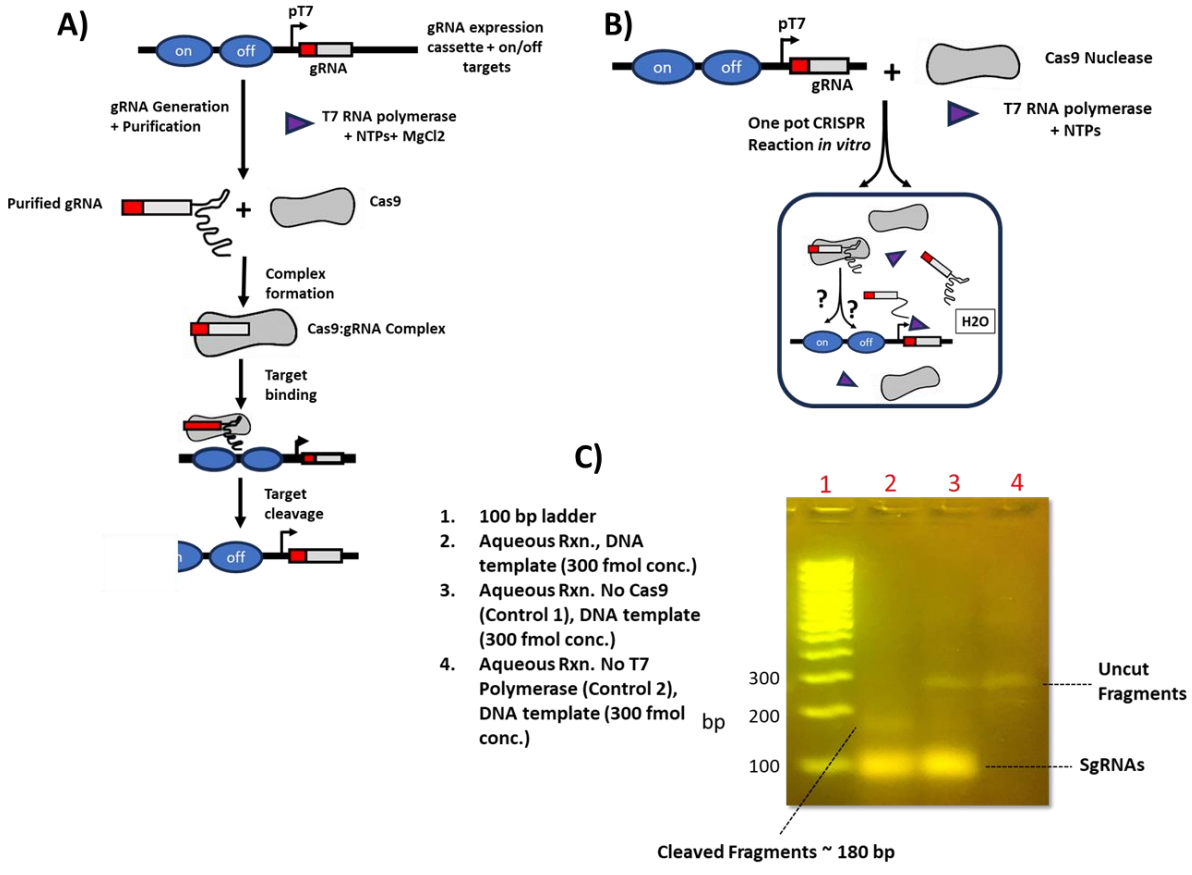

Note. Single-pot CRISPR reaction conducted in an aqueous bulk phase, eliminating the necessity for external CRISPR gRNA synthesis. A) The standard protocol utilized for CRISPR-Cas9 cleavage assays. B) Our developed protocol enables performing the CRISPR- Cas9 cleavage assays in a one pot manner C) Representative agarose gel demonstrates the feasibility of one pot CRISPR- Cas9 cleavage assays. Samples without Cas9 effector and T7 polymerase are two controls here. DNA template concentration is ~ 349.2 femtomoles.

Compartmentalized CRISPR reactions (CCR)

Following the theory of compartmentalized self-replication (CSR),[83-85] we then performed the entire CRISPR reaction, including gRNA transcription and CRISPR target cleavage, within individual water-in-oil microemulsions (Figure 20). A back-of-the-envelope calculation indicated that these emulsions contained approximately 3.5×10^{14} microliter-sized water droplets per millilitre of the emulsion mixture. By adding around (0.1 – 1) femtomoles of DNA, we aimed to achieve a ratio of 1 DNA molecule for every 100 - 1000 water droplets, even within the larger water droplets if present. This setup was hypothesized to ensure the isolation of each DNA molecule within its own emulsion while enabling the testing of a substantial number of gRNA/target/off-target combinations independently and simultaneously (Figure 20C).

Figure 20. Protocol for Compartmentalized CRISPR Reactions (CCR)

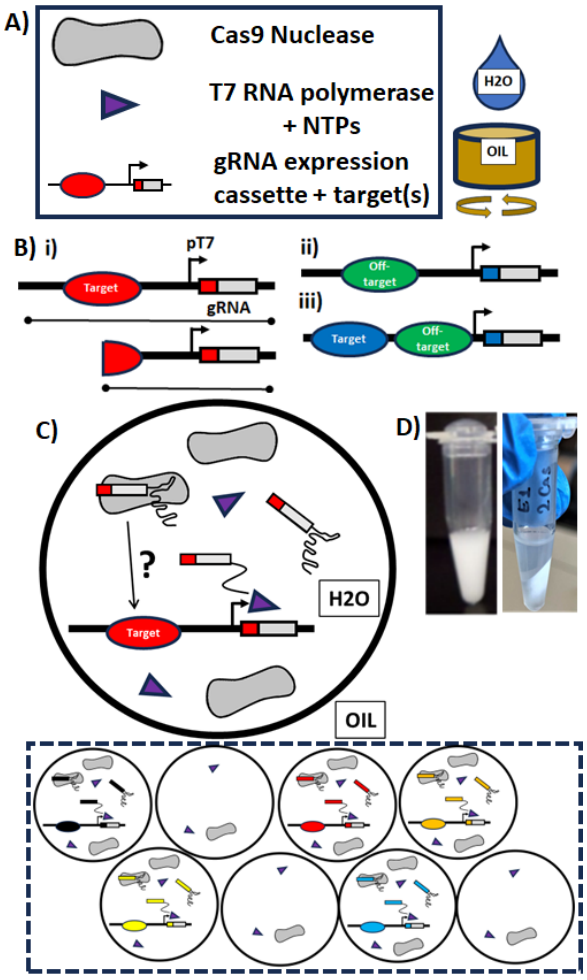

Note. A) Compartmentalized CRISPR Reactions (CCR) are performed in water-in-oil emulsions containing high concentrations of Cas9 nucleases and T7 RNA polymerases with nucleotide triphosphates (NTPs) for RNA transcription, and low concentrations of DNA substrates so that individual DNA molecules are expected to be isolated within a single emulsion. B) The DNA substrates are designed to contain a module for T7 RNA polymerase based expression of a gRNA and (i) a target for Cas9 with that gRNA, so that activity of the Cas9 within that emulsion that with specific gRNA can be determined from the length of the resulting DNA substrates with that spacer sequence (red); (ii) a potential off-target site (green)

for a gRNA of interest (blue); or (iii) a combination of both, where DNA molecules predominantly exhibiting cleavage patterns at the spacer-distal site would imply a gRNA with significantly higher activity on-target than at spacer-proximal off-target sites. C) (above) Within each emulsion, unique gRNAs are transcribed from isolated DNA molecules, where they can associate with a Cas9 nuclease then either demonstrate or fail to demonstrate cleavage activity at a (off- or on-) target site of interest. (below) If a library of different DNA molecules with different gRNA/target/off-target combinations (different colours) are used when generating the water-in-oil emulsions, large numbers of gRNA/target/off-target combinations can be evaluated simultaneously. D) (left) Photograph of a water-in-oil emulsions in a microcentrifuge tube; (right) after the emulsions have been broken after the CCR reaction via centrifugation for subsequent analysis.

Subsequently, to assess the efficacy of these emulsions in isolating these independent gRNA generation and CRISPR nuclease events, we designed a pair of DNA molecules each containing a gRNA expression cassette and its corresponding target positioned on the distal end of the DNA molecule. Additionally, the target for the paired gRNA was situated proximally between its target and the promotor (Figure 21A and 21B). This way, if each of the DNA molecules were isolated in their own water droplet, we expect to see DNA with cuts only on at the distal target sites, while if both species of the DNA pair were mixed (each in the same droplet), we expect to see DNA that were cut at the proximal target site. We then performed the *in vitro* reactions in either under standard reaction conditions (with no emulsions) and within the emulsions and determined the size of the resulting DNA molecules after an 8-hour reaction period. Analysis of the reaction products revealed that the DNA molecules under standard conditions were essentially all cut at the proximal target site, as both gRNAs were generated

together and CRISPR RNPs could easy access both respective targets on either molecule. In the emulsions, the overall fraction of cleaved molecules decreased, but those that were cleaved were mostly cleaved at the distal sites (Figure 22A and 22B). This implied that most of the DNA molecules were isolated in individual emulsions that greatly reduced the potential for cross-reaction between RNPs with gRNAs generated from one DNA and the targets positioned on another DNA molecule. However, occasional mispairing of DNA templates was observed in the micro-emulsions, likely due to heterogeneous water droplets, with a few very large droplets potentially containing more than one DNA template per droplet (Figure 22B).

Figure 21. Validation of Compartmentalized CRISPR reactions (CCR) Technique

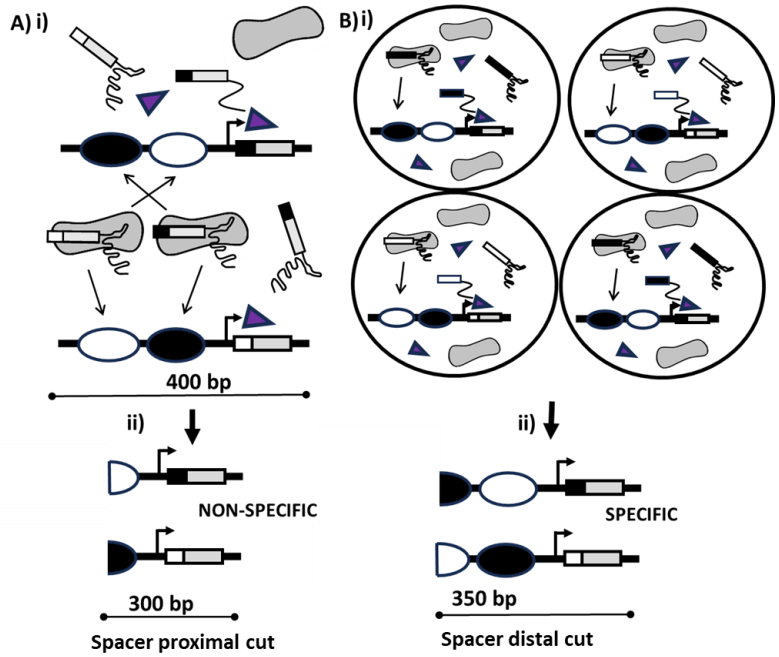

Note. Designed pair of DNA molecules where each contained a gRNA express cassette, its target on the distal end of the DNA molecule, and the target for the other paired gRNA positioned proximally between its target and the promotor. B) If DNA molecules were isolated (as expected in micro-emulsions), we expect to see DNA fragments with cuts only on at the

distal target sites, while A) if both DNA pairs were mixed (as in standard *in vitro* condition), we might expect to see DNA were cut at the proximal target site.

Figure 22. Validation of Compartmentalized CRISPR Reactions (CCR) Technique: Experimental Results

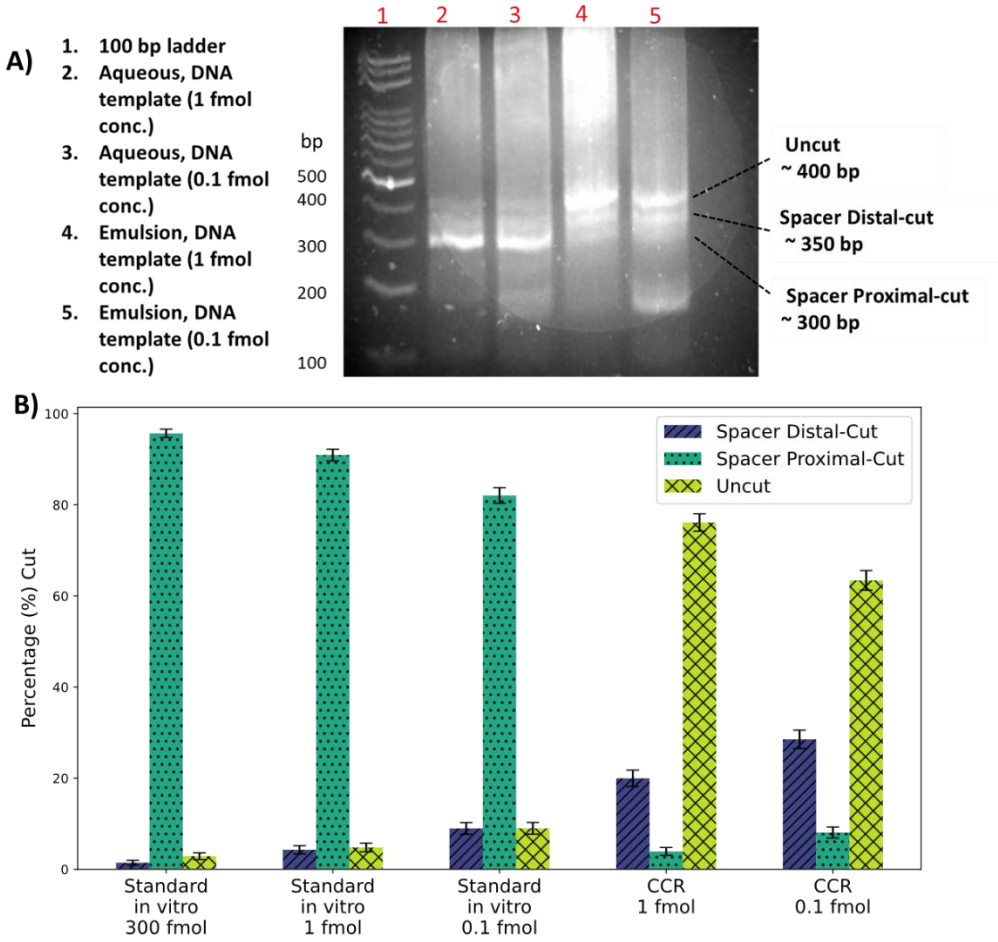

Note. A) Agarose gel image for *in vitro* reaction in either under standard reaction conditions (with no emulsions) and within the emulsions. Lane details are as provided in the figure. B) Analysis of the CRISPR cleavage assays conducted under standard reaction conditions (with no emulsions) and within the emulsions. Under emulsion conditions, a decrease in the overall fraction of cleaved molecules was observed. However, majority of molecules that were

cleaved were mostly cleaved at the distal sites. In contrast, under standard conditions DNA molecules were predominantly cut at the proximal target site, indicating both gRNAs and CRISPR RNPs could readily access both respective targets on either molecule.

Water-Oil Emulsion: Droplet Size Evaluation

We assessed the size of droplets in water-oil emulsions through Dynamic Light Scattering (DLS) technique. Our observations revealed a diameter variation for droplets ranging from 1 to 4 μm, with an average water droplet size of ~2 μm (Figure 23B). Approximately 90% of the water droplets exhibited an average diameter of ~850 nm (+/- 218 nm, standard deviation), while the remaining 10% were larger, with an average diameter of ~4.2 μm (+/- 1.042 μm, standard deviation) (Figure 23B). This finding was further validated through optical microscopy, (Figure 23A). The uneven dispersion of water droplets, particularly the presence of larger droplets, contributes to occasional interactions between templates in emulsion conditions.

Figure 23. Determining the Droplets Size in Emulsions

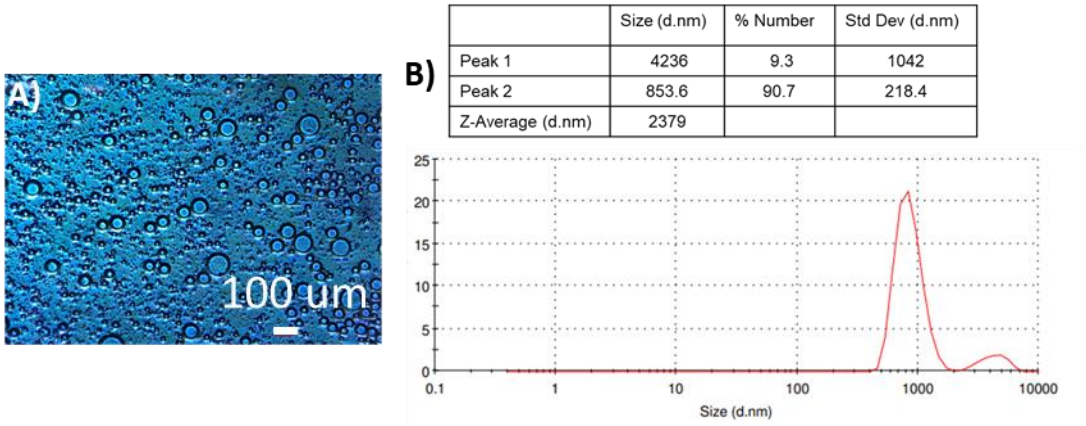

Note. A) Microemulsions generated observed under optical microscope. B) Size of droplets in micro-emulsions measured through Dynamic Light Scattering (DLS).

Simultaneous Evaluation of Cleavage Efficiency of gRNAs Targeting the Human EMX1 Gene Using Compartmentalized CRISPR Reactions (CCR)

An advantage of CCR is elimination of the need of cloning, and the libraries of individual DNA molecules needed for CCR can be synthesized inexpensively. These libraries can also be easily scaled to many members of the library as a pooled set of oligonucleotides, each containing both a unique target candidate and its paired gRNA candidate, that can be amplified using PCR to generate the double-stranded DNA molecules needed for CCR. Considering this, we then tested the utility of the CCR approach for larger screens by evaluating the on-target activity of all 18 possible spacers (Table 1 and Figure 24A) that are capable of targeting sequences within the 126 bp exon 1 of the human gene EMX1 (Chr2:72933825-72933951 in the hg38 assembly). Of those, one gRNA (gRNA 16) has been historically well-characterized for both on- and off-target activities.

Table 1. Eighteen Possible Targets/gRNAs Capable of Targeting Sequences Within the Human EMX1 Gene as Predicted by Various CRISPR gRNA Design Algorithms [59-68]

Targets/gRNAs	Sequences
1	GCTTCGTGGCAATGCGCCACCGG
2	GCGCCACCGGTTGATGTGATGGG
3	GTGGCGCATTGCCACGAAGCAGG
4	TGCGCCACCGGTTGATGTGATGG
5	GCTCCCATCACATCAACCGGTGG
6	TTGCCACGAAGCAGGCCAATGGG
7	CTCCCCATTGGCCTGCTTCGTGG
8	GACATCGATGTCCTCCCCATTGG
9	TGCCACGAAGCAGGCCAATGGGG
10	AGGGCTCCCATCACATCAACCGG

11	CACGAAGCAGGCCAATGGGGAGG
12	TTCTTCTTCTGCTCGGACTCAGG
13	ATTGCCACGAAGCAGGCCAATGG
14	GGAGCCCTTCTTCTTCTGCTCGG
15	TGAGTCCGAGCAGAAGAAGAAGG
16	GAGTCCGAGCAGAAGAAGAAGGG
17	CGGCAGAAGCTGGAGGAGGAAGG
18	GGCAGAAGCTGGAGGAGGAAGGG

CRISPOR,[75] a computational tool for gRNA design, by default reports the efficiency scores or prediction of activity from two common machine learning approaches known as Doench '16 (sgRNA Designer) [59] and Moreno-Mateos (CrisprScan),[60] and it also reports prediction scores for 8 other previously published methods.[61-68] As can be seen (Figure 24A), the different prediction methods are generally inconsistent with one another, with no one gRNA having high predicted efficacy scores across all methods, a situation which can complicate interpretation of these outputs and decision-making regarding which gRNAs are most likely to result in an active RNP. According to trend observed following the CCR screen of all 18 gRNAs simultaneously (Figure 24B), among the top performing RNPs, one includes the well-characterized gRNA (gRNA 16) which we have confirmed is active.[95] Furthermore, the in vitro (using purified RNP complexes reacting individually with DNA molecules) of the top candidates from the CCR screen recapitulated the same trend with gRNA 12 displaying a higher efficiency compared to gRNA 16 and gRNA 10 (Figure 24B inset and Figure 25). These results show that CCR offers a straightforward approach for high-throughput screening and ranking of on-target activity, starting from a pooled oligonucleotide library.

Figure 24. Simultaneous Evaluation of Cleavage Efficiency of gRNAs Targeting EMX1 Gene Using Compartmentalized CRISPR reactions (CCR)

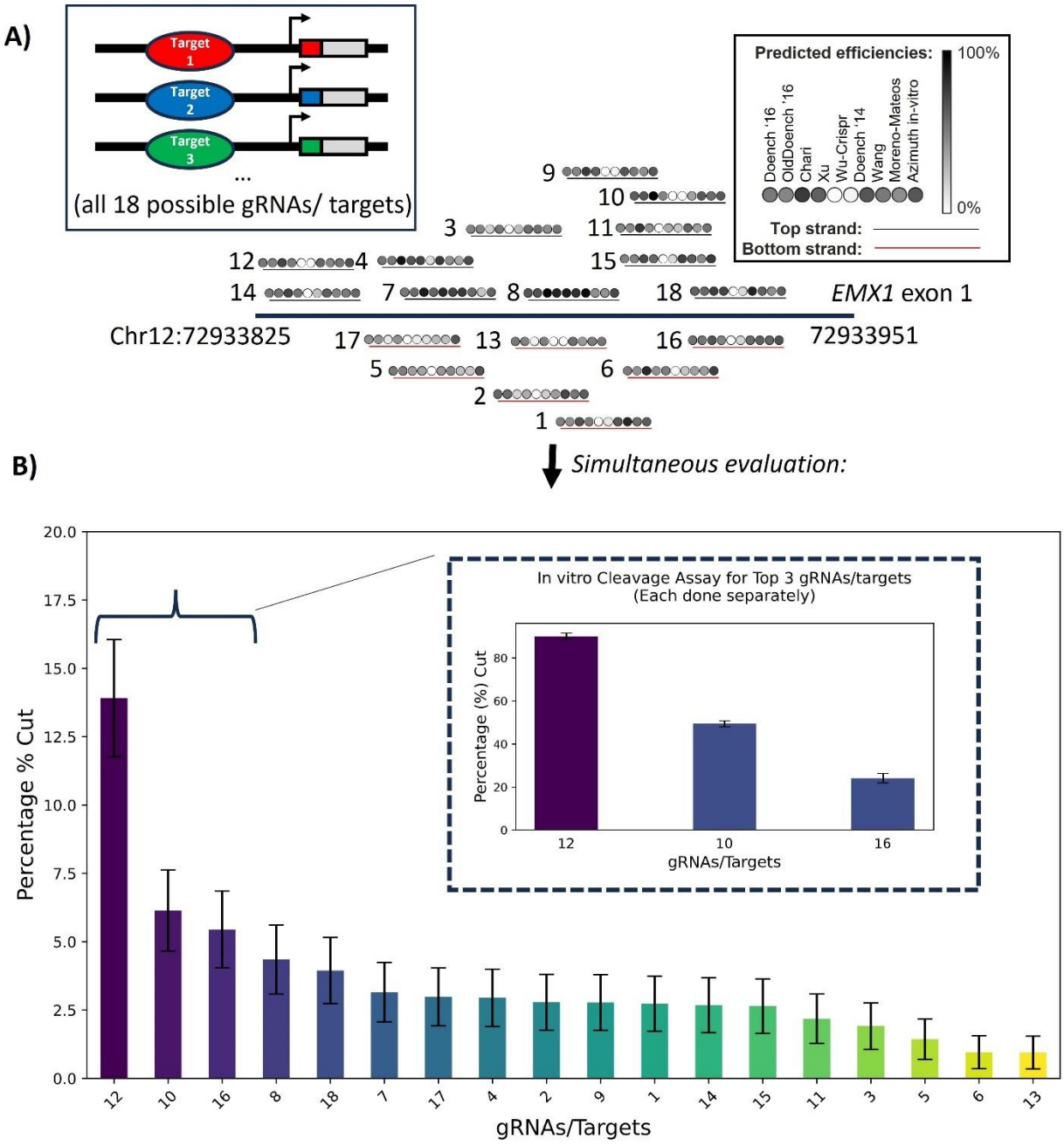

Note. A) All 18 possible spacers capable of targeting sequences within the 126 bp exon 1 of the human gene EMX1 (Chr2:72933825-72933951 in the hg38 assembly) and its cleavage

efficiency as predicted by various CRISPR gRNA design algorithms.[59-68] B) Rank of 18 guide RNAs targeting the EMX1 gene after Compartmentalized CRISPR reactions (CCR) screen. The cleavage percentage is determined by the fraction of NGS reads that is cut at the respective on-target relative to the fraction that is uncut. The NGS reads represent the average of three repeated experiments. Note, Among the highest performing gRNAs is the (gRNA 16) which is well-characterized in literature [94, 95] and confirmed to have high efficacy. The Error bars are binomial confidence (95%) based on the number of next-generation sequencing reads for each gRNA/target DNA molecule.

Figure 25. *In* vitro Validation of the Top Three Screened gRNAs Using CCR

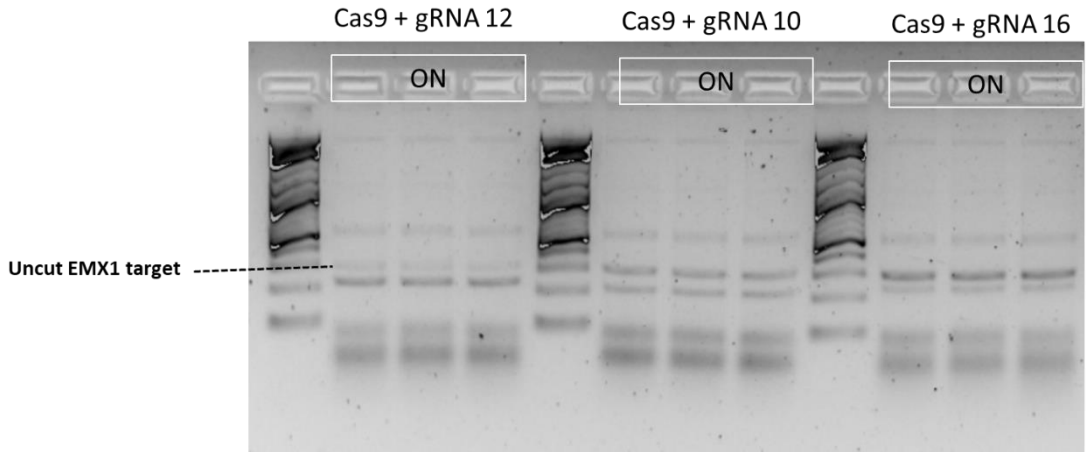

Note. *In vitro* validation (one at a time) of the top three gRNA candidates screened for on-target cleavage efficiency screened using Compartmentalized CRISPR reactions (CCR) approach. Note gRNA 12 has higher efficiency compared to gRNA 16 and gRNA 10. The uncut target derived from EMX1 gene (by PCR) is around 300 bp and the cleaved DNA post in vitro CRISPR assay is around 200 bp. The additional band around 500bp corresponds to PCR byproducts derived from the EMX1 gene.

Compartmentalized CRISPR Reactions (CCR) to Determine Multiple gRNAs Off-target Cleavage Efficiency

We next employed the compartmentalized CRISPR reactions (CCR) method to evaluate the cleavage efficiency of five different gRNAs targeting the EMX1 gene at its potential off-target sites [75] as shown in Table 2.

Table 2. Eighteen Predicated Off-target sites for Four of the gRNAs from CRISPOR [75] as Well as gRNA-16

#	targets/gRNAs	Off-targets
1	1	GCTTTGTGGCAATGCACAACTGG
2	1	GCTTCGTGTCAATTTGCCACGGG
3	2	GGGCCATGGGTTGATGTGATGAG
4	2	GTGCCACCAGTTGATCTGATGGG
5	3	GTGGCTCATTGCCAAGGAGCCGG
6	3	GTGTGGCATTGACACGAAGCTGA
7	3	ATGGCACATTGCCACTAAGCAGG
8	5	GCTCCCATCACATCACCCTGAGG
9	5	TCTCCCATCACATCCACCAGTGG
10	5	GCTGCCCTCACATCAACAGGTGG
11	5	GATCCCATCACATCCACAGGTGG
12	5	GCTTCCATCACAGCAGCCGGGGG
13	5	GCCCCCATCAGATCTACCGGAGG
14	5	GCTCCCCTCACATGAACCTGAGG
15	16	GAGTTAGAGCAGAAGAAGAAAGG
16	16	GAGTCTAAGCAGAAGAAGAAGAG
17	16	GAGTCCTAGCAGGAGAAGAAGAG
18	16	GAGGCCGAGCAGAAGAAAGACGG

We designed a DNA molecule similar to the design used in Figure 21, with the on-target site located distal to the gRNA expression region and the off-target located proximally (as depicted in Figure 26A). In this manner, following screening, the identity of the spacer and the resulting length of the DNA molecule can be determined. If the DNA molecule is only cleaved at the distal target, it indicates that the RNP with that particular gRNA is active and specific in relation to that off-target site, as the off-target site remains uncut. Conversely, if cleavage occurs at the proximal off-target, it suggests that the RNP with that gRNA is not sufficiently specific in relation to that off-target site.

Figure 26 B, illustrates the cleavage efficiency at the potential off-target sites for five different gRNAs, as determined by the fraction of NGS reads. To validate the accuracy of our NGS results obtained via the CCR technique, we then compared the observed off-target cleavage efficiency of one of the gRNAs 16 with that reported in the literature. [95] We found our result follows the similar trend with maximum cleavage at off targets OT1 and OT2 followed by OT3 and OT4 (Figure 26B-inset). Thus, this result demonstrates that CCR can be used as well to screen a large library of off-targets allowing for the simultaneous evaluation of guide RNA (gRNA) activity at both intended target sites and potential off-target sites, providing valuable insights into the specificity of CRISPR-Cas systems.

Figure 26. Simultaneous Evaluation of Off-target Cleavage Efficiency of Five Different gRNAs Targeting EMX1 Gene Using Compartmentalized CRISPR Reactions (CCR)

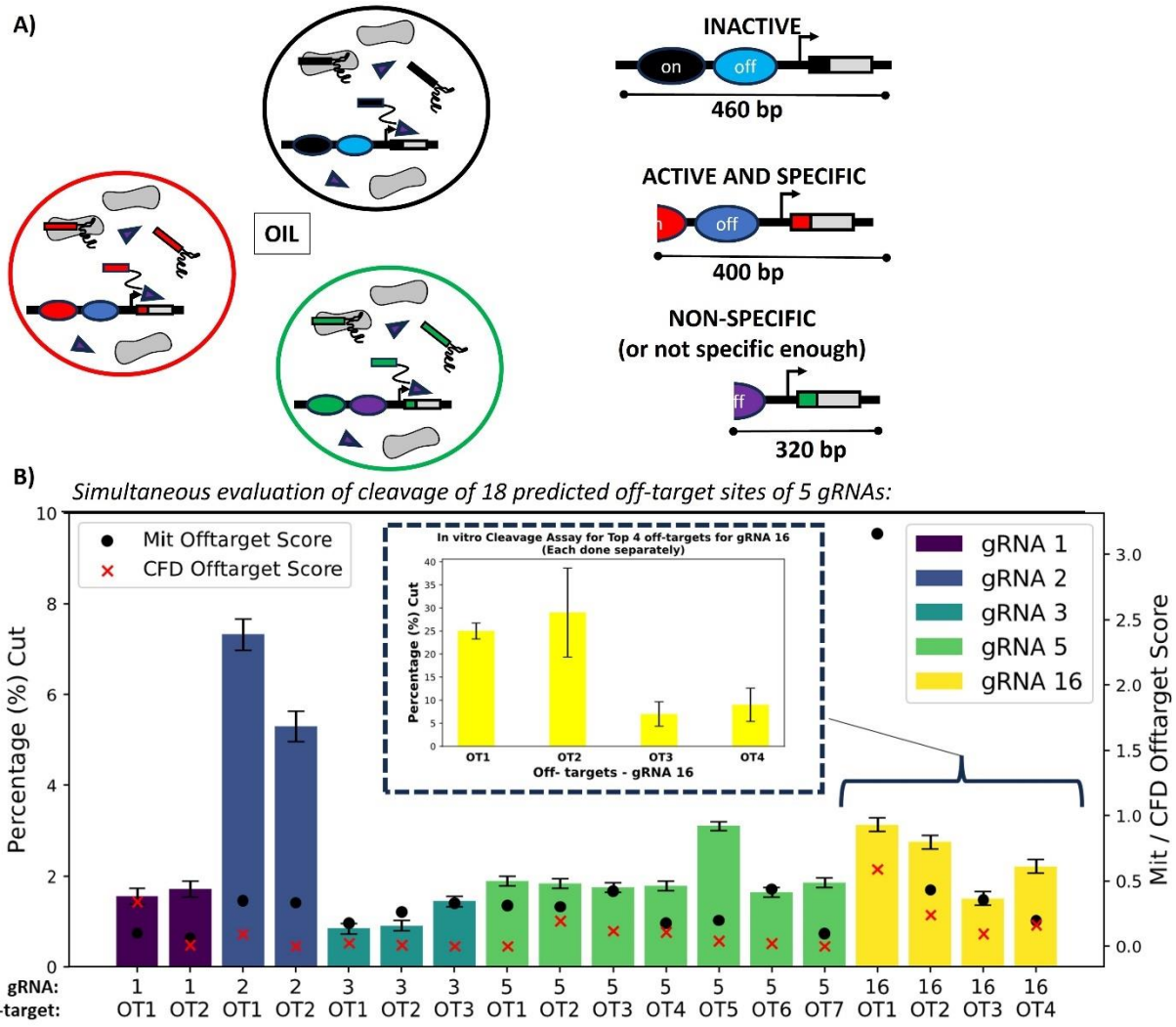

Note. A) Designed DNA molecule similar to the one used in Figure 20 B (iii), with the on-target site located distal to the gRNA expression region and the off-target located proximally. Resulting length of the DNA molecule can be used to determine the off-target cleavage efficiency for the gRNAs. If the DNA molecule is only cleaved at the distal target, it indicates that the RNP with that particular gRNA is active and specific in relation to that off-target site, as

the off-target site remains uncut. Whereas, if cleavage occurs at the proximal off-target, it suggests that the RNP with that gRNA is not sufficiently specific in relation to that off-target site B) Employing the compartmentalized CRISPR reactions (CCR) method to evaluate cleavage efficiency at the potential off-target sites for each gRNA set. The NGS reads represent the average of three repeated experiments. The cleavage percentage is determined by the fraction of NGS reads that is cut at the proximal off-target relative to the fraction that is uncut. The error bars are binomial confidence (95%) based on the number of next-generation sequencing reads for each gRNA/target DNA molecule. (inset) Off-target activity for gRNA 16 using CCR follows that pattern observed when activity at those sites is validated one-at-a-time using purified RNPs.[95]

Compartmentalized CRISPR reactions (CCR) for Screening of x-gRNAs

Next, we tested the utility of compartmentalized CRISPR reactions (CCR) approach to screen a large library of these extended guide RNAs (x-gRNAs). As previously reported,[94, 95] extended guide RNAs (x-gRNAs) are gRNAs with short (8-12) bp extensions to the 5'- end immediately next to their spacer sequence which potentially abolish the off-target activity while preserving on-target activity of the corresponding RNP (Figure 27A). However, identifying the optimal sequence for these 5'-nucleotide extensions poses a significant challenge, as many extensions either have no effect on specificity or also compromise on-target activity. To screen the x-gRNAs library, we constructed a DNA library encompassing all possible 5'- extensions of 8 nt's (65,536 possible sequences) for *EMX1* gRNA 16, from Figure 24 on a DNA molecule which had its target on the distal end and one each of the four most active off-target sites [94, 95] at the proximal site: a total of 262,144 separate gRNA/target/off-target combinations within a single CCR reaction (Figure 27). Through this approach, we could assess the efficiency and

specificity of x-gRNAs by analysing the resulting DNA molecule length: cleavage exclusively at the distal target indicated activity and specificity of the corresponding RNP, whereas cleavage at the proximal cut at the proximal off-target indicated that the RNP with that x-gRNA is not specific enough (Figure 27B).

Figure 27. Compartmentalized CRISPR Reactions (CCR) Designed for Screening of x-gRNAs

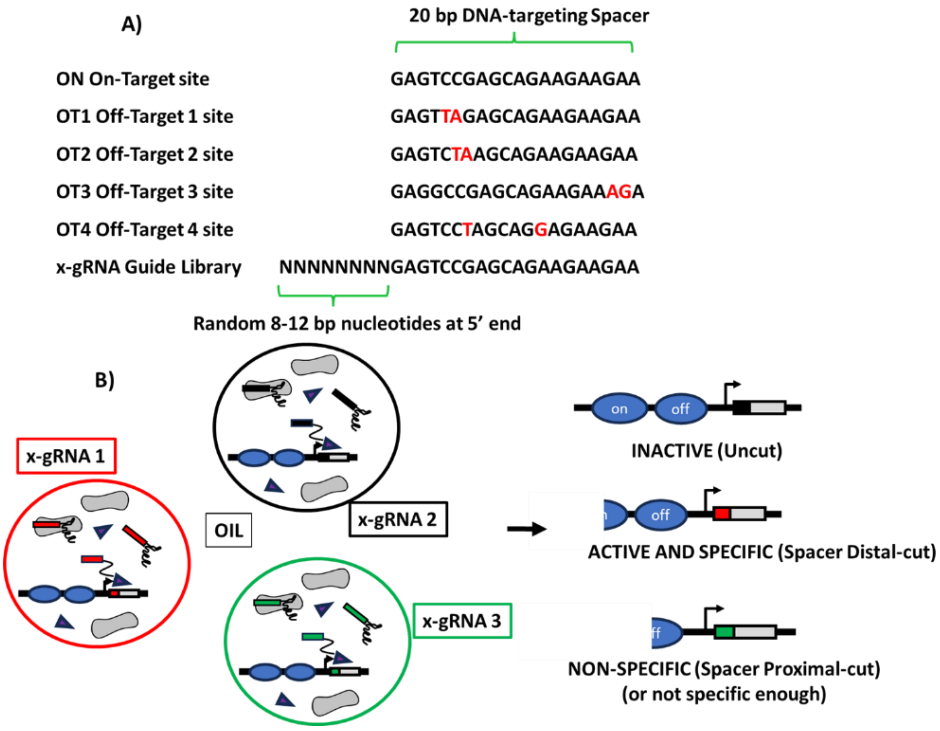

Note. A) Designed DNA library encompassing all possible 5'- extensions of 8 nt's (65,536 possible sequences) for EMX1 gRNA 16, from figure 24 on a DNA molecule which had its target on the distal end and one each of the four most active off-target sites at the proximal site B) Different x-gRNAs are expressed in different individual emulsions, and from the sizes of the recovered DNA fragments we can identify active and specific x-gRNAs via next-generation sequencing.

With a vast array of 262,144 individual gRNA/target/off-target combinations incorporated into the oligo, overcrowding of gRNAs in aqueous conditions resulted in minimal cleavage product formation. Conversely, in emulsion conditions, particularly with smaller water droplets, facilitated isolation of each template with its respective gRNAs within individual water droplets of the water-oil emulsion. This isolation alleviated crowding issues, leading to observed cleavage product formation (refer to Figure 28A).

Figure 28. CCR Results with the DNA library Designed for Screening of x-gRNAs

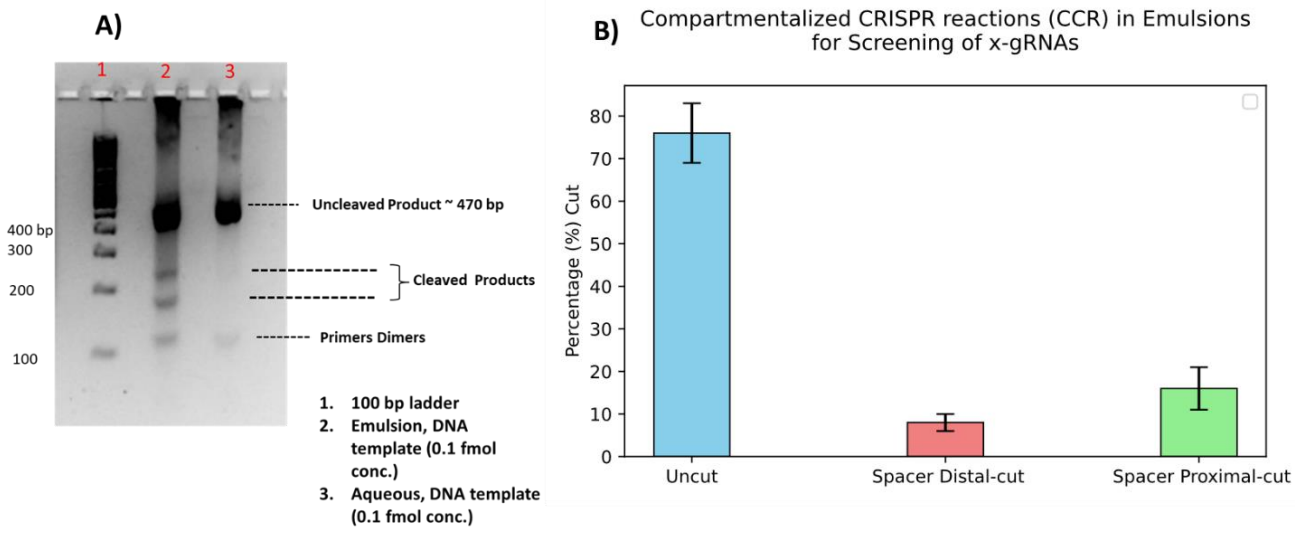

Note. A) Agarose gel image for *in vitro* reaction in either under standard reaction conditions (with no emulsions) and within the emulsions with the DNA library designed for screening of x-gRNAs. Lane details are as provided in the Figure. B) Analysis of the NGS result revealed that majority of the templates was uncut, while a smaller fraction, about 3590, efficient and specific extended gRNAs (x-gRNAs) are screened, which exhibited cleavage exclusively at the on-target sites and generating “Distal-Cut” DNA strands.

Figure 29. Determination of Top "Good" x-gRNAs from Next-Generation Sequencing (NGS)

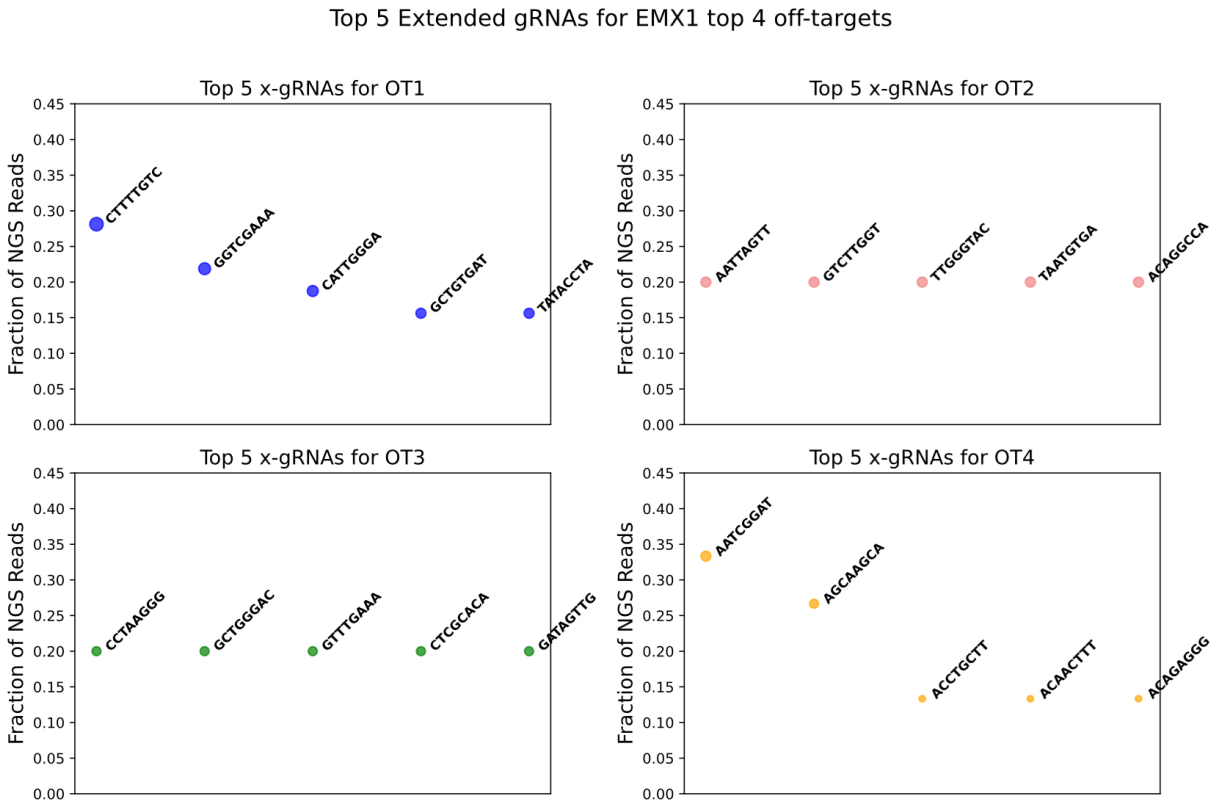

Subsequently, we conducted next-generation sequencing (NGS) of the reaction products under the emulsion condition. Examination of the NGS data revealed that bigger fraction of the templates was uncut, while a subset of 3590, efficient and specific extended gRNAs (x-gRNAs), exhibited cleavage exclusively at the on-target sites and generating "" DNA strands (Figure 28B).

In vitro Validation of the Top x-gRNA Candidates for EMX1 Off-targets

Figure 30. Top "Good" x-gRNAs for EMX1 Off-target 1(OT1) Screened Using CCR

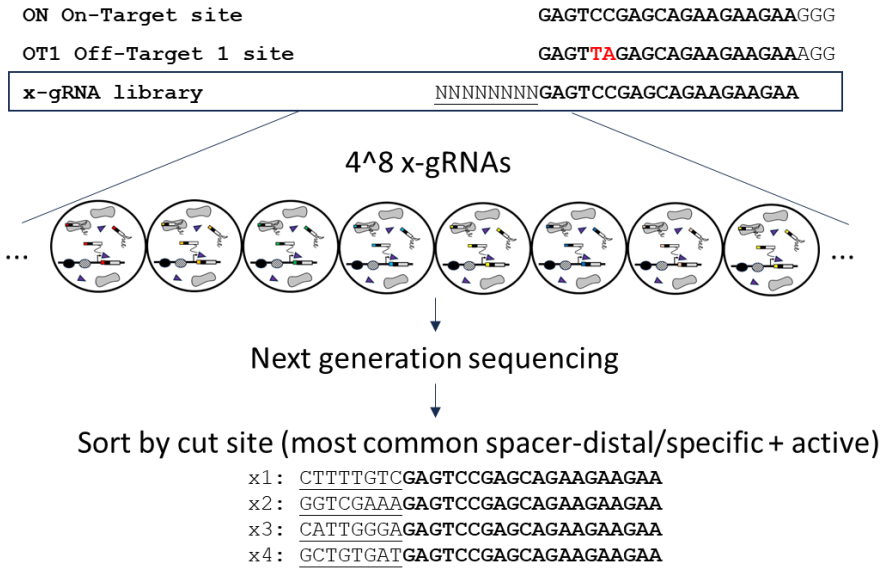

Note. With CCR, all 4^8 x-gRNA sequences are evaluated simultaneously.

We next identified the most common x-gRNA spacer sequences with spacer-distal cleavage patterns from the next-generation sequencing (NGS) data. Following this, we isolated the top five x-gRNAs with the highest fraction of NGS reads for each off-target, as depicted in Figure 29. To assess the concordance between our NGS-derived findings and experimental outcomes, we conducted *in vitro* validation of the top four x-gRNA candidates for one of the off-target site OT1 (Figure 30 and Figure 31). Remarkably, all four of the prioritized x-gRNAs demonstrated activity at the intended target site and exhibited no off-target cleavage activity *in vitro* (Figure 31). These findings shows that our developed compartmentalized CRISPR reactions (CCR) in emulsions can also be used for screening a big array of gRNAs with special attributes.

Figure 31. *In vitro* Validation of the Top "Good" x-gRNAs for EMX1 Off-target 1

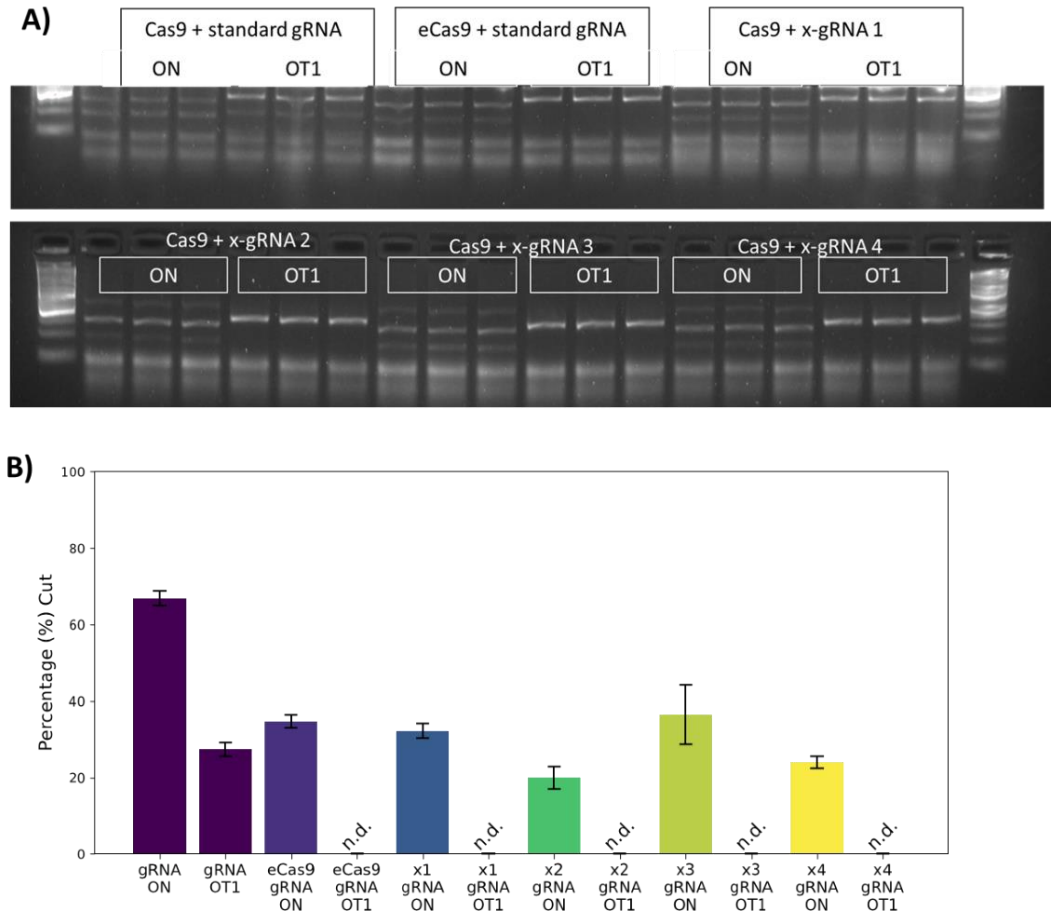

Note. A) In vitro validation (one at a time) of the top four extended guide RNA (x-gRNAs) candidates (in triplicate) for EMX1 off-target OT1. Representative agarose gel shows RNP cleavage activity for EMX1 sgRNA with both Cas9 and Engineered Cas9 (eCas9) as well as screened x-gRNAs with Cas9. The uncut target is around 300 bp both for targets and off-targets and the cleaved DNA is around 200 bp. B) Analysis of agarose gel revealed that the screened x-gRNAs are active on-target and exhibit no off-target in vitro cleavage activity.

Discussion

In summary, water-in-oil emulsions technique has found significant utility in handling vast array of unique DNA molecules concurrently, such as in library preparation for next-

generation sequencing (NGS) [84, 86] and in directed evolution studies.[87, 89, 91] Here, we have demonstrated the feasibility of conducting the entire CRISPR reaction process, including gRNA transcription, RNP formation, and target cleavage within these micro-emulsions to screen a large library of gRNAs/targets and off-targets in a streamlined and experimentally simplified manner. We've termed this method as 'compartmentalized CRISPR reactions (CCR). This CCR approach offers a robust yet straightforward method for efficiently screening numerous gRNA candidates, provided from various computational tools for gRNA design, for both activity and specificity. In addition, we have illustrated the utility of CCR approach for high-throughput screening of efficient extended gRNAs (x-gRNAs) which eliminates the off-target activity of the associated gRNAs while still maintaining its on-target activity. The CCR technique thus serves as a streamlined method for identifying highly active and specific gRNA variants from extensive sets of gRNA/target/off-target combinations, thereby providing an alternative strategy to address challenges associated with currently established high-throughput screening techniques.

Materials and Methods

DNA Oligonucleotides

DNA sequences for all oligonucleotides are listed in Supplementary Note S1-S5 provided in Appendix A.

Protocol for Single-Pot *in vitro* CRISPR Cleavage Assays

DNA oligonucleotides were purchased were purchased from Integrated DNA Technologies (IDT) and then resuspended to a stock concentration of 100 μM. DNA oligonucleotides were further diluted to a concentration of 300 fmol which is visible in agrarose gel stained with SYBR Safe dye. All the reagents were then mixed in the following order to set up CRISPR-mediated cleavage reaction: 7 μL nuclease-free water, 1 μL DNA Oligonucleotides

(300 fmol), 2 µL NEB r 3.1 Buffer (10X), 1 µL RNAse Inhibitor (New England Biolabs #M0314S), 0.4 µL (2.5 mM) ribonucleotide triphosphate mix (NEB: N0466S), 3 µL (1000nM) Cas9 nuclease, *S. pyogenes* ((NEB; M0386T) , 2 µL T7 RNA polymerase (New England BioLabs). The reaction mixture is then incubated for a duration of 3 hours at 37°C. This is followed by proteinase K digestion, where 1 µL of proteinase K (ThermoFisher kit #EO0491) is added, and the mixture is incubated at 56°C for 10 minutes. Subsequently, 2 µL of RNAseA is added to degrade the sgRNA molecules. The resulting products are then separated on a 3% agarose gel, stained with SYBR Safe, and analyzed using ImageJ.

Protocol for Single-Pot CRISPR Cleavage Assays in Emulsions

Water-oil emulsions were generated using the bulk mixing of water and oil phase following the procedure outlined by Williams et al. [84] The oil phase was prepared by thoroughly mixing the following components, 2.25 ml -Span 80 4.5% (vol/vol), 200 µl -Tween 80 0.4% (vol/vol), 25 µl- Triton X-100 0.05% (vol/vol) and Mineral oil to 50 ml. A modification in the protocol was introduced for the aqueous phase, which comprised the following reagents for the CRISPR-induced cleavage reaction: 216.6 µL nuclease-free water, 1 µL DNA oligonucleotides (1 fmol/0.1 fmol), 26 µL NEB r 3.1 Buffer (10X), 5 µL RNAse Inhibitor (New England Biolabs #M0314S), 5.2 µL (2.5 mM) ribonucleotide triphosphate mix (NEB: N0466S), 1µL (1000nM) Cas9 nuclease, S. pyogenes (NEB; M0386T), 5.2 µL T7 RNA polymerase (New England BioLabs).

In a cryovial with a magnetic stir bar on a magnetic plate at an intermediate setting (1150 rpm), 400 µL of the oil phase was placed. Subsequently, 200 µL of the aqueous reaction mixture was slowly added to the oil phase over a 5-minute duration. It is important to note that the entire setup was maintained in a cold room at 4°C during the emulsification process. After this step, a

stable water-oil emulsion was formed, followed by an 8-hour incubation at 37°C. The emulsion was then disrupted by centrifugation (15,000 rpm, 10 min) to recover the water phase, while the oil phase was pipetted out. Next, 1 μL of proteinase K (ThermoFisher kit #EO0491) is added to degrade the RNP, and the mixture is incubated at 56°C for 10 minutes. Following this, 2 μL of RNAse A is added to degrade the sgRNA molecules. The DNA library from the aqueous phase was extracted through a cleanup process with magnetic beads added in a 0.9X ratio to the aqueous phase. The purified DNA library was subsequently enriched using the NEBNext® Ultra™ II DNA Library Prep Kit for Illumina® (NEB# E7645S), followed by PCR with NEBNext® Multiplex Oligos for Illumina® (NEB# E7730S). The resulting products were separated on a 3% agarose gel, stained with SYBR Safe, and then submitted for NGS sequencing.

***In vitro* Digestion Reactions**

DNA targets containing the target sequences were synthesized by Twist Bioscience. Subsequently, they were PCR amplified using the provided universal primers, purified, and resuspended in nuclease-free water to to a concentration of 100 nM. For each reaction, three technical replicates were prepared in the following order: 7 μL of nuclease-free water, 1 μL of the target DNA substrate (100 nM), 1 μL of 10x Cas9 Nuclease Reaction buffer (composed of 200 mM HEPES, 1 M NaCl, 50 mM MgCl2, and 1 mM EDTA with a pH of 6.5 at 25°C), and 1 μL of Cas9-RNP (1 mM). The assembled reactions were then incubated for 1 hour at 37°C, followed by digestion with proteinase K (ThermoFisher enzyme #EO0491) (1 μL) at 56°C for 10 minutes. The resulting products were resolved on a 3% agarose gel stained with SYBR Gold and analyzed using ImageJ. For analysis of the gel image in Image J, the fluorescence intensity was

normalized by length of the DNA fragments, and fraction cleaved was calculated using the equation:

$$Fraction\ cleaved(\%) = \left(\frac{Normalised\ cleaved\ band\ intensity}{\sum Normalised\ Cleaved\ and\ Uncleaved\ band\ Intensities}\right) \times 100$$

Dynamic Light Scattering (DLS) Measurement

The size of water droplets in water-oil emulsions were measured using a dynamic light scattering (DLS) instrument, Zetasizer Nano ZS90 (Malvern instruments, Malvern, UK). The average value of 3 run was taken as a final result. The stability of the water-oil emulsion was tested by measuring the water droplets immediately after emulsion formation and after interval of 8 hours.

Analysis of the Next-generation Sequencing (NGS) Data

The Next-generation sequencing (NGS) data had sequences with pre-trimmed adaptors and barcode sequences. The paired end was then merged into longer, single reads using FLASH (Fast Length Adjustment of SHort reads) [96] bioinformatic tool. A script was written in python that used Bio-python [97] package for reading the FASTQ files. Each dataset here is combination of three identical repeat experiments. The algorithm begins by checking the sequence length of each read from the input data to ensure it meets a certain criterion. Next, the sequences that pass the length check undergo alignment using the Smith-Waterman algorithm with reference sequences, which include a complete list of different targets and off-targets present in the DNA library. Once the alignment scores are obtained, the algorithm evaluates the alignment score threshold and selects sequences that exceed the threshold. This step ensures that only sequences with high alignment scores, indicating a good match, are considered for further analysis.

Following this, based on their alignment scores the sequences are assigned to categories (Spacer-Distal /Spacer-Proximal/ Uncut Pattern) with respect to different targets or off-targets present. The algorithm then checks the occurrence of sequences in each category by counting how many times each sequence appears within its assigned category. To calculate the percentage cut, the ratio of the number of sequences in the cut state (spacer-proximal or distant) to the number of uncut sequences in each category is taken. Finally, the algorithm selects the top hits, which are the sequences with the highest percentage cut or most frequent occurrences. For the analysis of results from extended guideRNAs (x-gRNAs) screening experiment, a Python script was written to extract 8-nucleotide sequences (extended gRNA extensions) adjacent to the (T7 Promoter + off-target) sequence from the filtered large fragments list and stored them as a CSV file.

The reference code used for the analysis of the NGS data is provided in https://github.com/neelarka/CCR-Analysis

CHAPTER III: PROGRAMMED INTERNAL RECONFIGURATIONS IN A 3D-PRINTED MECHANICAL METAMATERIAL ENABLE FLUIDIC CONTROL FOR A VERTICALLY STACKED VALVE ARRAY

Abstract

Microfluidic valves play a key role within microfluidic systems by regulating fluid flow through distinct microchannels, enabling many advanced applications in medical diagnostics, lab-on-chips, and laboratory automation. While microfluidic systems are often limited to planar structures, 3D printing enables new capabilities to generate complex designs for fluidic circuits with higher densities and integrated components. However, the control of fluids within 3D structures presents several difficulties, making it challenging to scale effectively and many fluidic devices are still often restricted to quasi planar structures. Incorporating mechanical metamaterials that exhibit spatially adjustable mechanical properties into microfluidic systems provides an opportunity to address these challenges. Here, systematic computational and experimental characterization of a modified re-entrant honeycomb structure are performed to generate a modular metamaterial for an active device that allows us to directly regulate flow through integrated, multiplexed fluidic channels “one-at-a-time,” in a manner that is highly scalable. A design algorithm is presented, so that this architecture can be extended to arbitrary geometries, and it is expected that by incorporation of mechanical metamaterial designs into 3D printed fluidic systems, which themselves are readily expandable to any complex geometries, will enable new biotechnological and biomedical applications of 3D printed devices.

Introduction

Microfluidic valves play a key role as integrated elements within microfluidic circuits, [99, 100] regulating fluid flow in microchannels and enabling a diverse array of applications across fields such as analytical chemistry, [101, 102] biotechnology, [103, 104, 105] and medical diagnostics. [105, 106] Many of these sectors, especially in drug discovery [107, 108] and high-throughput molecular cell biology, [109, 110] benefit significantly when equipped with valving systems that can be effortlessly expanded to accommodate a vast array of multiplexed fluidic inputs and outputs. [111, 112] To achieve this type of scalable control across a considerable number of fluidic valves, a common approach relies on an architecture [113, 114] whereby one valve can be designed to shut off flow across multiple channels simultaneously (Figure 32A, C). In a design pioneered by Quake et al. [115, 116] the channels carrying the fluid of interest (the "flow" channels) are arranged in parallel beneath pneumatically actuated "control" channels. These control channels are designed to close specific flow channels at regions of overlap ("closeable" segments) when pressure is increased. Simultaneously, other flow channels remain open regardless of the pressure in the control channel at the regions of overlap ("always open" segments). This configuration can be designed so that only a single flow channel is open when any combination of half of the control channels is pressurized (Figure 32C). Consequently, it enables the addressing of $N! /(N/2)!^2$ individual flow channels using only N control channels. For instance, with six control channels, it can regulate twenty flow channels, so only one is open at a time; with eight control channels, it can regulate seventy individually addressable flow channels; and with ten control channels, it can regulate 252 individually addressable flow channels, and so forth, scaling factorially.

Figure 32. A 3D-printed, Vertically Stacked Valve Array for Fluidic Control

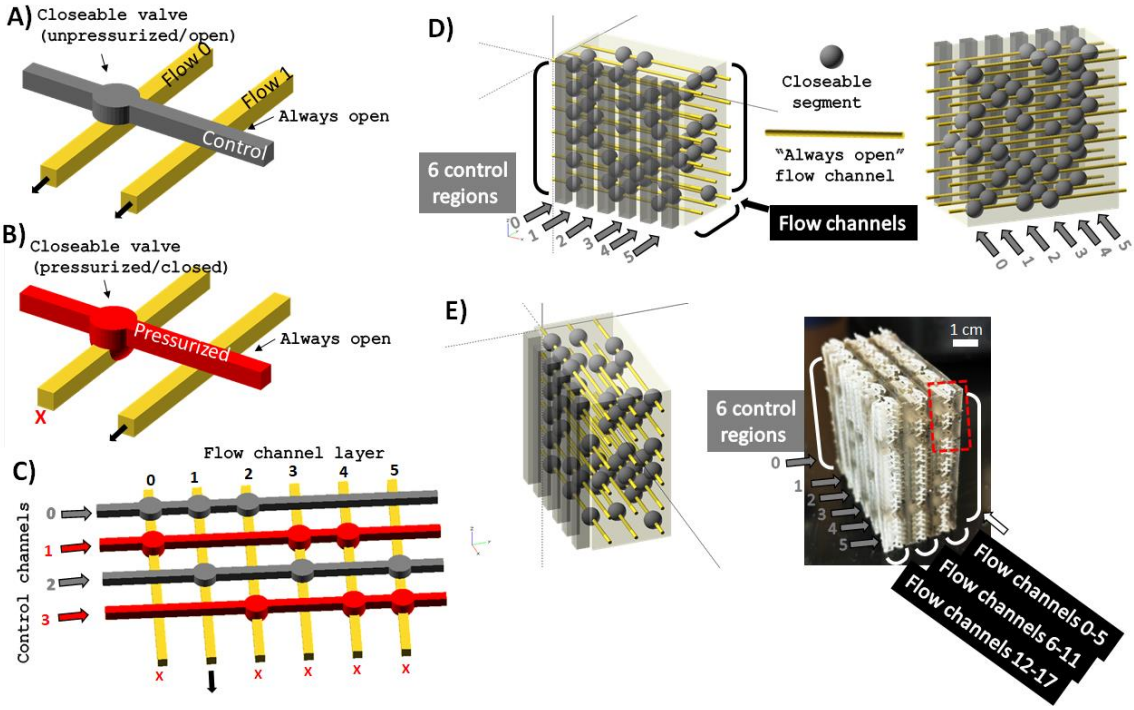

Note. A+B) In traditional, quasi-planar fluidic valves arrays (with "Quake-style" valves), pneumatic "control" channels are placed above a series of "flow" channels. When specific control channels are pressurized (red), "closeable" segments of the flow channels that lie underneath the pressurized control channels collapse to obstruct flow, while other flow channels ("always open") underneath the same control channel can remain unobstructed regardless of its state (pressurized/unpressured. C) This architecture allows for N control channels to regulate $N!/(N/2)!^2$ for any combination of N/2 pressurized control channels. Here, closeable valves are arranged so that pressurizing any 2 of 4 control channels allows flow through only 1 of 6 flow channels by blocking flow through the other 5. D) Schematic (and reverse, right) of a stacked valve array in 3 dimensions, where collapsible regions of flow channels are positioned so that applying pressure to any 3 of 6 "control regions" allows flow through only 1 of 18 flow channels

in the device. Vertical bars highlight the planes of the "control regions" in the device. E) Schematic and 3D printed valve array manifold, engineered using a mechanical metamaterial design to control the propagation of forces within its structure for the controllable collapse of integrated flow channels.

Fabricating these microfluidic systems typically requires a complex, multilayer process to properly arrange and register control channels atop the flow channels, separated by a thin membrane; [111, 113, 115, 116, 117, 118] however, advances in additive manufacturing with 3D printing have opened new opportunities to make these devices outside of a clean room facility. 3D printing has enabled the rapid fabrication and prototyping of miniaturized, intricately designed components which can control the flow of fluids at the microscale level, [119-132] and allows for the creation of monolithic, integrated microfluidic devices without any leakage issues. [121, 124,125] Digital light processing (DLP) 3D printing, [132, 133] which builds objects layer by layer using a planar light source, is highly versatile for scaling as it allows simultaneous printing of large number of valves and channels. Even "Quake-style" valves have been generated using DLP 3D printing, [124] albeit using a custom-made high-resolution 3D printer and specialized 3D printing resins.

Despite these advances, most 3D printed microfluidic systems remain essentially quasi-planar structures, [135] meaning they do not fully take advantage of the scaling capabilities offered by 3D printing. This limitation can likely be attributed to the complexity associated with regulating pressure propagation in three dimensions to control valve actuation within the device. [113] As a result, these quasi-planar devices are limited in their ability to achieve higher throughput, as the channel dimensions of these 3D printed valves are restricted by the resolution of commercially available 3D printers. Here we have aimed to design a 3D-printed valve array

system that are stacked in three dimensions and that can be easily expanded to control large numbers of flow channels, like “Quake-style” valving” system, [115, 116, 136] using a tilted re-entrant honeycomb mechanical metamaterial [137-140] structure (Figure 32C,D).[140, 141, 142] After systematic experimental and computational characterization of the mechanical structures, we have found that through the adjustment of a single characteristic of its re-entrant cells, its “tilt” angle θ (Figure 33A, C), we can generate metamaterial structures with specific regions that either remain stable or collapse under applied forces. This capability allows us to generate 3D structures with engineered “always open” and “closeable” valve regions (Figure 32C) that can be stacked to build arrays of “Quake”-like valves within a 3D printed framework. We also present an algorithm to design and print these “stacked” fluidic arrays with arbitrary geometries, and to illustrate this, we present a fluidic array of 6 × 3 (18 total) flow channels that are individually controllable through the application of forces on any three out of six “control” regions on the structure (Figure 32D), and demonstrate how these devices can be expanded even further (e.g., to 96 flow channels regulated by nine control regions). While re-entrant honeycomb and auxetic structures are often used as “passive” materials with robust stretching and tunable deformation characteristics, we expect that the integration of active and dynamic mechanical metamaterials with microfluidic devices that is enabled by advances in 3D printing will allow for new applications in lab-on chips and biotechnology.

Figure 33. The "Tilt" Angle in a Re-entrant Mechanical Metamaterial Provides a Handle to Tune Relative Mechanical Stiffness Within a 3D printed Device

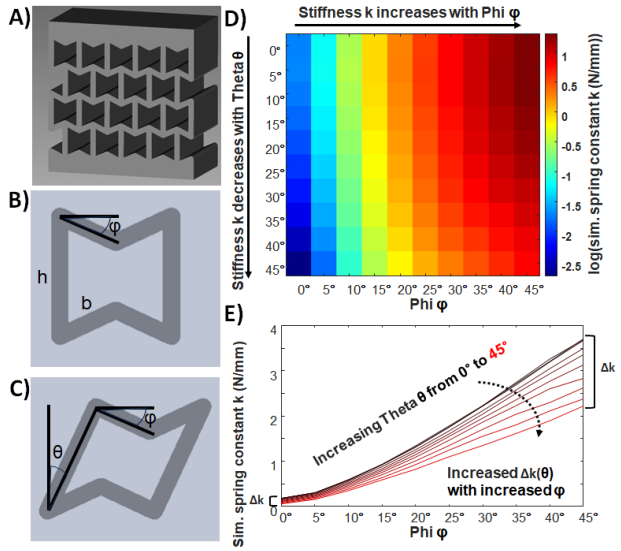

Note. A) The structure of a re-entrant mechanical metamaterial, with a "bowtie" structure offset by half the cell width in each layer. B) The basic unit of a re-entrant honeycomb structure, defined by the re-entrant angle phi φ which defines its key mechanical property of a negative Poisson ratio (NPR). h is the length of the side wall and b is the length of the re-entrant arm. C) We hypothesized that tilting the unit cells with tilt angle theta θ allows successive layers with the same φ to stack and maintain registry while providing an additional handle on the mechanical stiffness of the layer. D) According to finite element analysis (FEA) of re-entrant unit cells subjected to forces, the estimated (simulated) stiffness increases with increased φ but decreases with the same φ with increased θ (larger tilt). E) Increasing φ allows for greater differences in stiffness between layers with different tilts, a prerequisite for engineering "always open" and "closeable" segments of a fluidic device.

Results

Design and Optimization of 3D-Printed Mechanical Metamaterials with Programmable Internal Deformations

In expanding a "Quake-style" valve array into the third dimension, we require the ability to generate "closeable" segments and "always open" segments of flow channels through the device to which a pressure can be applied in parallel across the entire device (Figure 32D). This required the design of a material with controllable force propagation throughout the device so that all valves within a "control" region could be addressed simultaneously through the 3D structure. Initial designs focused using auxetic re-entrant metamaterials (Figures 33A,B), which are mechanical metamaterials with a repeated cellular structure in the shape of overlapping bowties, as they are commonly used in applications where robust controllable deformation is required.[141, 142] Auxetic metamaterials have the unusual property of negative Poisson ratios determined by their "reentrant angle" φ.

Finite element analysis (FEA) predicted that the stiffness of the materials with re-entrant cells would increase with increasing φ (Figures 33D-E). This finding was consistent with initial experiments to test force versus displacement using 3D printed 5x5 grids (Figure 34A,B; Figure S1, Supporting Information; which are 4 four layers of 5 five re-entrant cells capped by two half-layers of solid, "filled-in" auxetic cells).We hypothesized that by changing the tilt (θ) of the reentrant structure (Figure 33C), we could modulate the mechanical properties of the metamaterial in such a way that the re-entrant bowtie structures, regardless of their stiffness, would still maintain registry across layers by virtue of their identical φ angles (i.*e.*, Figure 34C). The results of FEA of individual tilted re-entrant cells predicted that increasing θ would result in more pliant structures (lower simulated spring constants *k*), as expected. Further, it revealed that

with increased φ, the differences in spring constants (*Δk*) between re-entrant cells having different θ also increased (Figures 33D, E). Building on this principle, FEA revealed that sandwiching 2 tilted layers between un-tilted layers (θ = 0°) would result in greater deflections for the same force (Figure 34C). Further, compared to un-tilted structures--where initial stresses were evenly spread through the structure, and where, regardless of φ, all layers collapse simultaneously (Figure 34B and; Figure S1, Supporting Information) --the stresses would be directed through the tilted layers upon the initial application of force (Figure 34C). Defining regions of preferential compliance or rigidity in three dimensions forms the basis of how we will generate "closeable" or "always open" segments for integrated flow channels.

Figure 34. Tilting Re-entrant Mechanical Metamaterials Focuses Mechanical Stresses Within the Structures

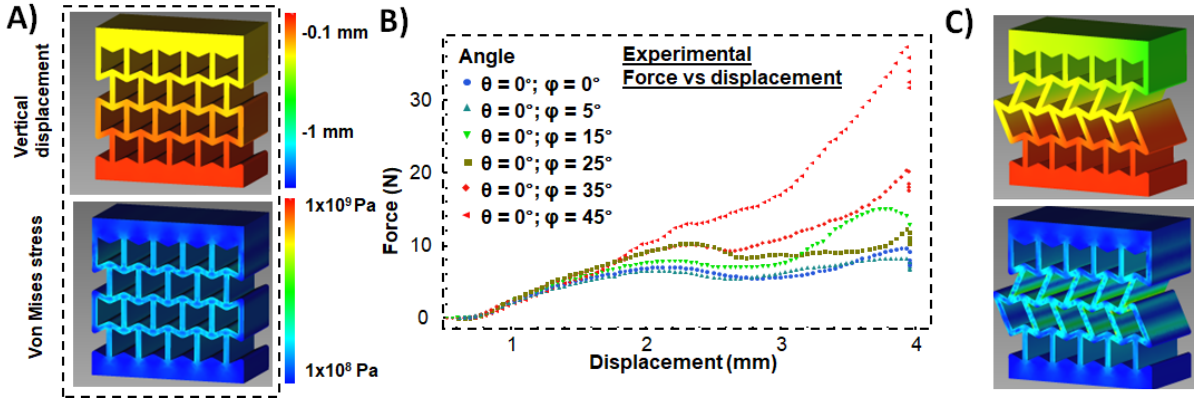

Note. A) FEA of 5x5 un-tilted (θ = 0°, φ = 25°) re-entrant honeycomb grids reveals that stresses are distributed evenly throughout. B) Experimental force vs. displacement curves of un-tilted 5x5 re-entrant honeycomb grids (as in 34A, dotted box) with different φ reveals that all layers deform simultaneously upon compression (see Figure S1, Supporting Information) and that these structures are significantly stiffer than those with tilted interior layers (see Figure

35C). FEA reveals that introducing tilted re-entrant cells (θ = 25°, φ = 25°) between un- tilted (θ = 0°, φ = 25°) layers focus the stress to the tilted layers initially and results in greater initial deflections for the same force. Coloration is the same as in 34A.

To maximize the difference in mechanical responses between un-tilted (Figure 35A) and tilted (Figure 35B) layers, we made two adjustments: 1) we "hollowed" the tilted re-entrant cells, giving them a wire-frame structure in three dimensions, further increasing their compliance, while un-tilted cells had solid walls, and 2) we systemically varied θ (for tilted cells) and φ (for both tilted and un-tilted cells, to maintain registration) to optimize these "banded" structures for use as "closeable" or "always open" segments in a 3D printed valve array (Figure 35C, Figures S2, and S3, Supporting Information). The 5x5 "banded" structures are built with (Figures 34C and 35D):

i. Half of one a layer of a solid, filled-in untitled re-entrant cells on the top and half of a layer of solid, filled-in untitled re-entrant cells on the bottom of the structure;
ii. a layer of untitled, solid-walled untitled re-entrant cells with empty interiors;
iii. one layer of tilted, wire-framed re-entrant cells;
iv. one layer of wire-framed re-entrant cells tilted at the same angle in the opposite direction;
v. one layer of untitled solid walled re-entrant cells with empty interiors.

Note that as part of our design criteria, we want each 5x5 grid to remain the same width (W) and length (L) (here, 9 mm x 9 mm) regardless of θ (for tilted cells) and φ. To do so, the side length of the bowties (h in Figure 33b) and re-entrant arm length (b) were adjusted for each set of conditions so that $b = W / (8 \times \cos(\varphi))$ and $h = (L + 5 \times b \times \sin(\varphi)) / (3+2 \times \cos(\theta))$, allowing the footprint of each 5x5 structure remains the same overall.

Figure 35. Banded (Tilted) and Hollowed Re-entrant Mechanical Metamaterials Allow for Controllable Collapse of the Specific Regions in the 3D Printed Structures

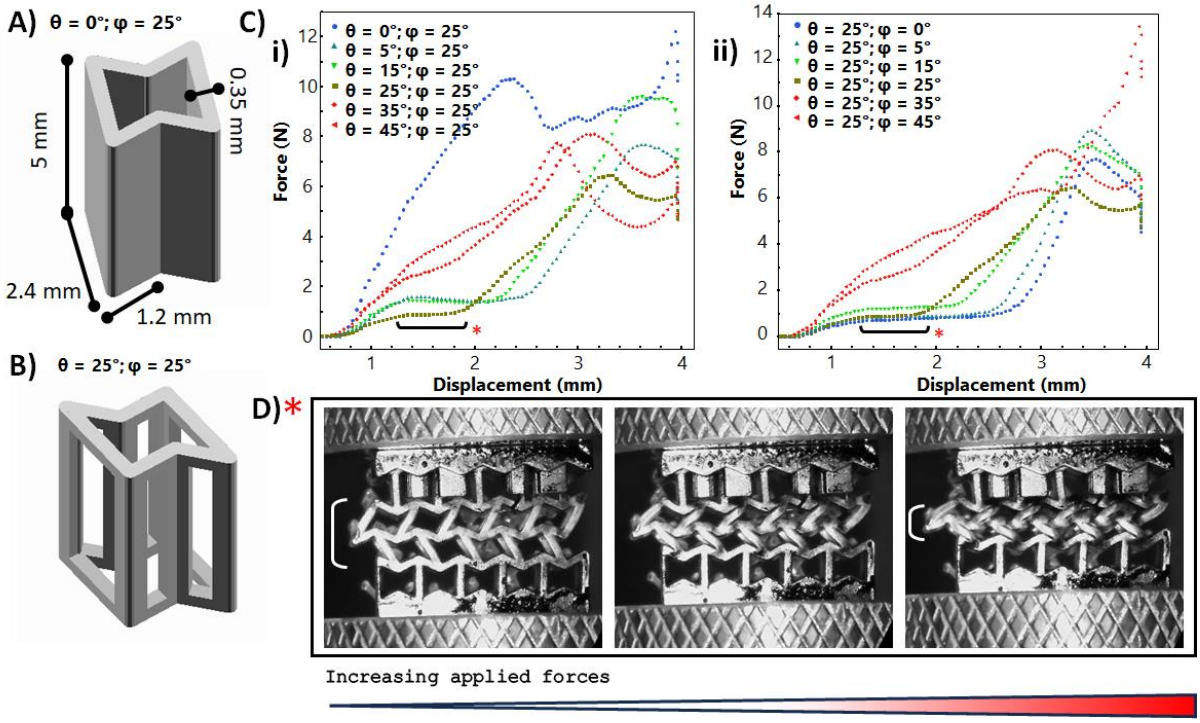

Note. A) 3D ('extruded') structure of the un-tilted re-entrant layers. B) Tilted layers are given 'wireframe' structures to further enhance their compliance compared to the un-tilted layers. C) Experimental force versus displacement curves for banded re-entrant 5x5 grids auxetic with un-tilted outer layers and tilted interior layers (see Figure 34C, for example), for increasing tilt angle theta θ for a given re-entrant angle phi φ (i) or increasing φ for a given θ. D) The interior layers (θ = 25°, φ = 25°) of banded tilted re-entrant mechanical metamaterials completely collapse before the outer layers (θ = 0°, φ = 25°) buckle, while maintaining spatial registration in the material.

We found the inner, tilted layers collapsed more readily as θ increased from 0° to 30°, after which the structures became more rigid and the inner and outer layers collapsed together

(Figure 35Ci; Figure S2, Supporting Information). Structures with θ = 25° have a minimum in the force required to collapse the interior layer, as those with higher θ tend to jam quickly; structures with lower φ require more displacement for the middle layers to completely collapse, while those with higher φ are significantly stiffer and cause the outer walls to buckle during their collapse. Conversely, for fixed θ values, the re-entrant structures exhibit the highest compressibility at the lowest φ value (zero degrees) and become less compressible as the value of φ increases (Figure 35Cii; Figure S3, Supporting Information).

"Closeable" and "Always Open" Segments for Mechanical Control of Fluid Flow

Structures with tilted layers having θ = 25°, φ = 25° (brown squares in Figure 35C) provide a 'sweet spot', with a short, low-force plateau during which the interior collapses first before the outer layers begin to deform (Figure 35D). Additionally, when assembled into larger arrays, structures with higher θ values (>25°) tend to buckle irregularly when subjected to applied forces (Figure S4, Supporting Information). Therefore, re-entrant grids with bands of tilted layers having θ = 25°, φ = 25° formed the basis of the "closeable" and "always open" segments of integrated flow cells (Figure 36A). These structures were extremely robust, spontaneously and recovering quickly after applied forces were removed, and exhibiting consistent mechanical characteristics without failure over the course of 1,000 deformations recorded using a force gauge (Figure S5, Supporting Information).

To engineer closeable segments, we positioned solid segments around integrated flow channels within the re-entrant grids, such that applied forces would call the interior region to collapse and seal the flow channel at that segment. The "always open" segments also collapsed, but redirected forces around the flow channel so it would remain open. In this way, if we apply mechanical pressures across stacked arrays of flow channels in parallel (at a "control region",

Figure 32D), depending on the structure around the flow channel it will either collapse or remain open (Figure 36B). When pressure was applied simultaneously across both segments, the flow channels in the closeable segments collapsed and flow of liquids through that channel ceased, while flow through the always-open segments was unaffected (Figure 36C). Multiple “closeable” and “always open” segments could be operated in parallel and independently when pressure is applied across a common control segment (Figure 37A). As an initial demonstration of controlled valving, we then constructed a 3D printed quasi-planar “Quake-style” manifold (as in Figure 32C) using the mechanical metamaterial segments with four control regions governing six channels, where pressure on any two control regions only allowed flow in a single region (Figures 36 and 37; Figure S6, Supporting Information). This manifold could be integrated to control inputs into a microfluidic chip or into fluidic multiplexors / de-multiplexors (Figure 37B, D; Figure S6, Supporting Information). Having developed “always open” and “closeable” segments of flow channels, these features allow for the controlled propagation of mechanical forces through a device and can be stacked to create a 3D, multi-layer valve array (Figure 38).

Figure 36. Tilted Re-entrant Mechanical Metamaterials Allow for the Generation of "Always Open" and "Closeable" Segments / Valves When Subjected to Applied Pressures in Parallel

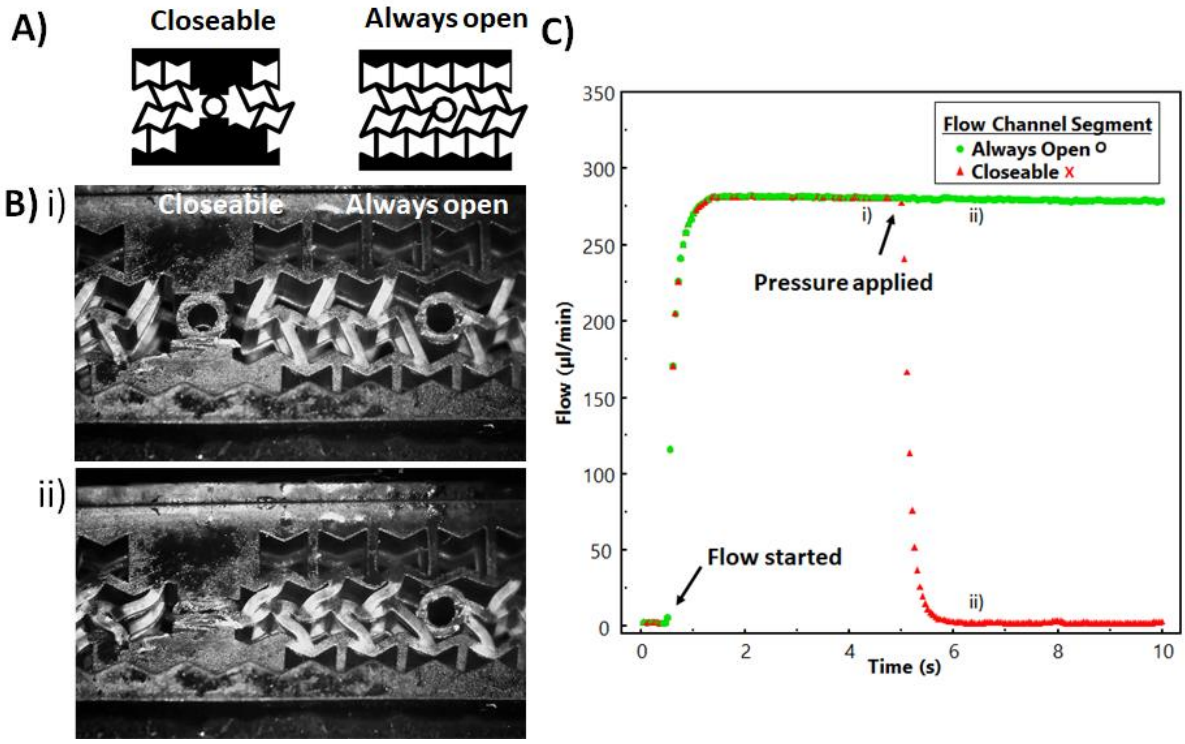

Note. A) 2D-projection of the design of "closeable" and "always open" flow channel segments. The flow channel is made from the circular segment in the middle of each design. Note that the un-tilted and (hollowed/wire-framed) tilted re-entrant cells have a 3D structure as shown in Figures 35A-B. B) (above) Before pressure is applied, both fluidic channels are open. (below) After pressure is applied to a "control region" above both segments, only the closeable channel collapses. C) Flow through two integrated channels (i) is high until both are simultaneously subjected to pressure applied across a "closeable" (red) and "always open" (green) segments until flow is obstructed in the flow channel with the closeable segment while flow in the channel with the always-open segment remains unchanged (ii).

Figure 37. A "Quasi-Planar" Valve Array Integrates into Microfluidic Multiplexors / De-Multiplexors

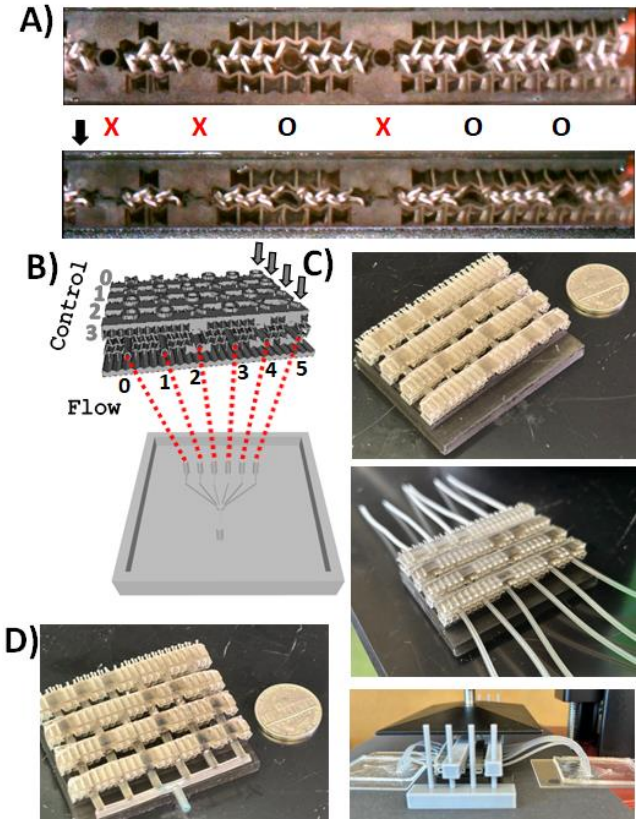

Note. A) An arrangement of six integrated flow channels, three of which have always open ('O') segments at the control region and three have closeable ('X') segments at the control region. When subjected to pressure across the entire control region, (below) only the flow channels with closeable segments collapse and are completely obstructed. B) Design of a 3D printed (quasi-planar) six flow channel / four control region metamaterial manifold (with architecture similar as in Figures 32C) for integration with a microfluidic multiplexor. C-D) Practical integration of the 3D printed quasi-planar valve array into microfluidic multiplexor / de-multiplexor architectures. See Figure S6 (Supporting Information).

Figure 38. A Stacked Valve Array with Complex Positioning of "Always Open" and "Closeable" Segments of Flow Channels

Note. A) A 3D printed stacked valve array (as in Figure 39E) has "always open" and "closeable" segments of 18 integrated flow channels distributed throughout, with some atop or between other kinds. (right) schematic projection of a multi-layer "control region". Note that the "always open" and "closeable" segments (from Figure 36A) of the flow channel are modular and fit together. B) Upon application of pressure to a control region (from the top) the closeable segments all collapse throughout the device, regardless of its position or location relative to "always open" valves, which remain unobstructed. (right) State of the integrated channels after application of pressure.

Algorithmic Design and 3D printing of Vertically Stacked Valve Arrays

To design a multi-layer valve array of arbitrary geometry, the number of control regions N for X number of flow channels must satisfy $N!/(N/2)!^2 \geq X$, which we demonstrate here with a 18, individually-addressable (only one is open at a time) flow channel device operated by six control regions ($3 \times 6 \times 6$, Figure 39). For a set of flow channels, it is useful to design a scheme

where the locations of “always open” and “closeable" can be algorithmically positioned at their precise control regions to allow individual addressability, and, if we wish specifically to open a specific control channel, to be able to readily calculate the control regions upon which pressure should be applied. To do so, we enumerate all combinations of *N* control channels (indexed from *0* to *N - 1*) of length *N/2* as [n_1, n_2,…n_k] (Figure 39A) for $k = N/2$ using the nested loop:[143, 144]

for $n_1 = 0$ to $N - k$

for $n_2 = (n_1 + 1)$ to $N - (k - 1)$

...

for $n_k = (n_{k-1} + 1)$ to $N-1$

print [n_1, n_2,…n_k]

that are each associated with a given flow channel with index $i = 0, 1, \ldots, X-1$ (the indexes of specific flow channels are enumerated starting at 0). For each flow channel, the “always open” segments are placed within the control regions whose indices are found within their corresponding combinations, while the closeable segments are placed within the control regions whose indices are not found in their combination (Figure 39A). This results in every flow channel having a unique combination of *N/2* control regions that, when pressed, will result in every other flow channel becoming obstructed while that flow channel itself remains unobstructed. Having determined the positions for each flow channel in space (Figures 39B-C), the modular designs for the “always open” and “closeable” segments of the flow channels can be placed according to Figure 39A at within respective control regions/layers (Figure 39D). Because the “always open” and “closeable” segments are modular and fit with each other, once their geometry has been established, the segments can be positioned algorithmically according to this protocol using programmatic computer-aided design software in order to generate these

complex, aperiodic/irregular 3D structures for valve arrays or arbitrary designs or complexity that would be extremely difficult and cumbersome to design by hand.

Figure 39. Design of a 3x6x6 3D-Printed, Vertically Stacked Valve Array with 18 Independently Addressable Flow Channels

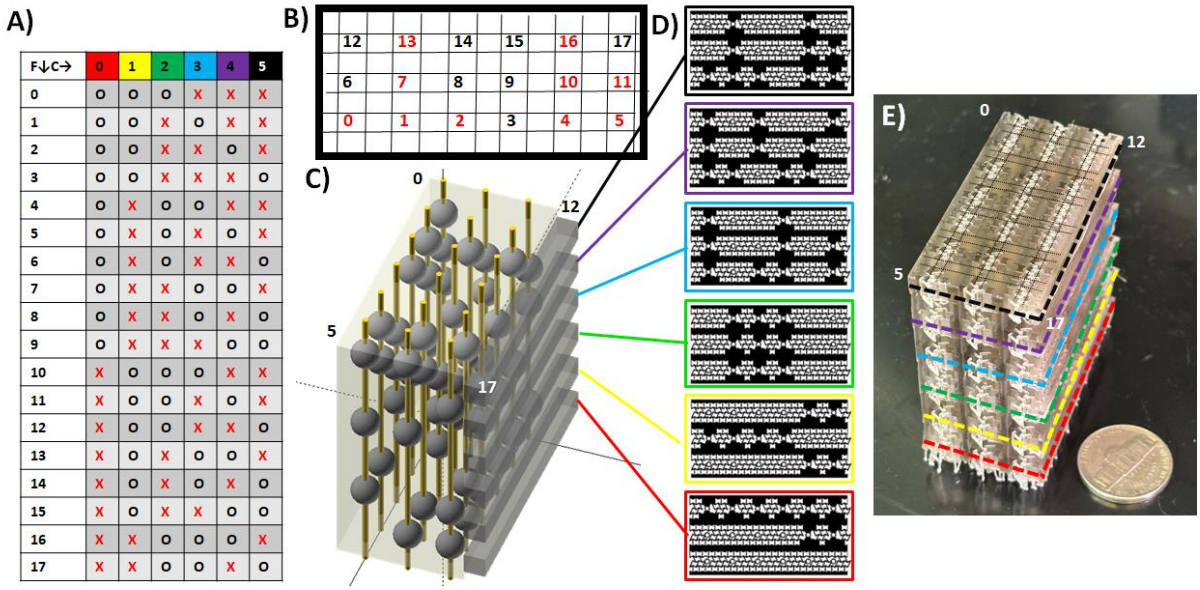

Note. A) For an eighteen fluid channel fluidic device (labeled from 0 to 17), we require six control regions (labeled from 0 to 5). To determine the positions of "closeable" and "always open" segments to uniquely allow only a single channel to be opened when pressure is applied to any three (= 6/2) control regions, first we enumerate all unique combinations of three control regions for, marking an "O" at those regions and an "X" for "closeable" segments at the regions not in that last. B) For 3 × 6 flow channels, the positions of each channel through a control region are mapped, for example, for control region 5 (black). C) The positions of closed channels (spheres, as in Figure 32D) and mapped to a 3D structure with control regions highlighted as dark gray bars. D) The 3D geometries for the modular "always open" and "closeable" segments

(as in Figure 36A) are positioned within each independent layer. E) The design can then be 3D printed.

In order to open a specific flow channel *i*, the combination of control regions to be compressed can be found using a look-up table (*i.e.*, Figure 39A) so those respective control regions can be compressed. In the case of arbitrarily complex structures, the control regions to compress to open specific flow channel *i* can be quickly determined using the algorithm:[143]

1) Find max(c_k such that (c_k choose k) $\leq$ ($N - 1 - i$))
2) Find max(c_{k-1} such that (c_{k-1} choose ($k - 1$)) $\leq$ ($N - 1 - i$) - (c_k choose k))

   . . .

3) Find max(c_1 such that (c_1 choose *1*) $\leq$ (N – 1 – i) – (sum [(c_{k-j} choose $k - j$)] for j from [1 to k]))
4) Compress control regions [($N - 1$) - c_1, ($N - 1$) - c_2,... ($N - 1$) - c_k]

where *(c choose k) = c!/((k!) ×(c-k)!)*. The ability to algorithmically position different segments to generate individually addressable arrays of flow channels and to algorithmically determine the inputs required to control any individual channel means this design approach can be used for arbitrarily complex structures, for example, a 96-flow channel array (8x12) requiring nine control valves, such that any four of nine will allow only a one of 96 channels to remain open (Figure 40).

Note that each control region contains a unique configuration of “always open” and “closeable” segments of each of the flow cells running through them, so that as complexity increases, algorithmic design of these modular segments becomes increasingly necessary.

Figure 40. Design and 3D-printing of a 8x12x9 Vertically Stacked Valve Array with 96 Independently Addressable Flow Channels

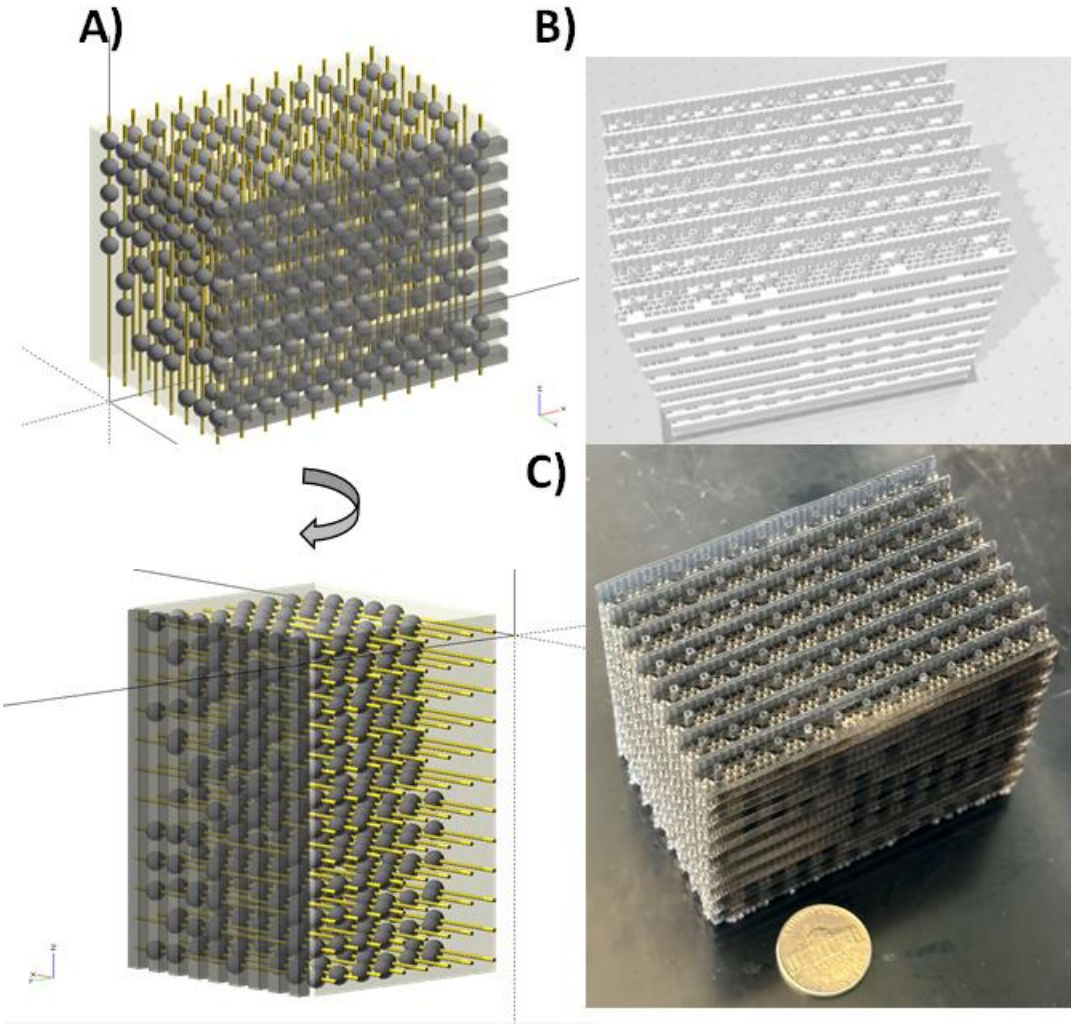

Note. Following the algorithm described in the text and demonstrated in Figure 39, A) multi-layer 3D printed valve arrays and nearly any geometry or complexity, such as this 96-flow channel valve array, can be algorithmically designed and B) an irregular/aperiodic structure generated in three dimensions to position the “always open” and “closeable” segments within each control region. C) These intriquite structures can then be 3D printed using a DLP printer. The design can be made to fit above a standard 96-well plate.

Conclusion

While re-entrant or auxetic metamaterials are often used "passively", where their unusual deformation properties are exploited for example to fit curved surfaces or minimize impact damage,[140, 141] we show that integrating 3D printed, flexible mechanical metamaterials into complex, algorithmically-designed fluidic valve architectures provides a way to expand a "Quake-style" valve arrays and active fluidic control into the "third dimension". Doing so, required precision positioning of solid and wire-framed (un-)tilted re-entrant cells at specific 3D locations in a manner that allowed control of the propagation of applied forces and programmable collapse or opening of specific flow channels uniformly along the structure of the device. To our knowledge, "multi-layer Quake-style" architectures have not been demonstrated otherwise, but without 3D printing doing so would require extensive expertise, effort, and expense to generate in a clean-room environment. Our use of commercially available, inexpensive DLP 3D printers and resins along with algorithmic design principles means that these technologies should be readily accessible, deployable, and customizable for different applications requiring fluidic control at various levels of complexity.

Conceivably, "closeable" and "always open" segments could be formed using materials with differing mechanical properties at the targeted regions.[145] However, employing DLP 3D printing technologies to simultaneously print two different materials into an integrated, composite device introduces significant technical complexities.[146] Trying to construct such an intricate composite device at the scales we are interested in (sub-mm to sub-cm) without employing DLP printing technique would indeed be quite challenging. Additionally, considering that one of the significant advantages of using DLP printing approach in these applications is its capability to fabricate all the channels in an array simultaneously, alternative non-DLP

approaches are unlikely capable of scaling for controlling the extensive fluidic channels that we aim for. Therefore, rather than resorting to different materials with varied mechanical properties to define these segments, we can leverage mechanical metamaterials with finely tuned mechanical behavior achieved through their internal microstructure. This approach allows us to fully utilize the benefits of DLP printing technology, enabling the fabrication of unified and intricately designed fluidic devices in three dimensions.

Applying pressure to the control regions of these devices could in principle be performed using automated mechanical actuators or pneumatic pressure, using open-source control systems that have already been designed for "Quake-style" valves in microfluidic systems.[147, 148] The key is that our approach similarly allows a single, individually-addressable flow channel to remain open within the 3D structure of the device and so the operation of our devices is functionally analogous and crucially, scales to similarly to potentially control very large numbers of channels with significantly fewer control inputs. We anticipate that the multilayer 3D-printed valve systems we present can help in the development of microfluidic systems for high-throughput applications in biotechnology and medicine. Further optimization of resins and auxetic cell architectures promises to enable larger, more complex devices and active operations that exploit the unusual properties of engineered mechanical metamaterials.

Experimental Section

Materials

3D printing was performed using a commercially available Elegoo Mars 2 or Mars 3 printer. The resin consisted of a mixture SuperFlex resin (3D Materials) and Plant-Based UV Resin (SUNLU) in a ratio of 10:1.

Valve Design, Fabrication, and Post-Processing

The valves were designed using the OpenSCAD[21] version 2023.11.29 (git 185ce268a) software and exported as STL files.[149, 150] The .scad files and scripts to generate the mechanical metamaterial structures according to the algorithms described in the manuscript are available at: https://github.com/ejosephslab/mechanical_metamaterial/. The STL files were sliced using Chitubox v1.9.4 (CBD-Tech) with the settings: Bottom layer exposure time (25 s) and intermediate layers (3 s) while other settings were kept at default. The layer step size is precisely set at 50 microns to ensure accurate and controlled layering. The resulting .CBT files were then printed using a commercially available Elegoo Mars 2 printer. This printer incorporates a projector that projects light over the entire layer, facilitating the simultaneous curing of the resin. After the printing process, the structures retained unpolymerized resin in the flow channels, which was purged through multiple rinses with isopropyl alcohol (IPA). Following this, the printed structures underwent a cleaning and drying process using dry air, followed by sonication in deionized water for 5 min. After sonication, the structures were once again dried and cured with a UV lamp for 5 min.

Uniaxial Compression Test of Re-Entrant Valves at Different Values of θ and φ

Uniaxial compression tests of the specimens at different values of θ and φ were performed using the Torbal force gauge at the crosshead speed of 10mm/min. The structures were compressed corresponding to the distance the inner layers were fully compressed.

Fatigue Measurement

A fatigue performance analysis was conducted on the engineered metamaterial 5×5 grids (Figure 34A, B; Figure S5, Supporting Information; which are four layers of five re-entrant cells capped by two half-layers of solid, "filled-in" auxetic cells). The structure was subjected to repeated cycles of compression and reopening, totaling ≈ 1000 cycles (equivalent to 9 h). This testing was carried out using the Torbal forge gauge at the minimum possible crosshead speed of 10mm/min. The compression distance for each cycle precisely matched the distance required for the complete closure of the closeable valve, leading to the shutdown of flow, as previously experimentally tested (Figure 36A,B). Remarkably, the valve showed no signs of collapse throughout this extensive cycling.

Flow Rate Measurement in the Flow Channels

Flow rates within the flow channels in the 3D-printed valve device used a pressure controller (OB1 Base MkIII, Elveflow, Paris, France) connected to a liquid reservoir and BFS1 Coriolis based flow sensor. The pressure controller, as above exerts a constant pressure on the liquid reservoir which pushes liquid into the printed valve. The input to the flow channels in the printed valve was connected to the BFS1 flow sensor which measures the fluid flow rate at the given regulator pressure. The readings were performed for the two configurations of flow channels in the printed structures, one "closeable" and one "always open".

Finite Element Analysis (FEA)

Models of the re-entrant grids were built in the FreeCAD (https://github.com/FreeCAD/FreeCAD) Sketcher workbench with the parameters as shown in Figure 35. As described in the main text, the lengths of the side and re-entrant segments of each reentrant unit were calculated so that five unit cells would fit across 9 mm x 9 mm total area, with a thickness of 5 mm. A mesh was generated using Netgen. The structure was assigned a Young's modulus of 6.0 GPa and for the compressive force of 100 to 1000 N applied to the top of the solved using CalculiX. A Python script was written to generate these structures to perform these calculations values for each θ and φ in increments of 100 N, and then determine for the Y displacement minimum and output the results. Spring constants were then estimated by fitting a line to the linear (low force) segments of the simulated force versus displacement curves. For the individual cells (bowties) calculations were performed similarly except simulations were performed only for forces between 1 to and 10 N.

Data availability

Scripts to generate the STL files to print the 3D mechanical metamaterial structures are available at: https://github.com/ejosephslab/mechanical_metamaterial/

CHAPTER IV: CONCLUSION

In Chapter I, a computational algorithm was developed for the design of CRISPR gRNAs, termed polyvalent guide RNAs (pgRNAs), which are optimized for simultaneous activity at multiple viral target sites. The algorithm utilized the inherent tolerance of certain CRISPR effectors, such as Cas13a and Cas9, to mismatches between their guide RNA (gRNA) sequences and their target sites to optimize the efficiency of a single guide RNA at multiple viral sites that are similar but not exactly identical. Our analysis demonstrated that these homoeologous sequences are abundant in viral genomes and can be simultaneously targeted by our engineered "polyvalent" gRNAs (pgRNAs), emphasizing the broad applicability and effectiveness of our approach. Additionally, these engineered pgRNAs target multiple viral sites without increasing the risk of "off-target activity" by maintaining significant divergence from the host genome.

Further, the feasibility of our algorithm was verified through experimental implementation. Experimentally, remarkable antiviral efficacy was observed in *Nicotiana benthamiana*, a model tobacco organism, even with multiple mismatches with their viral targets when using pgRNAs with Cas13. The reduction in viral RNA was 30- to 40-fold compared to monovalent gRNAs, showcasing the superior performance of pgRNAs. Moreover, i*n vitro* experiments demonstrated that pgRNAs, despite imperfect complementarity, could be tailored to induce Cas13's "collateral activity" for viral detection at viral target pairs with sequences diverging by up to 25%. Furthermore, these pgRNAs were capable of guiding DNA-targeting CRISPR-Cas9 to degrade multiple DNA targets ex vivo, even with sequence divergence reaching 40%, involving mismatches at 8 out of 20 base pairs. Thus, key challenges in CRISPR

antiviral applications, such as multiplexing and preventing escape, as well as accommodating clinical variation and viral sequence heterogeneity, were specifically addressed by our gRNA design algorithm which highlighted the distinctive need for an alternate strategy for designing CRISPR gRNAs for antiviral applications.

Next in Chapter II, we demonstrated a highly parallelized method, compartmentalized CRISPR reactions (CCR) technique, for identifying highly active and specific gRNA variants from extensive sets of gRNA/target/off-target combinations. The CCR approach confines the entire CRISPR reaction, including gRNA transcription and target cleavage, within individual water-in-oil microemulsion, providing a robust yet straightforward means for efficiently screening numerous gRNA candidates obtained from various computational tools for gRNA design, for both activity and specificity. Moreover, the CCR approach enabled the high-throughput screening of effective extended gRNAs (x-gRNAs) which eliminates the off-target activity of the associated gRNAs while still maintaining its on-target activity. Consequently, the CCR methodology presents an alternative strategy to address the limitations of traditional CRISPR gRNA screening methods, characterized by their low throughput and complexity.

Lastly, in chapter III, a technique was demonstrated to scale microfluidic systems, which find utility in various advanced applications in medical diagnostics, lab-on-chips, and laboratory automation. A pivotal role within microfluidic systems is played by microfluidic valves, as they regulate fluid flow through distinct microchannels. While microfluidic systems are typically confined to planar structures, 3D printing enables new capabilities to generate complex designs for fluidic circuits with higher densities and integrated components. However, the control of fluids within 3D structures poses several challenges, rendering effective scaling difficult, and resulting in many fluidic devices often being restricted to quasi-planar structures. Here, a

systematic computational and experimental characterization was conducted on a modified re-entrant honeycomb structure to create a modular metamaterial for an active device. This device allows for the direct regulation of flow through integrated, multiplexed fluidic channels "one-at-a-time," in a highly scalable manner.

In summary, this dissertation has introduced high-throughput techniques, such as multiplexed CRISPR-based antivirals, the compartmentalized CRISPR reactions (CCR) technique, and scaling of fluidic systems with 3D printed fluidic valves made by mechanical metamaterials. These advancements will improve the efficiency and scalability of various life sciences techniques across biotechnology, medicine, and diagnostics.

REFERENCES

1. Abbott, T.R., Dhamdhere, G., Liu, Y., Lin, X., Goudy, L., Zeng, L., Chemparathy, A., Chmura, S., Heaton, N.S., Debs, R., *et al.* (2020). Development of CRISPR as an Antiviral Strategy to Combat SARS-CoV-2 and Influenza. Cell *181*, 865-876.e812.
2. Abudayyeh, O.O., Gootenberg, J.S., Konermann, S., Joung, J., Slaymaker, I.M., Cox, D.B., Shmakov, S., Makarova, K.S., Semenova, E., and Minakhin, L. (2016). C2c2 is a single-component programmable RNA-guided RNA-targeting CRISPR effector. Science *353*, aaf5573.
3. Ackerman, C.M., Myhrvold, C., Thakku, S.G., Freije, C.A., Metsky, H.C., Yang, D.K., Simon, H.Y., Boehm, C.K., Kosoko-Thoroddsen, T.-S.F., and Kehe, J. (2020). Massively multiplexed nucleic acid detection with Cas13. Nature, 1-6.
4. Aman, R., Mahas, A., Butt, H., Ali, Z., Aljedaani, F., and Mahfouz, M. (2018). Engineering RNA virus interference via the CRISPR/Cas13 machinery in Arabidopsis. Viruses *10*, 732.
5. Blanchard, E.L., Vanover, D., Bawage, S.S., Tiwari, P.M., Rotolo, L., Beyersdorf, J., Peck, H.E., Bruno, N.C., Hincapie, R., and Michel, F. (2021). Treatment of influenza and SARS-CoV-2 infections via mRNA-encoded Cas13a in rodents. Nature Biotechnology, 1-10.
6. Broughton, J.P., Deng, X., Yu, G., Fasching, C.L., Servellita, V., Singh, J., Miao, X., Streithorst, J.A., Granados, A., and Sotomayor-Gonzalez, A. (2020). CRISPR–Cas12-based detection of SARS-CoV-2. Nature Biotechnology, 1-5.

7. Camacho, C., Coulouris, G., Avagyan, V., Ma, N., Papadopoulos, J., Bealer, K., and Madden, T.L. (2009). BLAST+: architecture and applications. BMC bioinformatics *10*, 1-9.
8. Darcis, G., Binda, C.S., Klaver, B., Herrera-Carrillo, E., Berkhout, B., and Das, A.T. (2019). The impact of HIV-1 genetic diversity on CRISPR-Cas9 antiviral activity and viral escape. Viruses *11*, 1-14.
9. Doench, J.G., Fusi, N., Sullender, M., Hegde, M., Vaimberg, E.W., Donovan, K.F., Smith, I., Tothova, Z., Wilen, C., and Orchard, R. (2016). Optimized sgRNA design to maximize activity and minimize off-target effects of CRISPR-Cas9. Nature biotechnology.
10. Gao, Z., Fan, M., Das, A.T., Herrera-Carrillo, E., and Berkhout, B. (2020). Extinction of all infectious HIV in cell culture by the CRISPR-Cas12a system with only a single crRNA. Nucleic Acids Research, 1-13.
11. Gootenberg, J.S., Abudayyeh, O.O., Kellner, M.J., Joung, J., Collins, J.J., and Zhang, F. (2018). Multiplexed and portable nucleic acid detection platform with Cas13, Cas12a, and Csm6. Science 360, 439-444.
12. Gootenberg, J.S., Abudayyeh, O.O., Lee, J.W., Essletzbichler, P., Dy, A.J., Joung, J., Verdine, V., Donghia, N., Daringer, N.M., and Freije, C.A. (2017). Nucleic acid detection with CRISPR-Cas13a/C2c2. Science 356, 438-442.
13. Guo, X., Rahman, J.A., Wessels, H.-H., Méndez-Mancilla, A., Haro, D., Chen, X., and Sanjana, N.E. (2021). Transcriptome-wide Cas13 guide RNA design for model organisms and viral RNA pathogens. Cell Genomics 1, 100001.

14. Mahas, A., Aman, R., and Mahfouz, M. (2019). CRISPR-Cas13d mediates robust RNA virus interference in plants. Genome Biology *20*, 1-16.

15. Li, G., Wang, X., Liu, Y., Lv, X., Li, G., Zhao, C., Wang, D., Huang, X., and Hu, X. (2020a). Porcine reproductive and respiratory syndrome virus (PRRSV) inhibition with engineered Cas13d. Journal of Genetics and Genomics.

16. Li, H., Wang, S., Dong, X., Li, Q., Li, M., Li, J., Guo, Y., Jin, X., Zhou, Y., Song, H., *et al.* (2020b). CRISPR-Cas13a Cleavage of Dengue Virus NS3 Gene Efficiently Inhibits Viral Replication. Molecular Therapy - Nucleic Acids *19*, 1460-1469.

17. Freije, C.A., Myhrvold, C., Boehm, C.K., Lin, A.E., Welch, N.L., Carter, A., Metsky, H.C., Luo, C.Y., Abudayyeh, O.O., and Gootenberg, J.S. (2019). Programmable inhibition and detection of RNA viruses using Cas13. Molecular cell *76*, 826-837. e811.

18. Lebbink, R.J., De Jong, D.C., Wolters, F., Kruse, E.M., Van Ham, P.M., Wiertz, E.J., and Nijhuis, M. (2017). A combinational CRISPR/Cas9 gene-editing approach can halt HIV replication and prevent viral escape. Scientific reports *7*, 41968.

19. Yan, W.X., Chong, S., Zhang, H., Makarova, K.S., Koonin, E.V., Cheng, D.R., and Scott, D.A. (2018). Cas13d is a compact RNA-targeting type VI CRISPR effector positively modulated by a WYL-domain-containing accessory protein. Molecular cell *70*, 327-339. e325.

20. Yin, D., Ling, S., Wang, D., Dai, Y., Jiang, H., Zhou, X., Paludan, S.R., Hong, J., and Cai, Y. (2021). Targeting herpes simplex virus with CRISPR–Cas9 cures herpetic stromal keratitis in mice. Nature Biotechnology, 1-11.

21. Lee, C. (2019). CRISPR/Cas9-based antiviral strategy: Current status and the potential challenge. Molecules *24*.

22. Myhrvold, C., Freije, C.A., Gootenberg, J.S., Abudayyeh, O.O., Metsky, H.C., Durbin, A.F., Kellner, M.J., Tan, A.L., Paul, L.M., and Parham, L.A. (2018). Field-deployable viral diagnostics using CRISPR-Cas13. Science *360*, 444-448.

23. Konermann, S., Lotfy, P., Brideau, N.J., Oki, J., Shokhirev, M.N., and Hsu, P.D. (2018). Transcriptome engineering with RNA-targeting type VI-D CRISPR effectors. Cell *173*, 665-676. e614.

24. Lindbo, J.A. (2007). TRBO: a high-efficiency tobacco mosaic virus RNA-based overexpression vector. Plant physiology 145, 1232-1240.

25. Fareh, M., Zhao, W., Hu, W., Casan, J.M., Kumar, A., Symons, J., Zerbato, J.M., Fong, D., Voskoboinik, I., and Ekert, P.G. (2021). Reprogrammed CRISPR-Cas13b suppresses SARS-CoV-2 replication and circumvents its mutational escape through mismatch tolerance. Nature communications *12*, 1-16.

26. Listgarten, J., Weinstein, M., Kleinstiver, B.P., Sousa, A.A., Joung, J.K., Crawford, J., Gao, K., Hoang, L., Elibol, M., and Doench, J.G. (2018). Prediction of off-target activities for the end-to-end design of CRISPR guide RNAs. Nature biomedical engineering *2*, 38-47.

27. Wessels, H.H., Méndez-Mancilla, A., Guo, X., Legut, M., Daniloski, Z., and Sanjana, N.E. (2020). Massively parallel Cas13 screens reveal principles for guide RNA design. Nature Biotechnology.

28. Fozouni, P., Son, S., de León Derby, M.D., Knott, G.J., Gray, C.N., D'Ambrosio, M.V., Zhao, C., Switz, N.A., Kumar, G.R., and Stephens, S.I. (2021). Amplification-free detection of SARS-CoV-2 with CRISPR-Cas13a and mobile phone microscopy. Cell *184*, 323-333. e329.

29. Doench, J.G., Hartenian, E., Graham, D.B., Tothova, Z., Hegde, M., Smith, I., Sullender, M., Ebert, B.L., Xavier, R.J., and Root, D.E. (2014). Rational design of highly active sgRNAs for CRISPR-Cas9-mediated gene inactivation. Nature biotechnology.

30. Hatcher, E.L., Zhdanov, S.A., Bao, Y., Blinkova, O., Nawrocki, E.P., Ostapchuck, Y., Schäffer, A.A., and Brister, J.R. (2017). Virus Variation Resource–improved response to emergent viral outbreaks. Nucleic acids research *45*, D482-D490.

31. Tycko, J., Barrera, L.A., Huston, N.C., Friedland, A.E., Wu, X., Gootenberg, J.S., Abudayyeh, O.O., Myer, V.E., Wilson, C.J., and Hsu, P.D. (2018). Pairwise library screen systematically interrogates Staphylococcus aureus Cas9 specificity in human cells. Nature communications *9*, 1-7.

32. Zhang, C., Konermann, S., Brideau, N.J., Lotfy, P., Wu, X., Novick, S.J., Strutzenberg, T., Griffin, P.R., Hsu, P.D., and Lyumkis, D. (2018). Structural basis for the RNA-guided ribonuclease activity of CRISPR-Cas13d. Cell *175*, 212-223. e217.

33. Kleinstiver, B.P. et al. Engineered CRISPR–Cas12a variants with increased activities and improved targeting ranges for gene, epigenetic and base editing. *Nature biotechnology* **37**, 276-282 (2019).

34. Sanson, K.R. et al. Optimization of AsCas12a for combinatorial genetic screens in human cells. *bioRxiv*, 747170 (2019).

35. Lorenz, R. et al. ViennaRNA Package 2.0. *Algorithms for molecular biology* **6**, 26 (2011).

36. Nakasugi, K., Crowhurst, R., Bally, J., and Waterhouse, P. (2014). Combining transcriptome assemblies from multiple de novo assemblers in the allo-tetraploid plant Nicotiana benthamiana. PloS one 9, e91776.

37. Tong, H., Huang, J., Xiao, Q., He, B., Dong, X., Liu, Y., Yang, X., Han, D., Wang, Z., and Wang, X. (2022). High-fidelity Cas13 variants for targeted RNA degradation with minimal collateral effects. Nature Biotechnology, 1-12.

38. Sharma, V.K., Marla, S., Zheng, W., Mishra, D., Huang, J., Zhang, W., Morris, G.P., and Cook, D.E. (2022). CRISPR guides induce gene silencing in plants in the absence of Cas. Genome biology *23*, 1-24.

39. Nalefski, E.A., Patel, N., Leung, P.J., Islam, Z., Kooistra, R.M., Parikh, I., Marion, E., Knott, G.J., Doudna, J.A., and Le Ny, A.-L.M. (2021). Kinetic analysis of Cas12a and Cas13a RNA-Guided nucleases for development of improved CRISPR-Based diagnostics. Iscience *24*, 102996.

40. Lin, X., Liu, Y., Chemparathy, A., Pande, T., La Russa, M., and Qi, L.S. (2021). A comprehensive analysis and resource to use CRISPR-Cas13 for broad-spectrum targeting of RNA viruses. Cell Reports Medicine *2*, 100245.

41. Kim, S., Kim, D., Cho, S.W., Kim, J., and Kim, J.-S. (2014). Highly efficient RNA-guided genome editing in human cells via delivery of purified Cas9 ribonucleoproteins. Genome research *24*, 1012-1019.

42. Shmakov, S., Smargon, A., Scott, D., Cox, D., Pyzocha, N., Yan, W., Abudayyeh, O.O., Gootenberg, J.S., Makarova, K.S., and Wolf, Y.I. (2017). Diversity and evolution of class 2 CRISPR–Cas systems. Nature Reviews Microbiology *15*, 169.

43. Özcan, A., Krajeski, R., Ioannidi, E., Lee, B., Gardner, A., Makarova, K.S., Koonin, E.V., Abudayyeh, O.O., and Gootenberg, J.S. (2021). Programmable RNA targeting with the single-protein CRISPR effector Cas7-11. Nature 597, 720-725.

44. Ran, F. A., Hsu, P. D., Wright, J., Agarwala, V., Scott, D. A., & Zhang, F. (2013). Genome engineering using the CRISPR-Cas9 system. Nature Protocols, 8(11), 2281-2308.

45. Hsu, P. D., Lander, E. S., & Zhang, F. (2014). Development and applications of CRISPR-Cas9 for genome engineering. Cell, 157(6), 1262-1278.

46. Jiang, F., & Doudna, J. A. (2017). CRISPR-Cas9 Structures and Mechanisms. Annual Reviews of Biophysics, 46, 505-529.

47. Sternberg, S. H., Redding, S., Jinek, M., Greene, E. C., & Doudna, J. A. (2014). DNA interrogation by the CRISPR RNA-guided endonuclease Cas9. Nature, 7490, 62–67.

48. Jinek, M., Jiang, F., Taylor, D. W., Sternberg, S. H., Kaya, E., Ma, E., Anders, C., Hauer, M., Zhou, K., Lin, S., & Kaplan, M. (2014). Structures of Cas9 endonucleases reveal RNA-mediated conformational activation. Science, 343(6176), 1247997.

49. . Nishimasu, H., Ran, F. A., Hsu, P. D., Konermann, S., Shehata, S. I., Dohmae, N., Ishitani, R., Zhang, F., & Nureki, O. (2014). Crystal structure of Cas9 in complex with guide RNA and target DNA. Cell, 156(5), 935-949.

50. Anders, C., Niewoehner, O., Duerst, A., & Jinek, M. (2014). Structural basis of PAM-dependent target DNA recognition by the Cas9 endonuclease. Nature, 513(7519), 569-573.

51. Kosicki, M., Tomberg, K., & Bradley, A. (2018). Repair of double-strand breaks induced by CRISPR–Cas9 leads to large deletions and complex rearrangements. Nature biotechnology, 36(8), 765-771.

52. Brinkman, E. K., Chen, T., de Haas, M., Holland, H. A., Akhtar, W., & van Steensel, B. (2018). Kinetics and fidelity of the repair of Cas9-induced double-strand DNA breaks. Molecular cell, 70(5), 801-813.

53. Allen, F., Crepaldi, L., Alsinet, C., Strong, A. J., Kleshchevnikov, V., De Angeli, P., Páleníková, P., Khodak, A., Kiselev, V., Kosicki, M., & Bassett, A. R. (2019). Predicting the mutations generated by repair of Cas9-induced double-strand breaks. Nature biotechnology, 37(1), 64-72.

54. Gagnon, J. A., Valen, E., Thyme, S. B., Huang, P., Ahkmetova, L., Pauli, A., Montague, T. G., Zimmerman, S., Richter, C., & Schier, A. F. (2014). Efficient mutagenesis by Cas9 protein-mediated oligonucleotide insertion and large-scale assessment of single-guide RNAs. PloS one, 9(5), e98186.

55. Jiang, F., Taylor, D. W., Chen, J. S., Kornfeld, J. E., Zhou, K., Thompson, A. J., Nogales, E., & Doudna, J. A. (2016). Structures of a CRISPR-Cas9 R-loop complex primed for DNA cleavage. Science, 351(6275), 867-871.

56. Mullally, G., Van Aelst, K., Naqvi, M. M., Diffin, F. M., Karvelis, T., Gasiunas, G., Siksnys, V., & Szczelkun, M. D. (2020). 5′ modifications to CRISPR–Cas9 gRNA can change the dynamics and size of R-loops and inhibit DNA cleavage. Nucleic acids research, 48(12), 6811-6823.

57. Rychlik, W. (1993). Selection of primers for polymerase chain reaction. PCR protocols: current methods and applications, 31-40.

58. Mann, T., Humbert, R., Dorschner, M., Stamatoyannopoulos, J., & Noble, W. S. (2009). A thermodynamic approach to PCR primer design. Nucleic acids research, 37(13), e95-e95.

59. Doench, J. G., Fusi, N., Sullender, M., Hegde, M., Vaimberg, E. W., Donovan, K. F., Smith, I., Tothova, Z., Wilen, C., Orchard, R., & Virgin, H. W. (2016). Optimized sgRNA design to maximize activity and minimize off-target effects of CRISPR-Cas9. Nature biotechnology, 34(2), 184-191

60. Moreno-Mateos, M. A., Vejnar, C. E., Beaudoin, J. D., Fernandez, J. P., Mis, E. K., Khokha, M. K., & Giraldez, A. J. (2015). CRISPRscan: designing highly efficient sgRNAs for CRISPR-Cas9 targeting in vivo. Nature methods, 12(10), 982-988.

61. Stemmer, M., Thumberger, T., del Sol Keyer, M., Wittbrodt, J., & Mateo, J. L. (2015). CCTop: an intuitive, flexible and reliable CRISPR/Cas9 target prediction tool. PloS one, 10(4), e0124633.

62. . Chen, W., McKenna, A., Schreiber, J., Haeussler, M., Yin, Y., Agarwal, V., Noble, W. S., & Shendure, J. (2019). Massively parallel profiling and predictive modeling of the outcomes of CRISPR/Cas9-mediated double-strand break repair. Nucleic acids research, 47(15), 7989-8003.

63. Xu, H., Xiao, T., Chen, C. H., Li, W., Meyer, C. A., Wu, Q., & Liu, X. S. (2015). Sequence determinants of improved CRISPR sgRNA design. Genome Research, 25(8), 1147-1157.

64. Wong, N., Liu, W., & Wang, X. (2015). WU-CRISPR: characteristics of functional guide RNAs for the CRISPR/Cas9 system. Genome Biology, 16, 1-8.

65. Doench, J. G., Hartenian, E., Graham, D. B., Tothova, Z., Hegde, M., Smith, I., Sullender, M., Ebert, B. L., Xavier, R. J., & Root, D. E. (2014). Rational design of highly active sgRNAs for CRISPR-Cas9–mediated gene inactivation. Nature biotechnology, 32(12), 1262-1267.

66. Wang, D., Zhang, C., Wang, B., Li, B., Wang, Q., Liu, D., Wang, H., Zhou, Y., Shi, L., Lan, F., & Wang, Y. (2019). Optimized CRISPR guide RNA design for two high-fidelity Cas9 variants by deep learning. Nature communications, 10(1), 4284.

67. Fusi, N., Smith, I., Doench, J., & Listgarten, J. (2015). In silico predictive modeling of CRISPR/Cas9 guide efficiency. BioRxiv, 021568.

68. Chari, R., Yeo, N. C., Chavez, A., & Church, G. M. (2017). sgRNA Scorer 2.0: a species-independent model to predict CRISPR/Cas9 activity. ACS synthetic biology, 6(5), 902-904.

69. Chuai, G., Ma, H., Yan, J., Chen, M., Hong, N., Xue, D., & Liu, Q. (2018). DeepCRISPR: optimized CRISPR guide RNA design by deep learning. Genome Biology, 19, 1-18.

70. Listgarten, J., Weinstein, M., Kleinstiver, B.P., Sousa, A.A., Joung, J.K., Crawford, J., Gao, K., Hoang, L., Elibol, M., Doench, J.G., & Fusi, N. (2018). Prediction of off-target activities for the end-to-end design of CRISPR guide RNAs. Nature biomedical engineering, 2(1), 38-47.

71. Bae, S., Park, J., & Kim, J. S. (2014). Cas-OFFinder: a fast and versatile algorithm that searches for potential off-target sites of Cas9 RNA-guided endonucleases. Bioinformatics, 30(10), 1473-1475.

72. . Hsu, P.D., Scott, D.A., Weinstein, J.A., Ran, F.A., Konermann, S., Agarwala, V., Li, Y., Fine, E.J., Wu, X., Shalem, O., & Cradick, T.J. (2013). DNA targeting specificity of RNA-guided Cas9 nucleases. Nature Biotechnology, 31(9), 827-832.

73. Pliatsika, V., & Rigoutsos, I. (2015). “Off-Spotter”: very fast and exhaustive enumeration of genomic lookalikes for designing CRISPR/Cas guide RNAs. Biology direct, 10, 1-10.

74. Xie, S., Shen, B., Zhang, C., Huang, X., & Zhang, Y. (2014). sgRNAcas9: a software package for designing CRISPR sgRNA and evaluating potential off-target cleavage sites. PloS one, 9(6), e100448.

75. Haeussler, M., Schönig, K., Eckert, H., Eschstruth, A., Mianné, J., Renaud, J.B., Schneider-Maunoury, S., Shkumatava, A., Teboul, L., Kent, J., & Joly, J.S. (2016). Evaluation of off-target and on-target scoring algorithms and integration into the guide RNA selection tool CRISPOR. Genome Biology, 17, 1-12.

76. Sentmanat, M. F., Peters, S. T., Florian, C. P., Connelly, J. P., & Pruett-Miller, S. M. (2018). A survey of validation strategies for CRISPR-Cas9 editing. Scientific reports, 8(1), 888.

77. Tsai, S. Q., Nguyen, N. T., Malagon-Lopez, J., Topkar, V. V., Aryee, M. J., & Joung, J. K. (2017). CIRCLE-seq: a highly sensitive in vitro screen for genome-wide CRISPR–Cas9 nuclease off-targets. Nature methods, 14(6), 607-614.

78. Arndell, T., Sharma, N., Langridge, P., Baumann, U., Watson-Haigh, N. S., & Whitford, R. (2019). gRNA validation for wheat genome editing with the CRISPR-Cas9 system. BMC biotechnology, 19, 1-12.

79. Zhou, Y., Zhu, S., Cai, C., Yuan, P., Li, C., Huang, Y., & Wei, W. (2014). High-throughput screening of a CRISPR/Cas9 library for functional genomics in human cells. Nature, 509(7501), 487-491.

80. Jason, S. L., & Yusa, K. (2019). Genome-wide CRISPR-Cas9 screening in mammalian cells. Methods, 164, 29-35.

81. Bock, C., Datlinger, P., Chardon, F., Coelho, M.A., Dong, M.B., Lawson, K.A., Lu, T., Maroc, L., Norman, T.M., Song, B., & Stanley, G. (2022). High-content CRISPR screening. Nature Reviews Methods Primers, 2(1), 1-23.

82. Wang, T., Wei, J. J., Sabatini, D. M., & Lander, E. S. (2014). Genetic screens in human cells using the CRISPR-Cas9 system. Science, 343(6166), 80-84.

83. Terekhov, S.S., Eliseev, I.E., Ovchinnikova, L.A., Kabilov, M.R., Prjibelski, A.D., Tupikin, A.E., Smirnov, I.V., Belogurov Jr, A.A., Severinov, K.V., Lomakin, Y.A., & Altman, S. (2020). Liquid drop of DNA libraries reveals total genome information. Proceedings of the National Academy of Sciences, 117(44), 27300-27306.

84. Williams, R., Peisajovich, S. G., Miller, O. J., Magdassi, S., Tawfik, D. S., & Griffiths, A. D. (2006). Amplification of complex gene libraries by emulsion PCR. Nature methods, 3(7), 545-550.

85. Griffiths, A. D., & Tawfik, D. S. (2006). Miniaturising the laboratory in emulsion droplets. Trends in Biotechnology, 24(9), 395-402.

86. Shao, K., Ding, W., Wang, F., Li, H., Ma, D., & Wang, H. (2011). Emulsion PCR: a high efficient way of PCR amplification of random DNA libraries in aptamer selection. PLoS One, 6(9), e24910.

87. Paegel, B. M., & Joyce, G. F. (2010). Microfluidic compartmentalized directed evolution. Chemistry & Biology, 17, 717–724.

88. Hindson, B.J., Ness, K.D., Masquelier, D.A., Belgrader, P., Heredia, N.J., Makarewicz, A.J., Bright, I.J., Lucero, M.Y., Hiddessen, A.L., Legler, T.C., & Kitano, T.K. (2011). High-throughput droplet digital PCR system for absolute quantitation of DNA copy number. Analytical Chemistry, 83(22), 8604-8610.

89. Tawfik, D. S., & Griffiths, A. D. (1998). Man-made cell-like compartments for molecular evolution. Nature Biotechnology, 16(7), 652-656.

90. Bernath, K., Hai, M., Mastrobattista, E., Griffiths, A. D., Magdassi, S., & Tawfik, D. S. (2004). In vitro compartmentalization by double emulsions: sorting and gene enrichment by fluorescence activated cell sorting. Analytical Biochemistry, 325(1), 151-157.

91. Miller, O.J., Bernath, K., Agresti, J.J., Amitai, G., Kelly, B.T., Mastrobattista, E., Taly, V., Magdassi, S., Tawfik, D.S., & Griffiths, A.D. (2006). Directed evolution by in vitro compartmentalization. Nature Methods, 3(7), 561-570.

92. Schaerli, Y., & Hollfelder, F. (2009). The potential of microfluidic water-in-oil droplets in experimental biology. Molecular Biosystems, 5(12), 1392-1404.

93. Taly, V., Kelly, B. T., & Griffiths, A. D. (2007). Droplets as microreactors for high-throughput biology. ChemBioChem, 8(3), 263-272.

94. Kocak, D. D., Josephs, E. A., Bhandarkar, V., Adkar, S. S., Kwon, J. B., & Gersbach, C. A. (2019). Increasing the specificity of CRISPR systems with engineered RNA secondary structures. Nature Biotechnology, 37(6), 657-666.

95. Herring-Nicholas, A., Dimig, H., Roesing, M. R., & Josephs, E. A. (2024). Selection of extended CRISPR RNAs with enhanced targeting and specificity. Communications Biology, 7(1), 86.

96. Magoč, T., & Salzberg, S. L. (2011). FLASH: Fast length adjustment of short reads to improve genome assemblies. Bioinformatics, 27, 2957-2963.

97. Cock, P.J., Antao, T., Chang, J.T., Chapman, B.A., Cox, C.J., Dalke, A., Friedberg, I., Hamelryck, T., Kauff, F., Wilczynski, B., & Dhe Hoon, M.J. (2009). Biopython: freely

available Python tools for computational molecular biology and bioinformatics. Bioinformatics, 25(11), 1422.

98. Smith, T. F., & Waterman, M. S. (1981). Identification of common molecular subsequences. Journal of Molecular Biology, 147(1), 195-197.
99. Gravesen, P., Branebjerg, J., & Jensen, O. S. (1993). Microfluidics-a review. Journal of micromechanics and microengineering, 3(4), 168.
100. Oh, K. W., & Ahn, C. H. (2006). A review of microvalves. Journal of micromechanics and microengineering, 16(5), R13.
101. Ohno, K. I., Tachikawa, K., & Manz, A. (2008). Microfluidics: applications for analytical purposes in chemistry and biochemistry. Electrophoresis, 29(22), 4443-4453.
102. Gómez-Sjöberg, R., Leyrat, A. A., Pirone, D. M., Chen, C. S., & Quake, S. R. (2007). Versatile, fully automated, microfluidic cell culture system. Analytical chemistry, 79(22), 8557-8563.
103. Beebe, D. J., Mensing, G. A., & Walker, G. M. (2002). Physics and applications of microfluidics in biology. Annual review of biomedical engineering, 4(1), 261-286.
104. Yeo, L. Y., Chang, H. C., Chan, P. P., & Friend, J. R. (2011). Microfluidic devices for bioapplications. small, 7(1), 12-48.
105. Sackmann, E. K., Fulton, A. L., & Beebe, D. J. (2014). The present and future role of microfluidics in biomedical research. Nature, 507(7491), 181-189.
106. Haeberle, S., & Zengerle, R. (2007). Microfluidic platforms for lab-on-a-chip applications. Lab on a Chip, 7(9), 1094-1110.

107. Carvalho, M. R., Truckenmuller, R., Reis, R. L., & Oliveira, J. M. (2020). Biomaterials and microfluidics for drug discovery and development. Biomaterials-and Microfluidics-Based Tissue Engineered 3D Models, 121-135.

108. Dittrich, P. S., & Manz, A. (2006). Lab-on-a-chip: microfluidics in drug discovery. Nature reviews Drug discovery, 5(3), 210-218.

109. Cheong, R., Wang, C. J., & Levchenko, A. (2009). High content cell screening in a microfluidic device. Molecular & Cellular Proteomics, 8(3), 433-442.

110. Briones, J., Espulgar, W., Koyama, S., Takamatsu, H., Tamiya, E., & Saito, M. (2021). A design and optimization of a high throughput valve based microfluidic device for single cell compartmentalization and analysis. Scientific reports, 11(1), 12995.

111. Au, A. K., Lai, H., Utela, B. R., & Folch, A. (2011). Microvalves and micropumps for BioMEMS. Micromachines, 2(2), 179-220.

112. Araci, I. E., & Brisk, P. (2014). Recent developments in microfluidic large scale integration. Current opinion in biotechnology, 25, 60-68.

113. Qian, J. Y., Hou, C. W., Li, X. J., & Jin, Z. J. (2020). Actuation mechanism of microvalves: A review. Micromachines, 11(2), 172.

114. Unger, M. A., Chou, H. P., Thorsen, T., Scherer, A., & Quake, S. R. (2000). Monolithic microfabricated valves and pumps by multilayer soft lithography. science, 288(5463), 113-116.

115. Thorsen, T., Maerkl, S. J., & Quake, S. R. (2002). Microfluidic large-scale integration. Science, 298(5593), 580-584.

116. Araci, I. E., & Quake, S. R. (2012). Microfluidic very large scale integration (mVLSI) with integrated micromechanical valves. Lab on a Chip, 12(16), 2803-2806.

117. Weibel, D. B., DiLuzio, W. R., & Whitesides, G. M. (2007). Microfabrication meets microbiology. Nature Reviews Microbiology, 5(3), 209-218.

118. Dy, A. J., Cosmanescu, A., Sluka, J., Glazier, J. A., Stupack, D., & Amarie, D. (2014). Fabricating microfluidic valve master molds in SU-8 photoresist. Journal of Micromechanics and Microengineering, 24(5), 057001.

119. Cocovi-Solberg, D. J., Rosende, M., Michalec, M., & Miró, M. (2018). 3D printing: the second dawn of lab-on-valve fluidic platforms for automatic (bio) chemical assays. Analytical chemistry, 91(1), 1140-1149.

120. Gong, H., Woolley, A. T., & Nordin, G. P. (2016). High density 3D printed microfluidic valves, pumps, and multiplexers. Lab on a Chip, 16(13), 2450-2458.

121. Gong, H., Woolley, A. T., & Nordin, G. P. (2018). 3D printed high density, reversible, chip-to-chip microfluidic interconnects. Lab on a Chip, 18(4), 639-647.

122. Zhou, Z., He, G., Zhang, K., Zhao, Y., & Sun, D. (2019). 3D-printed membrane microvalves and microdecoder. Microsystem Technologies, 25, 4019-4025.

123. Keating, S. J., Gariboldi, M. I., Patrick, W. G., Sharma, S., Kong, D. S., & Oxman, N. (2016). 3D printed multimaterial microfluidic valve. PloS one, 11(8), e0160624.

124. Lee, Y. S., Bhattacharjee, N., & Folch, A. (2018). 3D-printed Quake-style microvalves and micropumps. Lab on a Chip, 18(8), 1207-1214.

125. Rogers, C. I., Qaderi, K., Woolley, A. T., & Nordin, G. P. (2015). 3D printed microfluidic devices with integrated valves. Biomicrofluidics, 9(1).

126. Sanchez Noriega, J.L., Chartrand, N.A., Valdoz, J.C., Cribbs, C.G., Jacobs, D.A., Poulson, D., Viglione, M.S., Woolley, A.T., Van Ry, P.M., Christensen, K.A., & Nordin,

G.P. (2021). Spatially and optically tailored 3D printing for highly miniaturized and integrated microfluidics. Nature Communications, 12(1), 5509.

127. Ho, C. M. B., Ng, S. H., Li, K. H. H., & Yoon, Y. J. (2015). 3D printed microfluidics for biological applications. Lab on a Chip, 15(18), 3627-3637.

128. Castiaux, A. D., Selemani, M. A., Ward, M. A., & Martin, R. S. (2021). Fully 3D printed fluidic devices with integrated valves and pumps for flow injection analysis. Analytical Methods, 13(42), 5017-5024.

129. Winkler, S., Menke, J., Meyer, K. V., Kortmann, C., & Bahnemann, J. (2022). Automation of cell culture assays using a 3D-printed servomotor-controlled microfluidic valve system. Lab on a Chip, 22(23), 4656-4665.

130. Diehm, J., Hackert, V., & Franzreb, M. (2021). Configurable 3D printed microfluidic multiport valves with axial compression. Micromachines, 12(10), 1247.

131. Nie, M., & Takeuchi, S. (2020). Luer-lock valve: A pre-fabricated pneumatic valve for 3D printed microfluidic automation. Biomicrofluidics, 14(4).

132. Hinnen, H., Viglione, M., Munro, T. R., Woolley, A. T., & Nordin, G. P. (2023). 3D-Printed Microfluidic One-Way Valves and Pumps. Micromachines, 14(7), 1286.

133. Chaudhary, R., Fabbri, P., Leoni, E., Mazzanti, F., Akbari, R., & Antonini, C. (2023). Additive manufacturing by digital light processing: a review. Progress in Additive Manufacturing, 8(2), 331-351.

134. Zhang, J., Hu, Q., Wang, S., Tao, J., & Gou, M. (2020). Digital light processing based three-dimensional printing for medical applications. International journal of bioprinting, 6(1).

135. Waheed, S., Cabot, J. M., Macdonald, N. P., Lewis, T., Guijt, R. M., Paull, B., & Breadmore, M. C. (2016). 3D printed microfluidic devices: enablers and barriers. Lab on a Chip, 16(11), 1993-2013.

136. Melin, J., & Quake, S. R. (2007). Microfluidic large-scale integration: the evolution of design rules for biological automation. Annu. Rev. Biophys. Biomol. Struct., 36, 213-231.

137. Choe, J. K., Yi, J., Jang, H., Won, H., Lee, S., Lee, H., ... & Kim, J. (2024). Digital Mechanical Metamaterial: Encoding Mechanical Information with Graphical Stiffness Pattern for Adaptive Soft Machines. Advanced Materials, 36(4), 2304302.

138. Pahlavani, H., Tsifoutis-Kazolis, K., Saldivar, M. C., Mody, P., Zhou, J., Mirzaali, M. J., & Zadpoor, A. A. (2024). Deep Learning for Size-Agnostic Inverse Design of Random-Network 3D Printed Mechanical Metamaterials. Advanced Materials, 36(6), 2303481.

139. Li, T., & Li, Y. (2024). 3D Tiled Auxetic Metamaterial: A New Family of Mechanical Metamaterial with High Resilience and Mechanical Hysteresis. Advanced Materials, 2309604.

140. Cheng, X., Zhang, Y., Ren, X., Han, D., Jiang, W., Zhang, X.G., Luo, H.C., & Xie, Y.M. (2022). Design and mechanical characteristics of auxetic metamaterial with tunable stiffness. International Journal of Mechanical Sciences, 223, 107286.

141. Kolken, H. M., & Zadpoor, A. A. (2017). Auxetic mechanical metamaterials. RSC advances, 7(9), 5111-5129.

142. Mir, M., Ali, M. N., Sami, J., & Ansari, U. (2014). Review of mechanics and applications of auxetic structures. Advances in Materials Science and Engineering, 2014.

143. Buckles, B. P., & Lybanon, M. (1977). Algorithm 515: Generation of a vector from the lexicographical index [G6]. ACM Transactions on Mathematical Software (TOMS), 3(2), 180-182.

144. Genitrini, A., & Pépin, M. (2021). Lexicographic unranking of combinations revisited. Algorithms, 14(3), 97.

145. Pahlavani, H., Amani, M., Saldívar, M. C., Zhou, J., Mirzaali, M. J., & Zadpoor, A. A. (2022). Deep learning for the rare-event rational design of 3D printed multi-material mechanical metamaterials. Communications Materials, 3(1), 46.

146. Kim, Y. T., Ahmadianyazdi, A., & Folch, A. (2023). A 'print–pause–print'protocol for 3D printing microfluidics using multimaterial stereolithography. Nature protocols, 18(4), 1243-1259.

147. White, J. A., & Streets, A. M. (2018). Controller for microfluidic large-scale integration. HardwareX, 3, 135-145.

148. Brower, K., Puccinelli, R.R., Markin, C.J., Shimko, T.C., Longwell, S.A., Cruz, B., Gomez-Sjoberg, R., & Fordyce, P.M. (2018). An open-source, programmable pneumatic setup for operation and automated control of single- and multi-layer microfluidic devices. HardwareX, 3, 117-134.

149. Machado, F., Malpica, N., & Borromeo, S. (2019). Parametric CAD modeling for open source scientific hardware: Comparing OpenSCAD and FreeCAD Python scripts. Plos one, 14(12), e0225795.

150. Kintel, M. & Wolf, C. (2014). GNU General Public License.

APPENDIX A: SUPPORTING INFORMATION CHAPTER II

Supporting Information includes DNA sequences for all oligonucleotides used in Compartmentalized CRISPR Reaction (CCR) assays in Chapter II.

Supplementary Note 2. DNA library related to Figure 19

1. 5′ –
   GACATCACCTCCCACAACGACGAAAAGAGGAGGAAGGGCCTGAGTCCGAGCAGAAGAAGAAGGGC
   TCCCATCACATCAATGGGCTTTGGAAAGGGGGTGGGGGGAGTTTGCTCCTGGACCCCCTATTTCT
   GATAATACGACTCACTATAGGAGTCCGAGCAGAAGAAGAAGTTTTAGAGCTAGAAATAGCAAGTT
   AAAATAAGGCTAGTCCGTTATCAACTTGAAAAAGTGGCACCGAGTCGGTGCTTTTTTAAACGAGG
   CGAGTTTACGGGTTGTTA
2. 5′ –
   GACATCACCTCCCACAACGACGAGGGTGGGCTTTGGAAAGGGGGTGGGGGGAGTTTGCTCCTGGA
   CCCCCTATTTCTGAGAGGAGGAAGGGCCTGAGTCCGAGCAGAAGAAGAAGGGCTCCCATCACATC
   AATAATACGACTCACTATAGGGGTGGGGGGAGTTTGCTCCGTTTTAGAGCTAGAAATAGCAAGTT
   AAAATAAGGCTAGTCCGTTATCAACTTGAAAAAGTGGCACCGAGTCGGTGCTTTTTTGGGCGAGG
   CGAGTTTACGGGTTGTTA

Supplementary Note 3. On-target DNA library related to Figure 21

1) GACATCACCTCCCACAACGACGAAAACCTCCCCATTGGCCTGCTTCGTGGCAATGCGCCACCGGT
   TGATGTGATGGGAGGGATCTTATAGAGCCTGTGTGGACCCCCTATTTCTGATAATACGACTCACT
   ATAGGCTTCGTGGCAATGCGCCACGTTTTAGAGCTAGAAATAGCAAGTTAAAATAAGGCTAGTCC
   GTTATCAACTTGAAAAAGTGGCACCGAGTCGGTGCTTTTTTAAACGAGGCGAGTTTACGGGTTGT
   TA
2) GACATCACCTCCCACAACGACGAAAACTGCTTCGTGGCAATGCGCCACCGGTTGATGTGATGGGA
   GCCCTTCTTCTTCTGGATCTTATAGAGCCTGTGTGGACCCCCTATTTCTGATAATACGACTCACT
   ATAGGCGCCACCGGTTGATGTGATGTTTTAGAGCTAGAAATAGCAAGTTAAAATAAGGCTAGTCC
   GTTATCAACTTGAAAAAGTGGCACCGAGTCGGTGCTTTTTTAAACGAGGCGAGTTTACGGGTTGT
   TA
3) GACATCACCTCCCACAACGACGAAAACCATCACATCAACCGGTGGCGCATTGCCACGAAGCAGGC
   CAATGGGGAGGACAGGATCTTATAGAGCCTGTGTGGACCCCCTATTTCTGATAATACGACTCACT
   ATAGGTGGCGCATTGCCACGAAGCGTTTTAGAGCTAGAAATAGCAAGTTAAAATAAGGCTAGTCC
   GTTATCAACTTGAAAAAGTGGCACCGAGTCGGTGCTTTTTTAAACGAGGCGAGTTTACGGGTTGT
   TA
4) GACATCACCTCCCACAACGACGAAAACCTGCTTCGTGGCAATGCGCCACCGGTTGATGTGATGGG
   AGCCCTTCTTCTTCGGATCTTATAGAGCCTGTGTGGACCCCCTATTTCTGATAATACGACTCACT
   ATAGTGCGCCACCGGTTGATGTGAGTTTTAGAGCTAGAAATAGCAAGTTAAAATAAGGCTAGTCC
   GTTATCAACTTGAAAAAGTGGCACCGAGTCGGTGCTTTTTTAAACGAGGCGAGTTTACGGGTTGT
   TA
5) GACATCACCTCCCACAACGACGAAAAAGCAGAAGAAGAAGGGCTCCCATCACATCAACCGGTGGC
   GCATTGCCACGAAGGGATCTTATAGAGCCTGTGTGGACCCCCTATTTCTGATAATACGACTCACT
   ATAGGCTCCCATCACATCAACCGGGTTTTAGAGCTAGAAATAGCAAGTTAAAATAAGGCTAGTCC

GTTATCAACTTGAAAAAGTGGCACCGAGTCGGTGCTTTTTTAAACGAGGCGAGTTTACGGGTTGT
TA

6) GACATCACCTCCCACAACGACGAAAATCAACCGGTGGCGCATTGCCACGAAGCAGGCCAATGGGG
AGGACATCGATGTCGGATCTTATAGAGCCTGTGTGGACCCCCTATTTCTGATAATACGACTCACT
ATAGTTGCCACGAAGCAGGCCAATGTTTTAGAGCTAGAAATAGCAAGTTAAAATAAGGCTAGTCC
GTTATCAACTTGAAAAAGTGGCACCGAGTCGGTGCTTTTTTAAACGAGGCGAGTTTACGGGTTGT
TA

7) GACATCACCTCCCACAACGACGAAAAGGTGACATCGATGTCCTCCCCATTGGCCTGCTTCGTGGC
AATGCGCCACCGGTGGATCTTATAGAGCCTGTGTGGACCCCCTATTTCTGATAATACGACTCACT
ATAGCTCCCCATTGGCCTGCTTCGGTTTTAGAGCTAGAAATAGCAAGTTAAAATAAGGCTAGTCC
GTTATCAACTTGAAAAAGTGGCACCGAGTCGGTGCTTTTTTAAACGAGGCGAGTTTACGGGTTGT
TA

8) GACATCACCTCCCACAACGACGAAAACTAGTCATTGGAGGTGACATCGATGTCCTCCCCATTGGC
CTGCTTCGTGGCAAGGATCTTATAGAGCCTGTGTGGACCCCCTATTTCTGATAATACGACTCACT
ATAGGACATCGATGTCCTCCCCATGTTTTAGAGCTAGAAATAGCAAGTTAAAATAAGGCTAGTCC
GTTATCAACTTGAAAAAGTGGCACCGAGTCGGTGCTTTTTTAAACGAGGCGAGTTTACGGGTTGT
TA

9) GACATCACCTCCCACAACGACGAAAACAACCGGTGGCGCATTGCCACGAAGCAGGCCAATGGGGA
GGACATCGATGTCAGGATCTTATAGAGCCTGTGTGGACCCCCTATTTCTGATAATACGACTCACT
ATAGTGCCACGAAGCAGGCCAATGGTTTTAGAGCTAGAAATAGCAAGTTAAAATAAGGCTAGTCC
GTTATCAACTTGAAAAAGTGGCACCGAGTCGGTGCTTTTTTAAACGAGGCGAGTTTACGGGTTGT
TA

10) GACATCACCTCCCACAACGACGAAAACCGAGCAGAAGAAGAAGGGCTCCCATCACATCAACCGGT
GGCGCATTGCCACGGGATCTTATAGAGCCTGTGTGGACCCCCTATTTCTGATAATACGACTCACT
ATAGAGGGCTCCCATCACATCAACGTTTTAGAGCTAGAAATAGCAAGTTAAAATAAGGCTAGTCC
GTTATCAACTTGAAAAAGTGGCACCGAGTCGGTGCTTTTTTAAACGAGGCGAGTTTACGGGTTGT
TA

11) GACATCACCTCCCACAACGACGAAAACCGGTGGCGCATTGCCACGAAGCAGGCCAATGGGGAGGA
CATCGATGTCACCTGGATCTTATAGAGCCTGTGTGGACCCCCTATTTCTGATAATACGACTCACT
ATAGCACGAAGCAGGCCAATGGGGGTTTTAGAGCTAGAAATAGCAAGTTAAAATAAGGCTAGTCC
GTTATCAACTTGAAAAAGTGGCACCGAGTCGGTGCTTTTTTAAACGAGGCGAGTTTACGGGTTGT
TA

12) GACATCACCTCCCACAACGACGAAAAATGTGATGGGAGCCCTTCTTCTTCTGCTCGGACTCAGGC
CCTTCCTCCTCCAGGGATCTTATAGAGCCTGTGTGGACCCCCTATTTCTGATAATACGACTCACT
ATAGTTCTTCTTCTGCTCGGACTCGTTTTAGAGCTAGAAATAGCAAGTTAAAATAAGGCTAGTCC
GTTATCAACTTGAAAAAGTGGCACCGAGTCGGTGCTTTTTTAAACGAGGCGAGTTTACGGGTTGT
TA

13) GACATCACCTCCCACAACGACGAAAAATCAACCGGTGGCGCATTGCCACGAAGCAGGCCAATGGG
GAGGACATCGATGTGGATCTTATAGAGCCTGTGTGGACCCCCTATTTCTGATAATACGACTCACT
ATAGATTGCCACGAAGCAGGCCAAGTTTTAGAGCTAGAAATAGCAAGTTAAAATAAGGCTAGTCC
GTTATCAACTTGAAAAAGTGGCACCGAGTCGGTGCTTTTTTAAACGAGGCGAGTTTACGGGTTGT
TA

14) GACATCACCTCCCACAACGACGAAAACCGGTTGATGTGATGGGAGCCCTTCTTCTTCTGCTCGGA
CTCAGGCCCTTCCTGGATCTTATAGAGCCTGTGTGGACCCCCTATTTCTGATAATACGACTCACT
ATAGGGAGCCCTTCTTCTTCTGCTGTTTTAGAGCTAGAAATAGCAAGTTAAAATAAGGCTAGTCC
GTTATCAACTTGAAAAAGTGGCACCGAGTCGGTGCTTTTTTAAACGAGGCGAGTTTACGGGTTGT
TA

15) GACATCACCTCCCACAACGACGAAAAGGAGGAGGAAGGGCCTGAGTCCGAGCAGAAGAAGAAGGG
CTCCCATCACATCAGGATCTTATAGAGCCTGTGTGGACCCCCTATTTCTGATAATACGACTCACT
ATAGTGAGTCCGAGCAGAAGAAGAGTTTTAGAGCTAGAAATAGCAAGTTAAAATAAGGCTAGTCC
GTTATCAACTTGAAAAAGTGGCACCGAGTCGGTGCTTTTTTAAACGAGGCGAGTTTACGGGTTGT
TA

16) GACATCACCTCCCACAACGACGAAAAGAGGAGGAAGGGCCTGAGTCCGAGCAGAAGAAGAAGGGC
TCCCATCACATCAAGGATCTTATAGAGCCTGTGTGGACCCCCTATTTCTGATAATACGACTCACT
ATAGGAGTCCGAGCAGAAGAAGAAGTTTTAGAGCTAGAAATAGCAAGTTAAAATAAGGCTAGTCC
GTTATCAACTTGAAAAAGTGGCACCGAGTCGGTGCTTTTTTAAACGAGGCGAGTTTACGGGTTGT
TA

17) GACATCACCTCCCACAACGACGAAAAAGGACAAAGTACAAACGGCAGAAGCTGGAGGAGGAAGGG
CCTGAGTCCGAGCAGGATCTTATAGAGCCTGTGTGGACCCCCTATTTCTGATAATACGACTCACT
ATAGCGGCAGAAGCTGGAGGAGGAGTTTTAGAGCTAGAAATAGCAAGTTAAAATAAGGCTAGTCC
GTTATCAACTTGAAAAAGTGGCACCGAGTCGGTGCTTTTTTAAACGAGGCGAGTTTACGGGTTGT
TA

18) GACATCACCTCCCACAACGACGAAAAGGACAAAGTACAAACGGCAGAAGCTGGAGGAGGAAGGGC
CTGAGTCCGAGCAGGGATCTTATAGAGCCTGTGTGGACCCCCTATTTCTGATAATACGACTCACT
ATAGGGCAGAAGCTGGAGGAGGAAGTTTTAGAGCTAGAAATAGCAAGTTAAAATAAGGCTAGTCC
GTTATCAACTTGAAAAAGTGGCACCGAGTCGGTGCTTTTTTAAACGAGGCGAGTTTACGGGTTGT
TA

Supplementary Note 4. On-OFF DNA library related to Figure 22

**********ON**********
**********OFF**********

1) GACATCACCTCCCACAACGACGAAAACCTCCCCATTGGCCTGCTTCGTGGCAATGCGCCACCGGT
TGATGTGATGGGAGTGGGCTTTGGAAAGGCTTATGGCATGGGATATGTCTGGATGTGCTTTGTGG
CAATGCACAACTGGTCAGTGGGAAGGGACATCTTATAGAGCCTGTGTGGACCCCCTATTTCTGAT
AATACGACTCACTATAGGCTTCGTGGCAATGCGCCACGTTTTAGAGCTAGAAATAGCAAGTTAAA
ATAAGGCTAGTCCGTTATCAACTTGAAAAAGTGGCACCGAGTCGGTGCTTTTTTAAACGAGGCGA
GTTTACGGGTTGTTA

2) GACATCACCTCCCACAACGACGAAAACCTCCCCATTGGCCTGCTTCGTGGCAATGCGCCACCGGT
TGATGTGATGGGAGTGGGCTTTGGAAAGGCTTATGGCATGGCCTTAACTCGAGGTGCCCGTGGCA
AATTGACACGAAGCTGTCCACCTGTTGGAATCTTATAGAGCCTGTGTGGACCCCCTATTTCTGAT
AATACGACTCACTATAGGCTTCGTGGCAATGCGCCACGTTTTAGAGCTAGAAATAGCAAGTTAAA
ATAAGGCTAGTCCGTTATCAACTTGAAAAAGTGGCACCGAGTCGGTGCTTTTTTAAACGAGGCGA
GTTTACGGGTTGTTA

3) GACATCACCTCCCACAACGACGAAAACTGCTTCGTGGCAATGCGCCACCGGTTGATGTGATGGGA
GCCCTTCTTCTTCTTGGGCTTTGGAAAGGCTTATGGCATGGCTCTAGAGACACATGCTCATCACA
TCAACCCATGGCCCAGAAACCTCCAGTGGATCTTATAGAGCCTGTGTGGACCCCCTATTTCTGAT
AATACGACTCACTATAGGCGCCACCGGTTGATGTGATGTTTTAGAGCTAGAAATAGCAAGTTAAA
ATAAGGCTAGTCCGTTATCAACTTGAAAAAGTGGCACCGAGTCGGTGCTTTTTTAAACGAGGCGA
GTTTACGGGTTGTTA

4) GACATCACCTCCCACAACGACGAAAACTGCTTCGTGGCAATGCGCCACCGGTTGATGTGATGGGA
GCCCTTCTTCTTCTTGGGCTTTGGAAAGGCTTATGGCATGGGAATCAACCTAGATGCCCATCAGA
TCAACTGGTGGCACACATACACTATGAAAATCTTATAGAGCCTGTGTGGACCCCCTATTTCTGAT
AATACGACTCACTATAGGCGCCACCGGTTGATGTGATGTTTTAGAGCTAGAAATAGCAAGTTAAA
ATAAGGCTAGTCCGTTATCAACTTGAAAAAGTGGCACCGAGTCGGTGCTTTTTTAAACGAGGCGA
GTTTACGGGTTGTTA

5) GACATCACCTCCCACAACGACGAAAACCATCACATCAACCGGTGGCGCATTGCCACGAAGCAGGC
CAATGGGGAGGACATGGGCTTTGGAAAGGCTTATGGCATGGAGCCGCAGCCTGGCCCCGGCTCCT
TGGCAATGAGCCACCTCCTACCTGTCGCCATCTTATAGAGCCTGTGTGGACCCCCTATTTCTGAT
AATACGACTCACTATAGGTGGCGCATTGCCACGAAGCGTTTTAGAGCTAGAAATAGCAAGTTAAA
ATAAGGCTAGTCCGTTATCAACTTGAAAAAGTGGCACCGAGTCGGTGCTTTTTTAAACGAGGCGA
GTTTACGGGTTGTTA

6) GACATCACCTCCCACAACGACGAAAACCATCACATCAACCGGTGGCGCATTGCCACGAAGCAGGC
CAATGGGGAGGACATGGGCTTTGGAAAGGCTTATGGCATGGCAGTGTGCACCTCACTCAGCTTCG
TGTCAATGCCACACCATGTGGGGAGTGTTATCTTATAGAGCCTGTGTGGACCCCCTATTTCTGAT
AATACGACTCACTATAGGTGGCGCATTGCCACGAAGCGTTTTAGAGCTAGAAATAGCAAGTTAAA
ATAAGGCTAGTCCGTTATCAACTTGAAAAAGTGGCACCGAGTCGGTGCTTTTTTAAACGAGGCGA
GTTTACGGGTTGTTA

7) GACATCACCTCCCACAACGACGAAAACCATCACATCAACCGGTGGCGCATTGCCACGAAGCAGGC
CAATGGGGAGGACATGGGCTTTGGAAAGGCTTATGGCATGGAAATGTTCTAGGACCATGGCACAT
TGCCACTAAGCAGGAGTCAAAAGACTACAATCTTATAGAGCCTGTGTGGACCCCCTATTTCTGAT
AATACGACTCACTATAGGTGGCGCATTGCCACGAAGCGTTTTAGAGCTAGAAATAGCAAGTTAAA
ATAAGGCTAGTCCGTTATCAACTTGAAAAAGTGGCACCGAGTCGGTGCTTTTTTAAACGAGGCGA
GTTTACGGGTTGTTA

8) GACATCACCTCCCACAACGACGAAAAAGCAGAAGAAGAAGGGCTCCCATCACATCAACCGGTGGC
GCATTGCCACGAAGTGGGCTTTGGAAAGGCTTATGGCATGGGAGGTGTCTCTGAAGCCTCAGGGT
GATGTGATGGGAGCCCTGGTGCCCTCACTATCTTATAGAGCCTGTGTGGACCCCCTATTTCTGAT
AATACGACTCACTATAGGCTCCCATCACATCAACCGGGTTTTAGAGCTAGAAATAGCAAGTTAAA
ATAAGGCTAGTCCGTTATCAACTTGAAAAAGTGGCACCGAGTCGGTGCTTTTTTAAACGAGGCGA
GTTTACGGGTTGTTA

9) GACATCACCTCCCACAACGACGAAAAAGCAGAAGAAGAAGGGCTCCCATCACATCAACCGGTGGC
GCATTGCCACGAAGTGGGCTTTGGAAAGGCTTATGGCATGGGCCTGGCCAAGAAGTTCTCCCATC
ACATCCACCAGTGGATTCCCCTGCTGGGTATCTTATAGAGCCTGTGTGGACCCCCTATTTCTGAT
AATACGACTCACTATAGGCTCCCATCACATCAACCGGGTTTTAGAGCTAGAAATAGCAAGTTAAA
ATAAGGCTAGTCCGTTATCAACTTGAAAAAGTGGCACCGAGTCGGTGCTTTTTTAAACGAGGCGA
GTTTACGGGTTGTTA

10) GACATCACCTCCCACAACGACGAAAAAGCAGAAGAAGAAGGGCTCCCATCACATCAACCGGTGGC
GCATTGCCACGAAGTGGGCTTTGGAAAGGCTTATGGCATGGTCCCAGTAGGTGCATGCTGCCCTC
ACATCAACAGGTGGAGTCTATTTCCTCTCATCTTATAGAGCCTGTGTGGACCCCCTATTTCTGAT
AATACGACTCACTATAGGCTCCCATCACATCAACCGGGTTTTAGAGCTAGAAATAGCAAGTTAAA
ATAAGGCTAGTCCGTTATCAACTTGAAAAAGTGGCACCGAGTCGGTGCTTTTTTAAACGAGGCGA
GTTTACGGGTTGTTA

11) GACATCACCTCCCACAACGACGAAAAAGCAGAAGAAGAAGGGCTCCCATCACATCAACCGGTGGC
GCATTGCCACGAAGTGGGCTTTGGAAAGGCTTATGGCATGGGGTGACAAGTGGCAGGATCCCATC
ACATCCACAGGTGGCCTCGACTCTGGTCTATCTTATAGAGCCTGTGTGGACCCCCTATTTCTGAT
AATACGACTCACTATAGGCTCCCATCACATCAACCGGGTTTTAGAGCTAGAAATAGCAAGTTAAA
ATAAGGCTAGTCCGTTATCAACTTGAAAAAGTGGCACCGAGTCGGTGCTTTTTTAAACGAGGCGA
GTTTACGGGTTGTTA

12) GACATCACCTCCCACAACGACGAAAAAGCAGAAGAAGAAGGGCTCCCATCACATCAACCGGTGGC
GCATTGCCACGAAGTGGGCTTTGGAAAGGCTTATGGCATGGTCCCTTGTCCTGATGGCTTCCATC
ACAGCAGCCGGGGGCAACTCAGCCTGGACATCTTATAGAGCCTGTGTGGACCCCCTATTTCTGAT
AATACGACTCACTATAGGCTCCCATCACATCAACCGGGTTTTAGAGCTAGAAATAGCAAGTTAAA
ATAAGGCTAGTCCGTTATCAACTTGAAAAAGTGGCACCGAGTCGGTGCTTTTTTAAACGAGGCGA
GTTTACGGGTTGTTA

13) GACATCACCTCCCACAACGACGAAAAAGCAGAAGAAGAAGGGCTCCCATCACATCAACCGGTGGC
GCATTGCCACGAAGTGGGCTTTGGAAAGGCTTATGGCATGGATTGTTCAGTGATCTGCCCCCATC
AGATCTACCGGAGGCCCTTGCCTCAACCTATCTTATAGAGCCTGTGTGGACCCCCTATTTCTGAT

AATACGACTCACTATAGGCTCCCATCACATCAACCGGGTTTTAGAGCTAGAAATAGCAAGTTAAA
ATAAGGCTAGTCCGTTATCAACTTGAAAAAGTGGCACCGAGTCGGTGCTTTTTTAAACGAGGCGA
GTTTACGGGTTGTTA

14) GACATCACCTCCCACAACGACGAAAAAGCAGAAGAAGAAGGGCTCCCATCACATCAACCGGTGGC
GCATTGCCACGAAGTGGGCTTTGGAAAGGCTTATGGCATGGGCTCCCTTCTACCCAGCTCCCCTC
ACATGAACCTGAGGGCCCTGTCAAGGTGGATCTTATAGAGCCTGTGTGGACCCCCTATTTCTGAT
AATACGACTCACTATAGGCTCCCATCACATCAACCGGGTTTTAGAGCTAGAAATAGCAAGTTAAA
ATAAGGCTAGTCCGTTATCAACTTGAAAAAGTGGCACCGAGTCGGTGCTTTTTTAAACGAGGCGA
GTTTACGGGTTGTTA

15) GACATCACCTCCCACAACGACGAAAAGAGGAGGAAGGGCCTGAGTCCGAGCAGAAGAAGAAGGGC
TCCCATCACATCAATGGGCTTTGGAAAGGCTTATGGCATGGTGCCTTTACTCCATGCCTTTCTTC
TTCTGCTCTAACTCTGACAATCTGTCTTGATCTTATAGAGCCTGTGTGGACCCCCTATTTCTGAT
AATACGACTCACTATAGGAGTCCGAGCAGAAGAAGAAGTTTTAGAGCTAGAAATAGCAAGTTAAA
ATAAGGCTAGTCCGTTATCAACTTGAAAAAGTGGCACCGAGTCGGTGCTTTTTTAAACGAGGCGA
GTTTACGGGTTGTTA

16) GACATCACCTCCCACAACGACGAAAAGAGGAGGAAGGGCCTGAGTCCGAGCAGAAGAAGAAGGGC
TCCCATCACATCAATGGGCTTTGGAAAGGCTTATGGCATGGATTCATAGTAGACAAGAGTCTAAG
CAGAAGAAGAAGAGAGCCACTACCCAACCATCTTATAGAGCCTGTGTGGACCCCCTATTTCTGAT
AATACGACTCACTATAGGAGTCCGAGCAGAAGAAGAAGTTTTAGAGCTAGAAATAGCAAGTTAAA
ATAAGGCTAGTCCGTTATCAACTTGAAAAAGTGGCACCGAGTCGGTGCTTTTTTAAACGAGGCGA
GTTTACGGGTTGTTA

17) GACATCACCTCCCACAACGACGAAAAGAGGAGGAAGGGCCTGAGTCCGAGCAGAAGAAGAAGGGC
TCCCATCACATCAATGGGCTTTGGAAAGGCTTATGGCATGGGGGCCAGCATGACCTGAGTCCTAG
CAGGAGAAGAAGAGGCAGCCTAGAGTCTTATCTTATAGAGCCTGTGTGGACCCCCTATTTCTGAT
AATACGACTCACTATAGGAGTCCGAGCAGAAGAAGAAGTTTTAGAGCTAGAAATAGCAAGTTAAA
ATAAGGCTAGTCCGTTATCAACTTGAAAAAGTGGCACCGAGTCGGTGCTTTTTTAAACGAGGCGA
GTTTACGGGTTGTTA

18) GACATCACCTCCCACAACGACGAAAAGAGGAGGAAGGGCCTGAGTCCGAGCAGAAGAAGAAGGGC
TCCCATCACATCAATGGGCTTTGGAAAGGCTTATGGCATGGTCTTCTGCAAATGAGGAGGCCGAG
CAGAAGAAAGACGGCGACAGATGTTGGGGATCTTATAGAGCCTGTGTGGACCCCCTATTTCTGAT
AATACGACTCACTATAGGAGTCCGAGCAGAAGAAGAAGTTTTAGAGCTAGAAATAGCAAGTTAAA
ATAAGGCTAGTCCGTTATCAACTTGAAAAAGTGGCACCGAGTCGGTGCTTTTTTAAACGAGGCGA
GTTTACGGGTTGTTA

**********ON**********
********** **********OFF**********
****

Supplementary Note 5. Extended gRNAs (x-gRNAs) Library related to Figure 23

1) GACATCACCTCCCACAACGACGAAAAGAGGAGGAAGGGCCTGAGTCCGAGCAGAAGAAGAAGGGC
TCCCATCACATCAATGGGCTTTGGAAAGGcttatggcatggcaagacagattgtcaGAGTTAGAG
CAGAAGAAGAAAGGcatggagtaaaggcaatcttatagagcctgtgTGGACCCCCTATTTCTGAT
AATACGACTCACTATAGNNNNNNNNGAGTCCGAGCAGAAGAAGAAGTTTTAGAGCTAGAAATAGC
AAGTTAAAATAAGGCTAGTCCGTTATCAACTTGAAAAAGTGGCACCGAGTCGGTGCTTTTTTAAA
CGAGGCGAGTTTACGGGTTGTTA

2) GACATCACCTCCCACAACGACGAAAAGAGGAGGAAGGGCCTGAGTCCGAGCAGAAGAAGAAGGGC
TCCCATCACATCAATGGGCTTTGGAAAGGcttatggcatggattcatagtagacaaGAGTCTAAG
CAGAAGAAGAAGAGagccactacccaaccatctaagagagactgtgTGGACCCCCTATTTCTGAT
AATACGACTCACTATAGNNNNNNNNGAGTCCGAGCAGAAGAAGAAGTTTTAGAGCTAGAAATAGC
AAGTTAAAATAAGGCTAGTCCGTTATCAACTTGAAAAAGTGGCACCGAGTCGGTGCTTTTTTAAA
CGAGGCGAGTTTACGGGTTGTTA

3) GACATCACCTCCCACAACGACGAAAAGAGGAGGAAGGGCCTGAGTCCGAGCAGAAGAAGAAGGGC
TCCCATCACATCAATGGGCTTTGGAAAGGcttatggcatggtcttctgcaaatgagGAGGCCGAG
CAGAAGAAAGACGGcgacagatgttgggggggaggcaggtagctgtgTGGACCCCCTATTTCTGAT
AATACGACTCACTATAGNNNNNNNNGAGTCCGAGCAGAAGAAGAAGTTTTAGAGCTAGAAATAGC
AAGTTAAAATAAGGCTAGTCCGTTATCAACTTGAAAAAGTGGCACCGAGTCGGTGCTTTTTTAAA
CGAGGCGAGTTTACGGGTTGTTA
4) GACATCACCTCCCACAACGACGAAAAGAGGAGGAAGGGCCTGAGTCCGAGCAGAAGAAGAAGGGC
TCCCATCACATCAATGGGCTTTGGAAAGGcttatggcatgggggccagcatgacctGAGTCCTAG
CAGGAGAAGAAGAGgcagcctagagtcttatcttatagagcctgtgTGGACCCCCTATTTCTGAT
AATACGACTCACTATAGNNNNNNNNGAGTCCGAGCAGAAGAAGAAGTTTTAGAGCTAGAAATAGC
AAGTTAAAATAAGGCTAGTCCGTTATCAACTTGAAAAAGTGGCACCGAGTCGGTGCTTTTTTAAA
CGAGGCGAGTTTACGGGTTGTTA

Supplementary Note 1. EMX1 gene for *in vitro* validation related to Figure 24

5′ - TATGTAGCCTCAGTCTTCCCATCAGGCTCTCAGCTCAGCCTGAGTGTTGA
GGCCCCAGTGGCTGCTCTGGGGGCCTCCTGAGTTTCTCATCTGTGCCCCT
CCCTCCCTGGCCCAGGTGAAGGTGTGGTTCCAGAACCGGAGGACAAAGTA
CAAACGGCAGAAGCTGGAGGAGGAAGGGCCTGAGTCCGAGCAGAAGAAGA
AGGGCTCCCATCACATCAACCGGTGGCGCATTGCCACGAAGCAGGCCAAT
GGGGAGGACATCGATGTCACCTCCAATGACTAGGGTGGGCAACCACAAACC
- 3′

APPENDIX B: SUPPORTING INFORMATION CHAPTER III

Supporting Information includes additional images of re-entrant structures subjected to applied pressures and force *vs.* displacement graphs, as well as movies of cyclic loading and unloading of reentrant structures and fluid channels with “closeable” or “always open” segments as shown below:

Figure S1. A) Force-vs-Displacement Curves for 5 × 5 Re-entrant Grids with θ = 0° for Different Values of φ, with B) Corresponding Images of Structures being Compressed

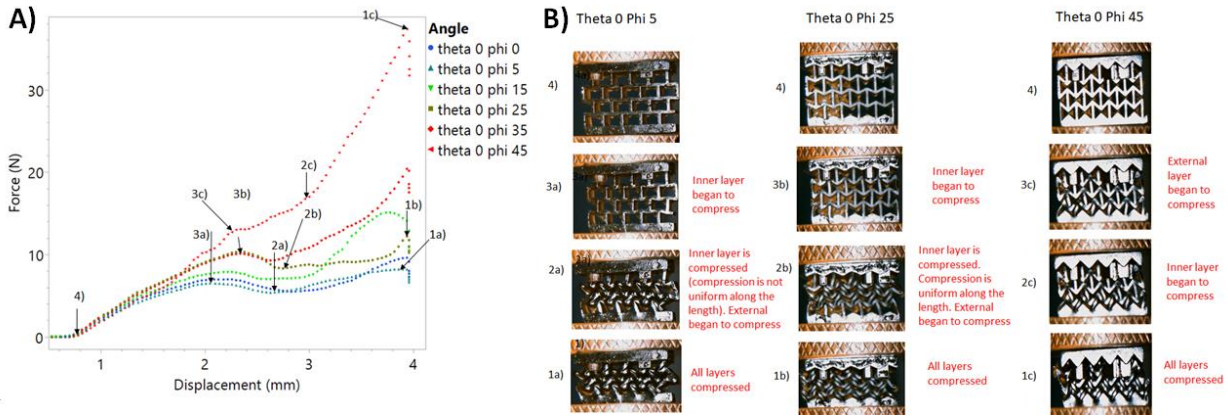

Figure S2. A) Force-vs-Displacement Curves for 5 × 5 Re-entrant Grids with θ = 25° for Different Values of φ, with B) Corresponding Images of Structures being Compressed

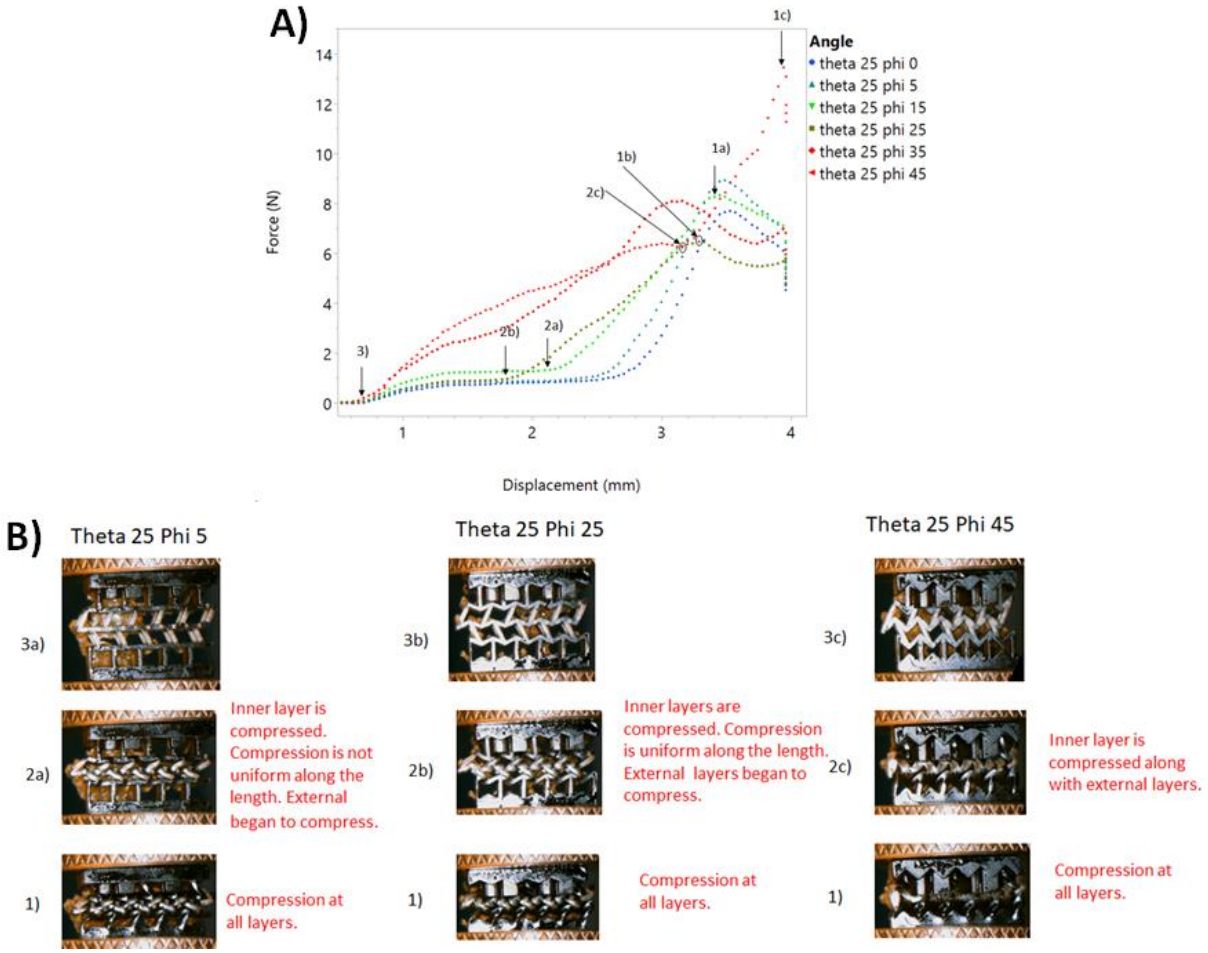

Figure S3. A) Force-vs-Displacement Curves for 5 × 5 Re-entrant Grids with φ = 25° for Different Values of θ, with B) Corresponding Images of Structures being Compressed

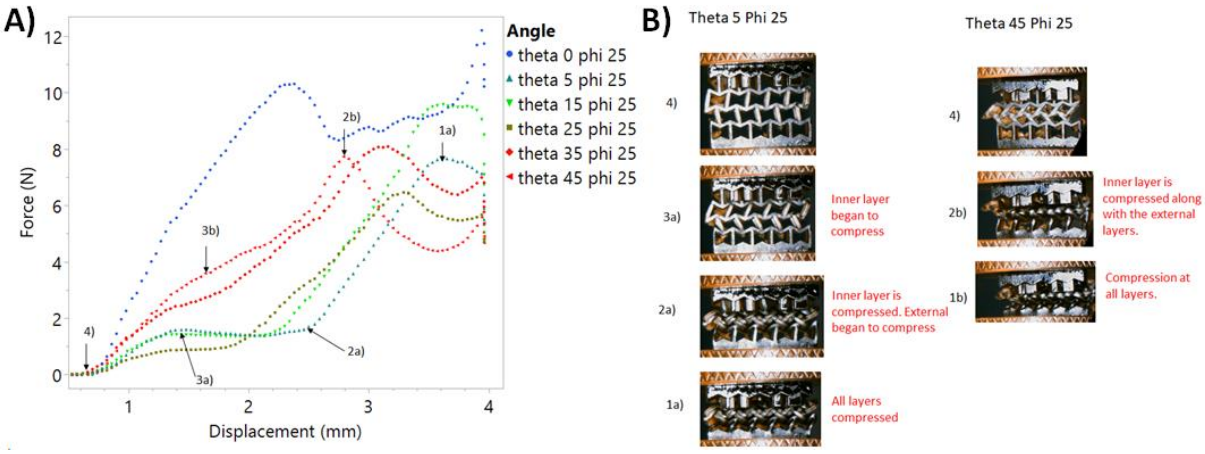

Figure S4. Close-up Structure (left) and Corresponding Overall Structure (right) for Stacked "Control" Regions of Re-entrant Honeycomb Grids at Different values of θ and φ

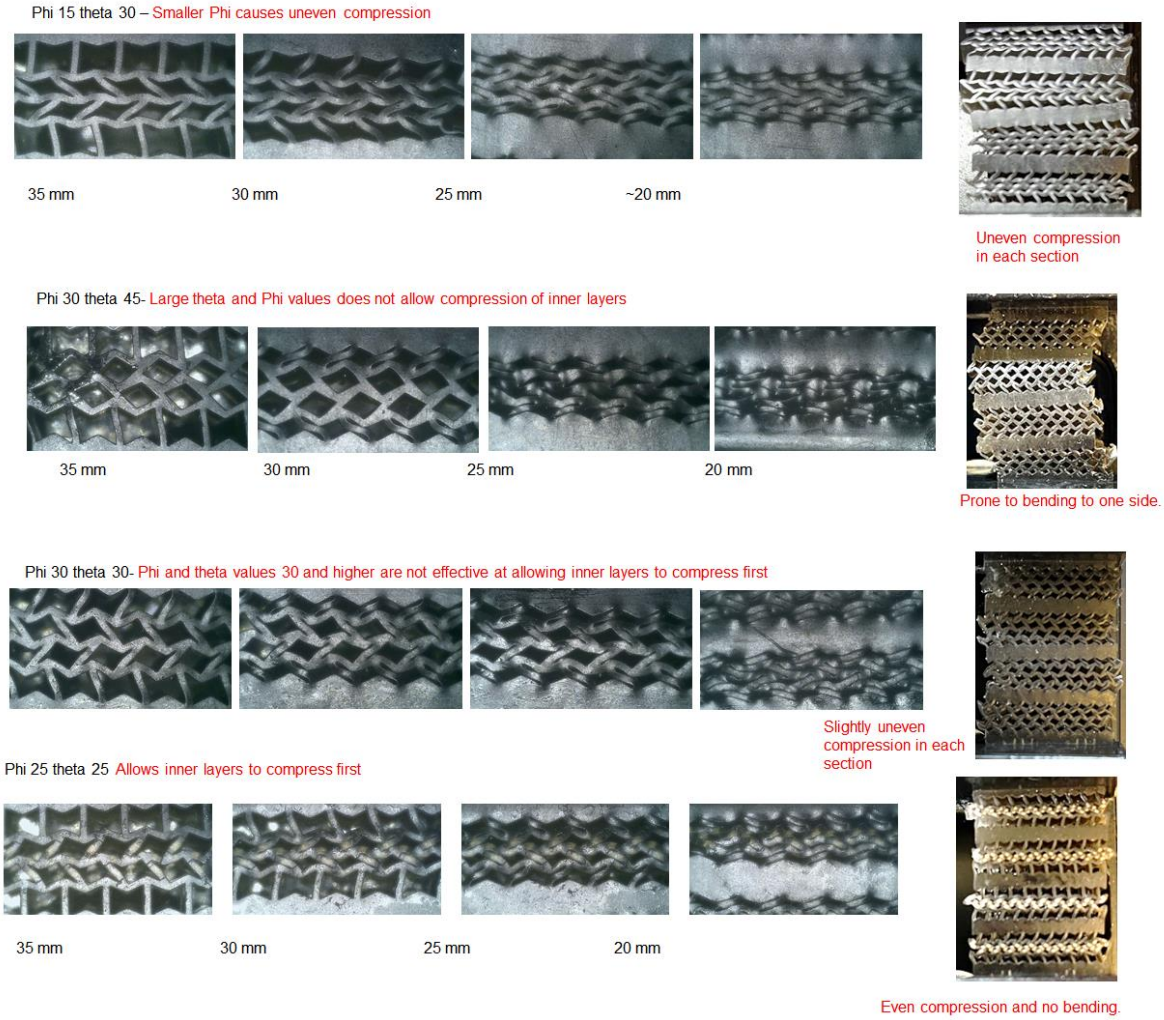

Figure S5. The 5 × 5 "Banded" Re-entrant Structures Exhibit Consistent Deformation and Mechanical behavior without Failing over the Course of 1000 Repetitive Deformations. The Average Maximum Force to Collapse the Inner Structures was 4.43 N with a Standard Deviation of 0.34 N Across the 1000 Cycles

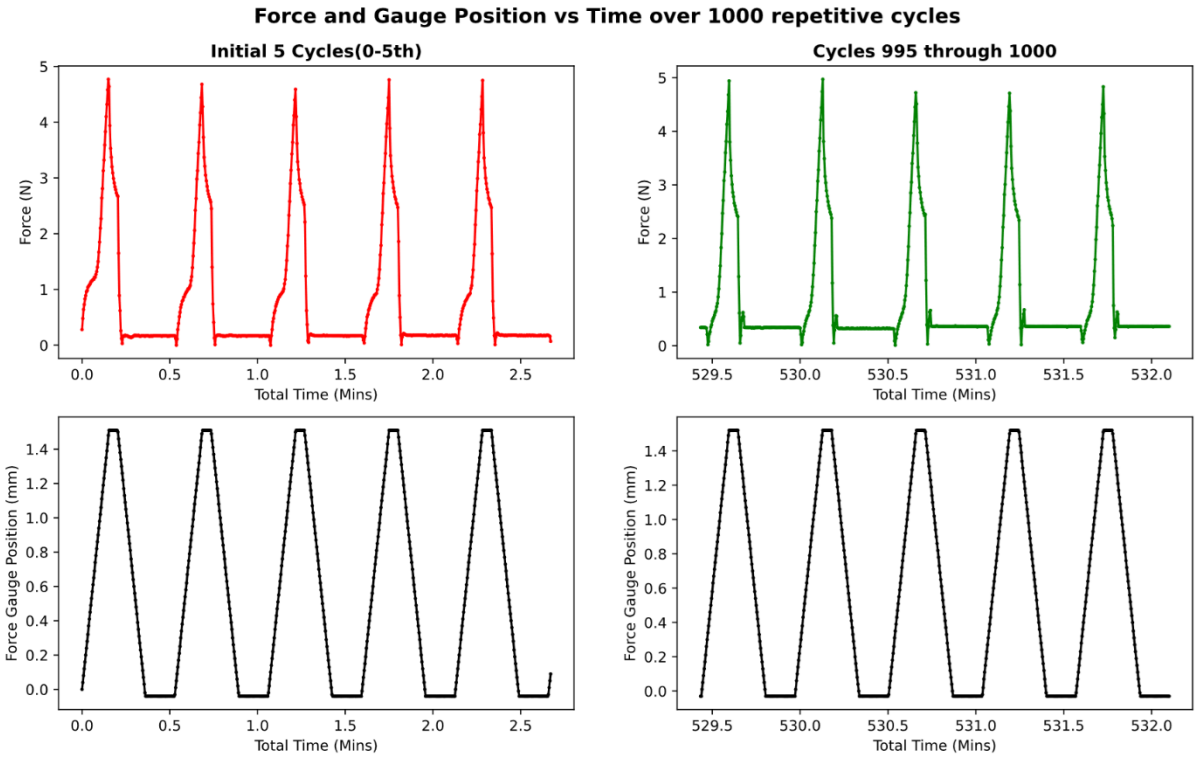

Figure S6. Demonstration of the Operation of the Quasi-Planar 3D Printed Metamaterial Valve Related to Figure 6. (Top) A 3D printed Stand was Used to Ensure Compression of 2 of 4 Control Regions Simultaneously Across the Quasi-Planar Valve Array. (Below) Compression of Sets of 2 Control Regions Allows for Flow in a Single Channel When Connected to a Microfluidic-Multiplexor

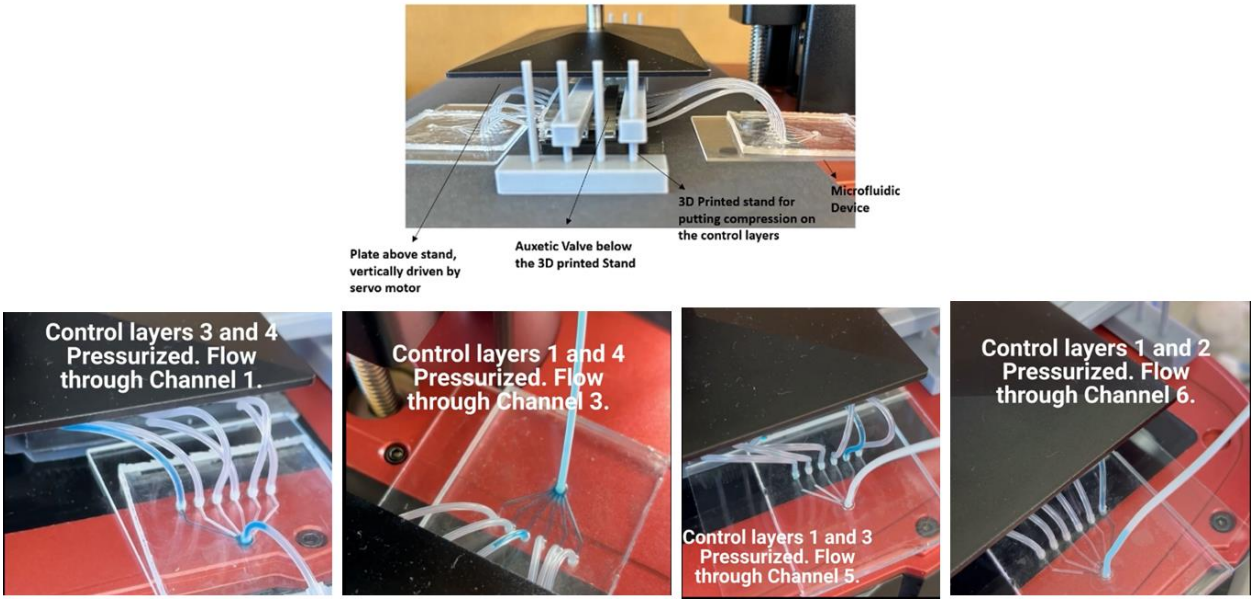

.